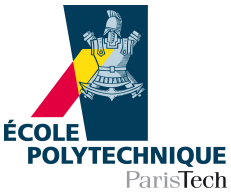

THÈSE

Présentée pour obtenir le grade de

DOCTEUR DE L'ÉCOLE POLYTECHNIQUE

Spécialité : Mécanique des fluides

par

Clément METTOT

Stabilité linéaire, sensibilité et contrôle passif d'écoulements turbulents par différence finies

Soutenue le 12 Décembre 2013 devant le jury composé de :

M. D. Sipp	Maître de recherche, DAFE-ONERA	*Directeur*
M. V. Theofilis	Professeur, Université Polytechnique de Madrid	*Rapporteur*
M. J.C. Robinet	Professeur, ENSAM Paristech	*Rapporteur*
M. C. Cossu	Directeur de recherche CNRS, IMFT Toulouse	*Examinateur*
M. L. Larchevêque	Maître de conférence, Polytech-Marseille	*Examinateur*
M. P. Meliga	Chargé de recherche, CNRS	*Examinateur*
M. F. Renac	Ingénieur de recherche, DSNA-ONERA	*Examinateur*
M. Y. Doutreleau	Encadrant DGA, MRIS -Bagneux	*Examinateur*

Abstract:

The contribution of this Ph.D consists in a formalism and a methodology to perform linear stability analysis of turbulent flows. The flow dynamics is modelled using the RANS equations closed with a turbulence model, and we focus on the instabilities associated with the large scale structures of turbulence. A global formulation is adopted so as to allow complex geometries analysis. A discrete framework is considered, where the equations are first discretized and then linearized. In particular, the linearization is performed using finite differences. This procedure ensures the generic character of the method regarding the system of equations such as the turbulence model for example, and avoids tedious analytical linearization. Furthermore, it allows to use a numerical code in a black-box manner in order to perform linear stability analysis. Finally, we demonstrate that the sensitivity gradients can be computed within this framework for both laminar and turbulent flows. Sensitivity analysis carries valuable information regarding the location where steady control means can affect the flow unsteadiness, enabling the design of robust strategies for open loop control.

The method is first tested on two laminar cases, reproducing former studies concerned with the oscillators dynamics of the wake behind a two dimensional cylinder, and the characterization of a laminar boundary layer as a noise amplifier. The robustness and validity of our procedure is then extensively studied on a compressible turbulent flow over a deep cavity. Numerical validations are performed, ensuring the correctness of our sensitivity gradients up to 3%, and the flow physics, including unstable mode analysis, acoustics, impact of turbulence modeling, is analysed. In order to enhance the portability and the valuable information carried out by our method, we present several preliminary studies that were performed using our formalism. First, we revisit the transonic buffet over an airfoil, the noise amplifier dynamics of a turbulent shock-boundary layer interaction is then characterized and we conclude with an analysis of the screech phenomenon in under-expanded jets. Finally, we conclude this work by studying the turbulent wake behind a D-shaped cylinder, and show the potential of our method for industrial applications.

Keywords: Global Stability, Sensitivity Analysis, Turbulence, RANS and URANS Dynamics, Passive Control, Jacobian matrix, Hessian, Finite Differences, Discrete Methods.

Résumé:

La contribution majeure de cette thèse consiste en un formalisme et une méthodologie permettant de réaliser une analyse de stabilité globale des écoulements turbulents. La dynamique de ces écoulements est modélisée à l'aide des équations moyennées RANS, on s'intéresse ainsi à l'évolution des grandes échelles turbulentes. Un formalisme global est adopté permettant d'analyser des écoulements complexes. Une approche de type discrète est proposée, où les équations sont d'abord discrétisées puis linéarisées par différences finies. Cette approche permet d'adopter une stratégie générique vis à vis du système d'équations utilisées, comme le choix d'un modèle turbulent, et évite une linéarisation analytique fastidieuse des équations. Par ailleurs, cette méthode permet également l'utilisation systématique d'un code de simulation numérique afin de réaliser une étude de stabilité linéaire. Enfin, on démontre que l'analyse de la sensibilité à des perturbations stationnaires peut être réalisée grâce à ce formalisme et ce pour des écoulements laminaires et turbulents. Cette analyse détermine les zones où un contrôle stationnaire permettrait de réduire les instationnarités observées, facilitant la conception de stratégies efficaces de contrôle en boucle ouverte.

La méthode est testée en premier lieu sur deux écoulements laminaires, où l'on reproduit les résultats obtenus par de précédentes études sur la dynamique d'oscillateur du sillage d'un cylindre bidimensionnel ainsi que sur la dynamique d'amplificateur de bruit d'une couche limite. La robustesse et la validité de notre méthode sont ensuite analysées sur un cas d'écoulement compressible et turbulent dans une cavité profonde. La précision des gradients de sensibilité est vérifiée, et la physique de l'écoulement, modes instables, propriétés acoustiques, impact de la modélisation de la turbulence, est détaillée. Afin de mieux appréhender la portabilité ainsi que la valeur ajoutée de notre méthode, on présentera ensuite trois cas d'études réalisées à l'aide de nos outils. On s'intéressera en premier lieu au phénomène de buffet sur un profil bidimensionnel, puis on présentera des résultats obtenus sur la caractérisation comme amplificateur de bruit d'un cas d'interaction de choc-couche limite, enfin une analyse du screech dans les jets sous détendus sera proposée. Enfin, on présente en dernier lieu la dynamique turbulente du sillage derrière un cylindre en forme de D, où le potentiel industriel de notre approche est mis en vidence.

Mots clés: Stabilité Globale, Analyse de Sensibilié, Turbulence, Dynamiques RANS et URANS, Contrôle passif, Matrice Jacobienne, Hessienne, Differences Finies, Méthodes Discrètes.

Contents

1 Introduction **1**
- 1.1 Flow dynamics characterization . . . 1
  - 1.1.1 Unsteady flows in fluid dynamics . . . 1
  - 1.1.2 Local and global stability . . . 2
  - 1.1.3 Non-normality of the Jacobian . . . 3
- 1.2 Passive control of laminar flows . . . 4
  - 1.2.1 Sensitivity of oscillators . . . 4
  - 1.2.2 Sensitivity of noise amplifiers . . . 5
- 1.3 Extension to turbulent flows . . . 6
  - 1.3.1 RANS equations . . . 6
  - 1.3.2 Frozen eddy viscosity . . . 7
  - 1.3.3 Eddy viscosity fluctuations and sensitivity analysis . . . 8
- 1.4 Linearization strategies . . . 9
  - 1.4.1 Continuous framework . . . 9
  - 1.4.2 Discrete framework . . . 10
- 1.5 Scope of the study . . . 11
  - 1.5.1 Generic method using finite differences . . . 11
  - 1.5.2 Linear dynamics and passive control of turbulent flows . . . 11
- 1.6 Plan . . . 12

2 Global stability analysis in a discrete framework **13**
- 2.1 Jacobian matrix . . . 13
- 2.2 Oscillators . . . 14
  - 2.2.1 Unstable modes . . . 14
  - 2.2.2 Sensitivity gradients of the unstable eigenvalue . . . 15
  - 2.2.3 Comparison with a continuous approach . . . 17
- 2.3 Noise amplifiers . . . 19
  - 2.3.1 Optimal forcing and response . . . 19
  - 2.3.2 Sensitivity gradients of the singular eigenvalue . . . 20
  - 2.3.3 Kinetic energy maximization . . . 22
  - 2.3.4 Forcing restrictions . . . 24
  - 2.3.5 Method summary . . . 25
- 2.4 Concluding remarks . . . 26

3 Numerical aspects **27**
- 3.1 Numerical strategy . . . 27
  - 3.1.1 Explicit storage of matrices with direct inversions . . . 27

3.1.2 On-the-fly computation . . . 29
3.2 Efficient evaluation of matrices with explicit storage . . . 29
3.2.1 Example case . . . 30
3.2.2 Jacobian computation . . . 31
3.2.3 Hessian computation . . . 33
3.2.4 Adequate choice of linearization parameters . . . 34
3.2.5 Adaptation of optimization codes . . . 34
3.3 RANS equations and turbulence models . . . 35
3.3.1 Mean field variables . . . 35
3.3.2 $k-\omega$ model of Wilcox . . . 36
3.3.3 Spalart-Allmaras model . . . 37
3.3.4 Numerical schemes . . . 38
3.3.5 Treatment of boundary conditions . . . 40
3.3.6 Shape optimization code adaptation . . . 40
3.4 Concluding remarks . . . 40

4 Validation on laminar flows 43
4.1 Wake behind a two dimensional cylinder . . . 43
4.1.1 Configuration . . . 43
4.1.2 Critical Reynolds number . . . 45
4.1.3 Direct and adjoint unstable mode . . . 46
4.1.4 Sensitivity gradient to baseflow perturbations . . . 47
4.2 Evolving boundary layer over a flate plate . . . 50
4.2.1 Configuration . . . 50
4.2.2 Optimal gain . . . 52
4.2.3 Mesh convergence . . . 53
4.2.4 Optimal forcing and response . . . 55
4.2.5 Gain sensitivity to baseflow perturbation . . . 56
4.3 Concluding remarks . . . 58

5 Sensitivity analysis of a turbulent compressible flow over a deep cavity 59
5.1 Characterization of the cavity . . . 60
5.1.1 Configuration . . . 60
5.1.2 Baseflow computation . . . 61
5.1.3 Unsteady dynamics . . . 62
5.1.4 Memory cost of Jacobian computation, storage and inversion . . . 63
5.2 Flow dynamics analysis . . . 64
5.2.1 Linear stability versus unsteady simulations . . . 64
5.2.2 Mesh discretization impact on the spectrum . . . 65
5.2.3 Unstable modes analysis . . . 66
5.2.4 Influence of the system of equations . . . 68
5.2.5 Spectrum convergence with the linearization parameter . . . 72
5.2.6 Adjoint modes . . . 73
5.3 Sensitivity analysis . . . 74
5.3.1 Sensitivity gradient to baseflow perturbations $\boldsymbol{\nabla}_{\mathbf{w_b}}\lambda$ . . . 74
5.3.2 Validation of the gradient $\boldsymbol{\nabla}_{\mathbf{w_b}}\lambda$ . . . 76
5.3.3 Steady control . . . 78

5.4 Detailed analysis of the Spalart-Allmaras model . . . 80
5.4.0.1 Discontinuities in the gradient . . . 80
5.4.0.2 Numerical origin . . . 81
5.4.0.3 Corrected gradient . . . 82
5.5 Concluding remarks . . . 85

6 Application cases **87**
6.1 Shock wave/boundary layer interactions . . . 87
6.1.1 Transonic buffet over an airfoil . . . 88
6.1.2 Strong shock over a curved profile . . . 93
6.2 Screech in jets . . . 97
6.3 Concluding remarks . . . 100

7 Towards turbulence model free sensitivity analysis **101**
7.1 Configuration . . . 102
7.2 Flow dynamics . . . 103
7.2.1 Unsteady simulations . . . 103
7.2.2 Meanflow computation . . . 104
7.2.3 Discussion on the choice of a relevant eddy viscosity . . . 105
7.3 Direct and adjoint unstable modes . . . 106
7.4 Sensitivity gradients . . . 107
7.5 Steady control of the flow frequency . . . 109
7.6 Concluding remarks . . . 110

8 Conclusion and perspectives **113**
8.1 Conclusion . . . 113
8.2 Perspectives . . . 116

A Appendix A **119**
A.1 Scalar products definitions . . . 119
A.1.1 Matrix $\mathbf{Q}$ . . . 119
A.1.2 Matrix $\mathbf{Q_e}$ . . . 119

Bibliography **121**

Remerciements

Une page se tourne, 3 ans c'est long, et j'ai beaucoup de personnes à remercier pour leur soutien et leur aide durant cette formidable période passée en thèse.

Denis, je tiens à te remercier chaleureusement pour ces trois années passées à l'Onera, sans toi rien de tout ceci ne serait arrivé. Tu as toujours été présent dans les moments de difficultés, à me soutenir et à m'encourager, tout comme tu as su me féliciter lorsque tout fonctionnait. Je suis très heureux de mon parcours de thèse, qui comme la qualité de ces travaux, te doit indéniablement beaucoup.

Je tiens également à remercier toutes les personnes avec qui j'ai pu interagir et qui m'ont aidé dans la réalisation de cette thèse. Je pense à Jacques Peter et Florent Renac du DSNA, qui m'avez énormément aidé durant ces travaux, sans compter votre temps lorsque j'avais des questions à vous poser, et en portant toujours un regard attentif à mes travaux. Merci pour ces heures de travail à vos côtés et pour vos encouragements. Merci aussi à Olivier Marquet, pour les nombreuses discussions que nous avons pu avoir et les nombreux conseils que tu as pu me donner, ils m'ont toujours été profitables. Merci à Bertrand Michel du DSNA pour tes explications d'elsA et le temps que tu m'as consacré, ainsi qu'à Hervé Bezard et Farid Benyoucef du DMAE pour l'heureuse collaboration que nous avons pu effectuer.

Je remercie respectueusement l'ensemble des membres de mon jury d'avoir accepté de juger mes travaux, Vassilios Theofilis, Jean-Christophe Robinet, Carlo Cossu, Lionel Larchevêque, Philippe Meliga, Florent Renac et Yann Doutreleau. Je suis honnoré d'avoir pu vous présenter mon travail de thèse.

Je remercie par ailleurs Laurent Jacquin et tous les membres du DAFE, pour votre acceuil chaleureux dès mon arrivée et tout au long de ma thèse, je pense à Benjamin, Vincent, Dominique, Claire, Philippe, Serge, et j'en oublie surement. C'est dans une excellente ambiance que j'ai pu réaliser ces travaux et c'est grâce toute l'équipe du DAFE. Une pensée notamment pour les doctorants, la dream-team du bureau 23 Gregory, Laurence et Juanito, les anciens Samuel, Aurélien, Sami, les italiens Claudio, Fulvio, et tous les autres Romain, Adam, Holly, Robin et Samir, merci pour tous ces bons moments passés autour d'un café, d'un tank trouble, où d'un amaro del capo.

Merci aussi à tous mes amis pour m'avoir supporté dans mes moments difficiles et de m'avoir accompagné dans les bons moments. Merci pour votre amitié c'est important pour moi, Thomas, Cyprien, Kevin, Jimmy-Jonathan, Youssef, Stephane, Nicolas, Sylvain, Coco, Sophie, Manon, Marion, Juliette, Aude et tous ceux que j'ai malencontreusement oublié.

Enfin, last but not least, merci à mes parents, ma soeur, mes grand-parents, mes oncles et tantes pour leur inconditionnel support durant ces

3 années parfois difficiles, je n'aurais jamais pu arriver jusqu'ici sans vous, merci de tout mon coeur vous êtes formidables.

Chapter 1

Introduction

1.1 Flow dynamics characterization

1.1.1 Unsteady flows in fluid dynamics

A wide variety of unsteady flows are encountered in practical engineering applications which may lead to undesirable features. The wake behind a cylinder, a simple model for flows around bridge pillars or tall buildings, starts to oscillate for critical Reynolds number. Counter rotating vortices are emitted which propagate downstream forming a Von-Kármán alley as observed in Fig. 1.1(a). Such oscillations induce load vibrations which may weaken the considered structure or lead it to resonance. The flight envelope of a transport airplane is currently limited in the Mach-angle of attack (AoA) plane by the shock-induced buffeting phenomenon on the airfoil. For Mach numbers of the order of 0.8 and high AoAs, the shock located on the suction side of the wing suddenly starts to oscillate (Jacquin et al. [1]), which produces vibrations that are detrimental to the airplane. Similarly, cavity flows which can be encountered in military applications (bomb bays [2]) as well as in transport aircrafts (slat on a multi-element wing configuration [3]) are the site of strong unsteadiness. Sound waves are emitted which are the source of intense noise and structural vibrations, leading to fatigue problems and extensive noise pollution. Under certain conditions, imperfectly expanded jets produce a discrete tone referred to as screech. An example of under expanded jet is depicted in Fig.1.1(b) at the exit of a $F-16$ engine. Screech plays a critical role in the design of advanced aircraft because it can cause sonic fatigue failure (Raman [4]). Elongated structures in the streamwise direction called streaks naturally develop in boundary layers (Cossu et al. [5]). These structures play an important role in the transition scenario to turbulence in boundary layer which results in strong increase of the drag. Linear stability analysis was introduced to analyse this large variety of unsteady flows, and appeared in the last

(a) (b)

FIGURE 1.1: (a): Von-Kármán vortex street behind a cylinder. (b): Under expanded structures with apparent Mach disks in the jet engine exhaust of an $F-16$ Fighting Falcon during takeoff, from Tech. Sgt. Caycee Cook, South Carolina National Guard.

decades as an efficient means to characterize the occurrence of flow unsteadiness, as well as a robust tool to understand the physical mechanisms at stake.

1.1.2 Local and global stability

Linear stability analysis assumes the existence of a stationary solution $\mathbf{w_b}$ of the Navier-Stokes equations upon which a small amplitude unsteady perturbation is added under the form of a normal mode $\mathbf{w} = \hat{\mathbf{w}}e^{\lambda t}$ of spatial structure $\hat{\mathbf{w}}$ and eigenvalue λ. The evolution equations of the perturbation are given by the linearized Navier-Stokes operator $\mathbf{J}$, the so called Jacobian, and the flow is globally unstable if there exists an exponentially growing mode. The local stability analysis was first introduced for parallel flows whose properties only depend on the cross-stream direction. The analysis is said local as a given crosswise profile of the baseflow is considered to model the whole flow configuration. In this context, Huerre and Monkewitz [6] distinguished two types of instabilities: absolute and convective. Absolutely unstable flows correspond to flows for which initial perturbations will grow and perturb the whole configuration at large time scales, while in convectively unstable flows the perturbations are increased but convected downstream. More recently, the increase in computational capabilities enabled the performance of global stability analysis for which no particular assumption are made for the baseflow $\mathbf{w_b}$. In particular, this allowed the exploration of much more complex and realistic geometries. From a global point of view, Huerre and Rossi [7] distinguished 2 particular types of flow dynamics. Oscillators correspond to unstable flows for which there exist at least an unstable eigenvalue λ. The unstable mode will naturally grow imposing its dynamics to the flow, the dynamics is thus intrinsic. Noise amplifiers correspond to stable flows which may strongly amplify initial external perturbations, but the perturbations vanish for large time scales as the flow is stable, their dynamics is extrinsic. This increase of energy in the flow is generally designated as transient growth. An illustration of these two dynamics is depicted Fig.1.2, where we plotted typical evolutions of the flow energy

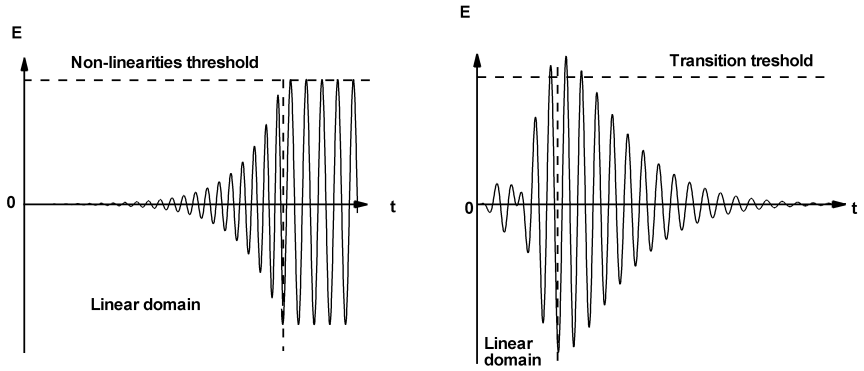

(a) (b)

FIGURE 1.2: Illustration of the total energy evolution in time for (a) an oscillator and (b) a noise-amplifier.

with time. Note that for both types of dynamics, the increase of the flow energy can trigger non-linear effects leading to saturation in the case of oscillators or different type of dynamics for noise-amplifiers (transition to turbulence for example) as emphasized in Fig.1.2. Wakes [8], cavity flows [9], mixing layers [10] are prototypes of oscillators while boundary layers [11], free stream jets [12], two-dimensional backward steps [13, 14] are examples of noise amplifiers. The link between global and local analysis can be stated as follow: oscillators correspond to absolutely unstable flows while noise amplifiers relate to convectively unstable flows. Detailed reviews on the characterization of flow dynamics as oscillators or noise amplifiers can be found in the studies by Godrèche and Manneville [15], Theofilis [16], Sipp et al. [17].

1.1.3 Non-normality of the Jacobian

The non-normality of the Jacobian $\mathbf{J}$ comes from the advection terms in the Navier-Stokes equations and complexifies the study of unsteady flow dynamics. In the case of oscillators, the non-normality induces that the spatial distribution of direct modes and adjoint modes solutions of the adjoint problem are not identical. In particular, as the region of the flow where the spectrum is mostly sensitive to external perturbations corresponds to the recovering region between the direct and adjoint mode, the determination of this area designated as the wave-maker region requires the resolution of the adjoint problem thus the knowledge of the adjoint Jacobian $\mathbf{J}^\dagger$ (Chomaz [18]). In the case of noise amplifiers, the transient energy growth is intrinsically linked to the non-normality of the Jacobian (see studies by Trefethen et al. [19], Farrell and Ioannou [20], Schmid and Henningson [21]). Noise amplifiers are stable flows so that the flow should tend to

the baseflow for large time scales. However, the energy growth may significantly affect the flow dynamics by triggering non linear behavior or transition to turbulence for example. Therefore, the computation and prediction of this quantity is of interest when analysing noise amplifiers unsteadiness. Transient growth assessment requires a non-modal or input/output approach (Schmid and Henningson [21]). This type of analysis can be carried out in the time or frequency domain. In the time domain, the aim is to determine the initial conditions yielding the largest possible energy growth over a finite time horizon (see Blackburn et al. [13], Marquet et al. [22], Cossu et al. [23]), while in the frequency domain the aim is to find the largest possible response $\hat{\mathbf{x}}e^{\omega t}$ to time-periodic external forcing $\hat{\mathbf{f}}e^{\omega t}$ (see Alizard and Robinet [11], Ehrenstein and Gallaire [24]). Both approaches reflect the non-normality of the Jacobian $\mathbf{J}$ and yield a measure quantifying the energy amplifications μ^2 in the flow, which corresponds to the singular values of the resolvent operator $\mathbb{R}_\omega = (i\omega\mathbf{I} - \mathbf{J})^{-1}$.

1.2 Passive control of laminar flows

The underlying mechanisms responsible for flow unsteadiness being more clearly understood, a wide variety of control methods were developed to suppress flow unsteadiness (see reviews by Sipp et al. [17], Gad-el Hak et al. [25], Collis et al. [26]). We will consider here passive control methods in which steady control means are used, such as vortex generators, control cylinders, spoilers, surface roughness.

1.2.1 Sensitivity of oscillators

As the dynamics of oscillators is intrinsically linked to the existence of a unstable modes, flow control methods targeting the unstable modes were developed in order to manipulate these flows [18, 27–29]. In particular, prediction of sensitive regions for passive control is of interest as wind tunnel tests and numerical simulations remain expensive. In his review, Chomaz [18] details how small perturbations of non-normal operators may displace the eigenvalues in a significant manner. In this spirit, Hill [30] computed the impact of a baseflow perturbations onto the flow spectrum in a global framework. Giannetti and Luchini [31] and Giannetti and Luchini [27] further developed this concept introducing the wave-maker region which corresponds to the area responsible for the birth of instabilities. More recently, Marquet et al. [32] extended their results to a global framework. They studied the laminar wake behind a two dimensional cylinder for flow parameters above but near the instability threshold ($Re = 30 - 100$). They proposed to evaluate the impact on the unstable eigenvalue λ of a modification of the baseflow $\mathbf{w_b}$ due to the presence of a stationary force $\mathbf{f}$. To this end, they considered the

gradient of the unstable eigenvalue with respect to baseflow modifications $\nabla_{\mathbf{w_b}}\lambda$, also called the sensitivity gradient to baseflow perturbation, as well as the gradient of the unstable eigenvalue with respect to the introduction of a steady force $\nabla_{\mathbf{f}}\lambda$. Modelling a small cylinder as a steady force, they predicted the most sensitive regions of the flow to stabilize the unstable global mode and compared their results with the experimental study of Strykowski & Sreenivasan [33]. Control maps of both studies overlapped well as can be observed in Fig. 1.3, suggesting that this numerical approach could be a valuable tool in predicting stabilization regions of unsteady flows. These results further encouraged the use of sensitivity analysis to characterise flow dynamics (see for example studies by Pralits et al. [34], Alizard et al. [35], Fani et al. [36], Tammisola [37]).

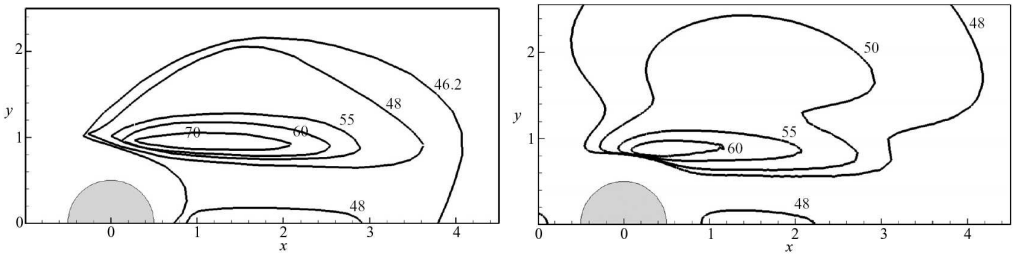

(a) (b)

FIGURE 1.3: Locations where a steady small control cylinder suppresses the unsteadiness of the wake behind a cylinder for several Reynolds numbers. (a): Experimental study of Strykowski and Sreenivasan [33]. (b): Control map of the unstable mode using the sensitivity gradient to a steady force from Marquet et al. [32].

1.2.2 Sensitivity of noise amplifiers

In the case of noise amplifiers, as any real application is subject to external noise, an interesting way to control the flow is to damp the singular eigenvalue μ^2 corresponding to the energy growth. The idea of linking flow spectrum variation to baseflow perturbations for oscillators was extended to noise amplifiers by Sipp et al. [17] and Brandt et al. [38] in a global framework with frequency domain analysis. They defined the sensitivity gradient of the singular eigenvalue to a baseflow perturbation $\nabla_{\mathbf{w_b}}\mu^2$. This gradient gives access to the variation of the amplification gain induced by steady baseflow perturbations. In particular, Brandt et al. [38] studied the Blasius boundary layer at $R_e = 600000$ as a noise amplifier prototype. Two sets of optimal response exist for this configuration: two dimensional Tollmien-Schlichting waves (TS) linked to the Orr mechanism [39] , and three dimensional waves due to the lift-up mechanism (LU) [40]. An example of TS waves developing in a boundary layer can be observed in Fig. 1.4(a). They showed that the TS perturbations were more sensitive to baseflow variations than the LU perturbations, suggesting that the LU perturbations are more robust to flow

configurations. Furthermore, computing the sensitivity gradient of the singular eigenvalue to a steady force $\nabla_{\mathbf{f}}\mu^2$, they showed that the TS perturbations could be damped more easily with a steady force than the LU perturbations.

The gradients $\nabla_{\mathbf{w_b}}\mu^2$ and $\nabla_{\mathbf{f}}\mu^2$ thus carry several valuable information. As any experimental study is subject to noise, they first indicate which regions of the flow should not be subjected to steady perturbations in order to study the natural amplification dynamics of the flow. Second, they depict interesting areas to place control devices, either to damp the amplifier dynamics or to enhance it so as to enforce transition to turbulence for example.

1.3 Extension to turbulent flows

1.3.1 RANS equations

These encouraging results obtained for laminar flow dynamics raised the question of the applicability of such methods for turbulent flows, which are more likely to be encountered in aeronautical applications. Turbulence models remain widely used in this area as the computational cost to solve the Navier-Stokes equations using Direct Numerical Simulation (DNS) drastically increases with the Reynolds number. The Reynolds-Averaged Navier-Stokes equations (RANS) are obtained considering turbulent flows for which scale decoupling assumption holds [9, 41–43]. The dynamics of the large scale structures of the flow may be captured solving the unsteady Reynolds-Averaged Navier Stokes (RANS) equations. The impact of the small scales dynamics onto the large ones is accounted for with an additional viscosity or eddy viscosity μ_t.

The eddy viscosity is generally defined using the Boussinesq hypothesis which in particular links the Reynolds stress tensor to the deformation rate tensor of the flow. As a first modeling (see Townsend [44], Lighthill [45], Lumley [46]), the eddy viscosity was defined as a spatial field that only depends on the coordinate system $\mu_t\left(x, y, z\right)$, in such case the eddy viscosity is said to be frozen [47, 48]. More recently, more subtle methods were developed to define the eddy viscosity using a turbulence model, which in turn introduces one or several turbulent variables along with their corresponding transport equations (see models by Jones and Launder [49], Chien [50], Wilcox [51], Smith [52], Spalart and Allmaras [53]). For example, the classical $k-\epsilon$ turbulence model introduces the turbulent kinetic energy k and energy dissipation ϵ, which allow the definition of the eddy viscosity as a function of the flow variables $\mu_t\left(\rho, k, \epsilon\right)$ (with ρ the density).

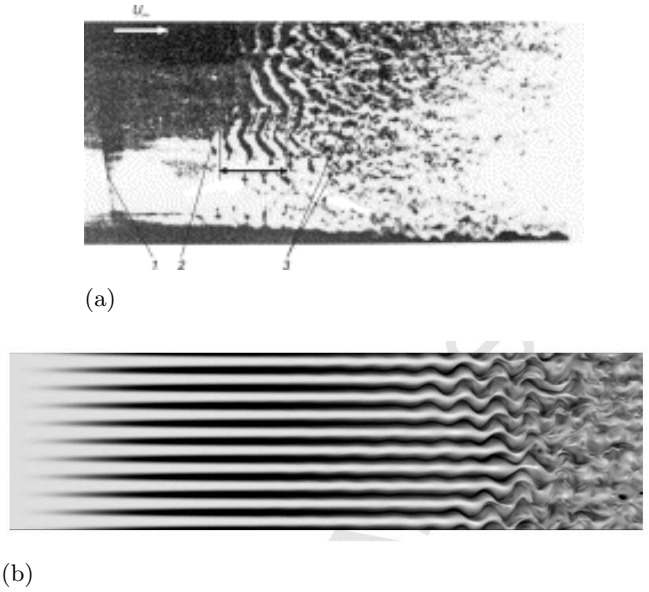

(a)

(b)

FIGURE 1.4: (a): Tollmien-Schlichting waves in a developing boundary layer from Babenko et al. [54]. The flow goes from left to right and is viewed from atop. The arrow indicates the zone of deformation of the TS waves. (b): Visualization in a plane parallel to the wall of streamwise streaks in a channel flow from Buffat et al. [55]. The flow goes from left to right, the streaks become unstable inducing transition to turbulence after a while.

1.3.2 Frozen eddy viscosity

In channel flows, downstream elongated vortices or streaks develop and break down which lead the flow to transition to turbulence, a phenomenon illustrated in Fig. 1.4(b). In their seminal work, Reynolds and Hussain [48] considered the linear stability of the meanflow profile in a turbulent channel flow. They analysed the stability of artificially induced waves and demonstrated the need of an eddy viscosity model μ_t to take into account the impact of the small turbulent scales onto the perturbations dynamics. In particular, Reynolds and Hussain [48] gave a physical meaning to the use of a frozen eddy viscosity model in the linearization process. Indeed, they showed that this choice is justified if the perturbation waves do not impact the characteristic time of turbulent fluctuations. Nevertheless, they observed the flow to be stable which discouraged further research on the subject.

As the role of transient growth was more clearly understood for laminar flows, Butler and Farrell [56] renewed this approach considering optimally amplified perturbations in the time domain. They used the turbulent profile of Reynolds and Tiederman [57] (derived using Cess [47] viscosity model) but performed a laminar analysis of the optimal amplifications. This neglecting of the impact of fine-scale turbulence on large-scale coherent structures in the transient growth process limited their results to final optimization times equal to one eddy turnover timescale. More recently, Cossu et al. [23], Juan

and Jiménez [58], Pujals et al. [59] used the same profile but included the eddy viscosity model in the linearized equations, suggesting that small turbulent scales intervene in the amplification process of external noise into large scale coherent structures. They showed that the optimal energy growth exhibits two peaks corresponding with the development of streaks in the flow. The first peak corresponds to very large structures that scale with the bulk units while the secondary peaks scales in wall unit with streaks located close to the wall. Both scaling overlapped well with experimental results suggesting the relevancy of such an approach to the study of turbulent flows, and lead to further studies using frozen eddy viscosity models (see for example Hwang and Cossu [60, 61], Kitsios et al. [62]).

These studies suggest that turbulence effects, modelled through the use of an eddy viscosity, have to be accounted for when considering linear stability analysis of turbulent flows. Note that in the previous studies, the eddy viscosity does not depend on the flow variable but is a spatial field that only depends on the spatial coordinates. In particular, the eddy viscosity remains constant when linearizing the equations. Such a modeling is thus generally referred to as a frozen eddy viscosity model.

1.3.3 Eddy viscosity fluctuations and sensitivity analysis

Using a turbulence model, the eddy viscosity is coupled to the mean field variables. Hence, the imposed perturbations may include fluctuations of the turbulent variables as well as eddy viscosity fluctuation μ_t'. Such an analysis can be performed using a turbulence model whose equations are also linearized in the stability study. This implies that the impact of the turbulent quantities is taken into account in the perturbations dynamics.

Crouch et al. [63, 64] analysed the buffeting phenomenon on a two dimensional aerofoil. The shock wave starts to oscillate when the angle of attack of the wing and the Mach number reach critical values. They used the one equation turbulence model of Spalart-Allmaras [65] and showed that the time integration of the RANS equations reasonably reproduced the Buffet-onset as well as the frequency of the observed phenomenon. They linearized the RANS equations and showed that the Buffet onset was linked to the occurrence of an unstable global mode whose frequency matched the expected one. In particular, they observed that when using frozen viscosity linearization, they did not find any unstable modes. This suggests that in this case, the propagating wave does have an impact on the turbulent fluctuations time scale (Reynolds and Hussain [48]). Their stability results matched well with numerical simulations and experimental studies regarding the onset of flow unsteadiness as can be observed in Fig. 1.5(a).

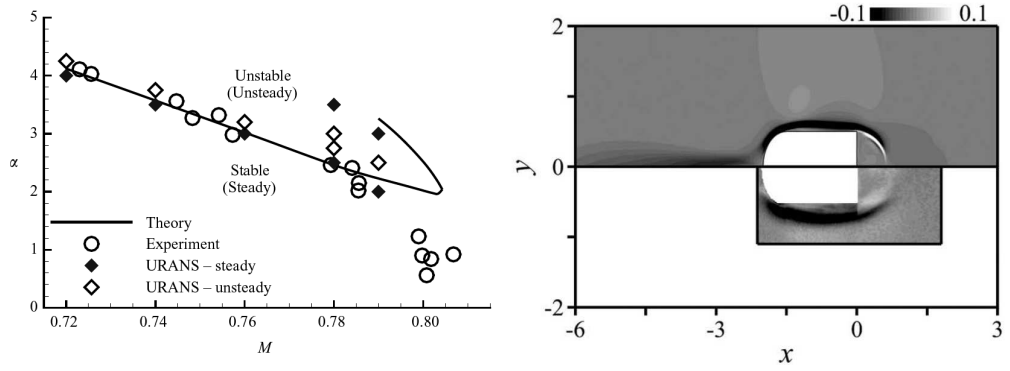

(a) (b)

FIGURE 1.5: (a): Stability diagram of the transonic buffet over an aerofoil computed by Crouch et al. [64], wing incidence α versus Mach number M. (b): Comparison between the linear stability control map of the flow frequency from Meliga et al. [66] (upper part) and the experimental control map of Parezanović and Cadot [67] (lower part), from [66].

More recently, Meliga et al. [66] linearized the incompressible RANS equations using the Spalart-Allmaras model to study the dynamics of the wake behind a D-shaped cylinder at $R_e = 13000$. They found that the meanflow (time average of the unsteady flow) was slightly unstable and that the associated global mode was characterized by a frequency corresponding approximately to the one observed experimentally (Sipp and Lebedev [68]). In the spirit of the work of Marquet et al. [32], they analytically derived the sensitivity gradients of the full system of equations. Using a steady force (modeling the presence of a small cylinder) as a means to modify the meanflow, they computed sensitivity maps indicating where the cylinder would efficiently change the frequency of the unstable mode. They compared their results with the experimental study of Parezanović & Cadot [67] who controlled the same configuration using a small cylinder. Both experimental and numerical control maps of the frequency showed good agreement as can be observed in Fig. 1.5(b).

1.4 Linearization strategies

1.4.1 Continuous framework

These previous results suggest that sensitivity gradients constitute a valuable tool for designing open-loop control strategies for both laminar and turbulent flows. The computation of the sensitivity gradients requires the linearization of the RANS equations, which is generally performed in a continuous framework: the equations are first linearized and the eigenvalue problem is then discretized. Several methods can be used for the discretization of the eigenvalue problem (finite elements, spectral methods ...), a

review of which can be found in Theofilis [16]. As the adjoint quantities are required for the computation of the sensitivity gradients, both direct and adjoint problems have to be derived, and then discretized with potentially a different discretization scheme. This yields some error between direct and adjoint quantities which are thus obtained up to discretization error [69] and some matching has to be performed. Furthermore, when discontinuities such as shock waves are present in the flow, a continuous framework does not automatically yield valid direct and adjoint matrices. Indeed, Giles and Pierce [70] showed that special care must be taken for the linearized and adjoint equations. If not, Crouch et al. [63] showed that the shock discontinuities in the baseflow need first to be smoothed for the linear analysis to be valid. Finally, the sensitivity gradients equations have also to be derived through a second linearization step which may become complex when dealing with compressible flows (Robinet [71]) or RANS equations closed with a turbulence model (Crouch et al. [63], Meliga et al. [66]).

1.4.2 Discrete framework

The linearization can also be performed in a discrete framework: the equations are first discretized and then linearized. Advantages and drawbacks of both frameworks were early studied in the field of optimal shape design methods (Peter and Dwight [72]) and lead to similar results (Giles and Pierce [73], Nadarajah and Jameson [74]). A major advantage of the discrete approach is that the adjoint quantities, which are required to compute the sensitivity gradients, are obtained up to machine precision (De Pando et al. [69]). Furthermore, a discrete approach based on a shock-capturing method and a conservative scheme automatically yields valid direct and adjoint matrices in the case of shocks. The discrete framework is also conceptually simpler, since the Jacobian and adjoint matrices are directly defined from the discretized residual $\mathcal{R}$.

However, in both the continuous and discrete approaches, analytical derivation of the linearized equations remains a difficult task. Indeed, as noted by Peter and Drullion [75], the governing equations may involve complex equations with turbulence models and complex boundary conditions (characteristic boundary conditions [76]). In a discrete framework, the discretization scheme may also include complex spatial discretization techniques (centered schemes with artificial viscosity [77, 78], upwind schemes [79, 80] with limiters [81]). The compressibility of the equations further complexifies the linearization as can be observed in Robinet [71], Theofilis and Colonius [82]. As an example, the analytical derivation of the sensitivity gradients in the case of compressible turbulent RANS equations has not yet been achieved although this system of equations is more likely to represent practical aeronautical cases.

1.5 Scope of the study

1.5.1 Generic method using finite differences

We propose in this study a fully discrete framework where the linearized equations are obtained from a finite difference method rather than analytical derivation. To this end, we define the direct and adjoint problem as well as the sensitivity gradients in a discrete framework. As the sensitivity gradients have only been defined up to now in a continuous framework, their discrete derivation is one of the contribution of this study. Furthermore, we show how the direct and adjoint global modes as well as the sensitivity gradients can be obtained solely from residual evaluations. In particular, we demonstrate that the sensitivity gradients are linked to the Hessian of the governing equations. The finite difference method used to linearize the equations avoids complex analytical treatments and can easily handle different system of equations and different spatial discretization schemes. All the complexity (equations, boundary conditions, spatial discretization scheme) is actually accounted for in the evaluation of the residual equation $\mathcal{R}$, which is available in all numerical codes. Hence, we show how a numerical code can be used in a black box manner to compute global modes, adjoint global modes and sensitivity gradients. The discrete framework based on finite difference evaluations therefore yields a highly flexible strategy which is important since several turbulence models and discretization schemes are generally required to cover a variety of configurations (separation, mixing layers, boundary layers, ...) and regimes (subsonic, transonic, supersonic). Of course, the price to pay is that the various quantities involved in the analysis (Jacobian, adjoint matrix, global modes, adjoint global modes, sensitivity gradients) are computed with some error due to the inherent approximations involved in a finite difference method [69].

1.5.2 Linear dynamics and passive control of turbulent flows

In most turbulent flows, low frequency unsteadiness are generally responsible for undesirable features such as load fluctuations, vibrations. The unsteady RANS equations and the turbulence models used to close the system are designed to reproduce these large scale fluctuations, these models relying on the definition of an eddy viscosity μ_t. We propose in this study to perform a linear stability analysis of the RANS equations. From a physical standpoint, a first goal of this work is to analyse the stability of the low frequency structures of turbulent flows. In particular, the link between the flow unsteadiness observed while solving the unsteady RANS equations and the oscillator

(existence of unstable mode) or noise amplifier (transient growth) dynamics of the turbulent flow might be assessed. Furthermore, the genericity of the method which allows the use of several turbulence models may also be useful to analyse the impact of these models and their relevancy to reproduce the flow physics. For example, the impact of a frozen or fluctuating eddy viscosity in the linearization process may be analysed, as this choice may significantly affects the flow dynamics (Crouch et al. [63] found no buffeting mode using frozen eddy viscosity). Finally, the computation of turbulent compressible sensitivity gradients corresponds to the main contribution of this study. It enables the a priori determination of interesting areas where steady control means may significantly affect the flow unsteadiness, and constitutes a first step in view of designing open loop control strategies for compressible turbulent flows.

1.6 Plan

We first introduce in Chapter 2 the stability theory background in a discrete framework. The Jacobian matrix $\mathbf{J}$ is defined, as well as the sensitivity gradients $\nabla_{\mathbf{w_b}}\lambda$ and $\nabla_{\mathbf{f}}\lambda$,$\nabla_{\mathbf{w_b}}\mu^2$. The explicit formulation of the gradients are then derived for both oscillators and noise amplifiers. In Chapter 3, we present several strategies that can be used to compute the gradients and detail the one used throughout this study. In particular, we explain how the current method can be adapted to matrix free methods. The computational technique using efficient residual evaluations to obtain the Jacobian matrix and the gradients is then described. An adaptation of shape optimization codes to compute the sensitivity gradients will also be proposed. At last, the governing equations as well as the numerical schemes are detailed. As first validation step, we consider two laminar flows in Chapter 4, an oscillator and a noise amplifier, and reproduce results previously obtained by Marquet et al. [32], Brandt et al. [38]. Chapter 5 is devoted to the computation and validation of the sensitivity gradients for a compressible turbulent flow. Numerical validation, convergence tests, genericity of the methods are tested on a deep cavity configuration at Mach number 0.80 and Reynolds number 860000, which was experimentally studied by Forestier et al. [83] and numerically by Larchevêque et al. [84]. Eexamples of other laminar and turbulent applications such as transonic buffet, shock-boundary layers interactions, and jets are introduced in Chapter 6. Finally, preliminary results computed for a turbulent flow over a D-shaped cylinder are presented in Chapter 7, enhancing perspectives for the future.

Chapter 2

Global stability analysis in a discrete framework

This Chapter is devoted to the definition of the theoretical background required to perform a stability analysis in a discrete framework. The Jacobian $\mathbf{J}$ is first introduced in Section 2.1 and the distinction between oscillator and noise amplifier dynamics is detailed. In Section 2.2, the sensitivity gradients are defined in the case of oscillators. The stability and sensitivity analyses of noise amplifiers are finally discussed in Section 2.3.

2.1 Jacobian matrix

After spatial discretization, the governing equations can be recast in the general following conservative form:

$$\frac{d\mathbf{w}}{dt} = \mathcal{R}\left(\mathbf{w}\right), \tag{2.1}$$

where $\mathbf{w} \in \mathbb{R}^N$ represents the set of conservative variables describing the flow at each spatial location of the mesh and $\mathcal{R} : \Omega \in \mathbb{R}^{\mathrm{N}} \rightarrow \mathbb{R}^{\mathrm{N}}$ is $\mathcal{C}^2$ over Ω and represents the discrete residuals. Using finite volume or finite difference methods, the dimension of $\mathbf{w}$ corresponds to the number of cells or nodes in the mesh times the number of variables. Note that all boundary conditions are included in the discrete operator $\mathcal{R}$.

We assume the existence of a steady solution $\mathbf{w_b} \in \mathbb{R}^N$ to this system referred to as the baseflow and defined by the discrete equation:

$$\mathcal{R}\left(\mathbf{w_b}\right) = \mathbf{0}. \tag{2.2}$$

In the case of governing equations involving a turbulence model, it is worth mentioning that such a baseflow takes into account the Reynolds stresses involved in the turbulence model, but not those related to possible low-frequency (and large-scale) perturbations, which are accounted for by the time-integration in Eq. (2.1). In so far, the above defined baseflow is not strictly speaking a mean-flow (even though it incorporates some mean-flow effects due to high-frequency turbulence) and may therefore be considered as a valid candidate for a stability analysis.

The stability of the baseflow is probed by analysing the evolution of a small amplitude perturbation $\epsilon\mathbf{w}'$ superimposed on the baseflow: $\mathbf{w} = \mathbf{w_b} + \epsilon\mathbf{w}'$, with $\epsilon \ll 1$. Note that in the case of governing equations involving a turbulence model, the perturbation also involves variations of the turbulent quantities. The equation governing the perturbation is given by the linearization to the first order of the discretized equations in (2.1):

$$\frac{d\mathbf{w}'}{dt} = \mathbf{J}\mathbf{w}'. \tag{2.3}$$

The Jacobian operator $\mathbf{J} \in \mathbb{R}^{\mathrm{N}\times\mathrm{N}}$ corresponds to the linearization of the discrete Navier-Stokes operator $\mathcal{R}$ around the baseflow $\mathbf{w_b}$:

$$\mathbf{J}_{ij} = \left.\frac{\partial \mathcal{R}_i}{\partial \mathbf{w}_j}\right|_{\mathbf{w}=\mathbf{w_b}}, \tag{2.4}$$

where $\mathcal{R}_i$ designates the i^{th} component of the residual, which is a priori a function of all unknowns $\mathbf{w}_j$ in the mesh. If we use finite volume or finite difference methods, then the spatial discretization stencil is compact and the i^{th} component of the residual only depends on few neighbouring unknowns. Hence, $\mathbf{J}$ is a sparse matrix in such cases. Note that the proposed formalism does not assume homogeneity of the fluctuations in a given direction. For three dimensional configuration, this formalism corresponds to the TriGlobal linear stability analysis as introduced by Theofilis [85].

Remark: We assumed the residual operator $\mathcal{R}$ to be $\mathcal{C}^2(\Omega)$ for the sensitivity gradients to be defined. Strictly speaking, the stability analysis only requires the considered system of equations to be differentiable, that is $\mathcal{R} \in \mathcal{C}^1(\Omega)$.

2.2 Oscillators

2.2.1 Unstable modes

We consider perturbations under the form of normal modes $\mathbf{w}' = \hat{\mathbf{w}}e^{\lambda t}$, where $\lambda = \sigma + i\omega$ describes its temporal behaviour — σ is the amplification rate and ω the frequency —

and $\hat{\mathbf{w}} \in \mathbb{C}^N$ its spatial structure. Then Eq. (2.3) may be recast into the following eigenvalue problem:

$$\mathbf{J}\hat{\mathbf{w}} = \lambda\hat{\mathbf{w}}. \tag{2.5}$$

If at least one of the eigenvalues λ exhibits a positive growth rate σ, then the baseflow $\mathbf{w_b}$ is unstable. We refer to unstable flows as oscillators since the unstable mode will naturally grow and impose its dynamics to the flow regardless of any external perturbations.

As the natural flow unsteadiness may be linked to the existence of one or several unstable modes, the stabilization of the unstable modes is expected to lead to the suppression of the flow unsteadiness. The sensitivity gradients that we will introduce in the following carry valuable information on locations were steady control means might stabilize the unstable modes thus suppress flow unsteadiness.

2.2.2 Sensitivity gradients of the unstable eigenvalue

Let us consider a particular eigenmode (λ,$\hat{\mathbf{w}}$). Following previous studies (Hill [30], Marquet et al. [32], Bottaro et al. [86]), this eigenmode may be considered as a function of the baseflow $\mathbf{w_b}$, since the Jacobian matrix has been obtained by linearization of the governing equations near the baseflow. Hence, a small baseflow perturbation $\boldsymbol{\delta}\mathbf{w_b}$ generates a small variation of the eigenvalue $\delta\lambda$, which can be written as:

$$\delta\lambda = \langle \boldsymbol{\nabla}_{\mathbf{w_b}}\lambda, \boldsymbol{\delta}\mathbf{w_b} \rangle . \tag{2.6}$$

This expression defines the gradient $\boldsymbol{\nabla}_{\mathbf{w_b}}\lambda \in \mathbb{C}^{\mathrm{N}}$, called the sensitivity of the eigenvalue to baseflow modifications. It is a complex vector field, the real and imaginary parts respectively dealing with the sensitivity of the amplification rate $\boldsymbol{\nabla}_{\mathbf{w_b}}\sigma$ and the frequency $\boldsymbol{\nabla}_{\mathbf{w_b}}\omega$. Note that in the case of governing equations including a turbulence model, one may analyse the sensitivity of the global mode to variations of turbulent scales of the baseflow. In Eq. (2.6), the discrete inner product $\langle\cdot\rangle$ refers to the Euclidian inner-product in $\mathbb{C}^{\mathrm{N}}$:

$$\langle \mathbf{u}, \mathbf{v} \rangle = \mathbf{u}^*\mathbf{v}, \tag{2.7}$$

where * denotes conjugate transpose. The associated norm $\|\mathbf{u}\| = \sqrt{\langle \mathbf{u}, \mathbf{u} \rangle}$ will be used in the following.

We now derive an explicit expression of $\boldsymbol{\nabla}_{\mathbf{w_b}}\lambda$. Note again that this has been done up to now in a continuous framework, while the goal of the present study is to introduce the discrete one. Considering a small baseflow variation $\boldsymbol{\delta}\mathbf{w_b}$, the eigenvalue problem in

Eq. (2.5) is perturbed and becomes to the first order:

$$\boldsymbol{\delta}\mathbf{J}\hat{\mathbf{w}} + \mathbf{J}\boldsymbol{\delta}\hat{\mathbf{w}} = \delta\lambda\hat{\mathbf{w}} + \lambda\boldsymbol{\delta}\hat{\mathbf{w}}. \tag{2.8}$$

We then multiply the previous equation with a complex vector $\tilde{\mathbf{w}}^*$ such that:

$$\tilde{\mathbf{w}}^*\mathbf{J}\boldsymbol{\delta}\hat{\mathbf{w}} = \tilde{\mathbf{w}}^*\lambda\boldsymbol{\delta}\hat{\mathbf{w}}. \tag{2.9}$$

Hence, $\tilde{\mathbf{w}} \in \mathbb{C}^N$ can be taken as the solution of the adjoint problem:

$$\mathbf{J}^*\tilde{\mathbf{w}} = \lambda^*\tilde{\mathbf{w}} \quad \text{with} \quad \langle\tilde{\mathbf{w}},\hat{\mathbf{w}}\rangle = 1. \tag{2.10}$$

Finally, Eq. (2.8) becomes:

$$\tilde{\mathbf{w}}^*\boldsymbol{\delta}\mathbf{J}\hat{\mathbf{w}} = \delta\lambda\tilde{\mathbf{w}}^*\hat{\mathbf{w}} = \delta\lambda. \tag{2.11}$$

As a consequence, we can link an arbitrary variation of the Jacobian $\boldsymbol{\delta}\mathbf{J}$ to a variation of the eigenvalue $\delta\lambda$ with:

$$\delta\lambda = \langle\tilde{\mathbf{w}},\, \boldsymbol{\delta}\mathbf{J}\hat{\mathbf{w}}\rangle\,, \tag{2.12}$$

where $\tilde{\mathbf{w}}$ is the adjoint global mode solution of the adjoint eigenproblem. If $\boldsymbol{\delta}\mathbf{J}$ corresponds to a variation of the Jacobian induced by a variation of the baseflow $\boldsymbol{\delta}\mathbf{w_b}$, then:

$$\boldsymbol{\delta}\mathbf{J}\hat{\mathbf{w}} = \left.\frac{\partial(\mathbf{J}\hat{\mathbf{w}})}{\partial\mathbf{w}}\right|_{\mathbf{w}=\mathbf{w_b}} \boldsymbol{\delta}\mathbf{w_b}, \tag{2.13}$$

where the global mode $\hat{\mathbf{w}}$ is assumed to be frozen. This expression may be written in a different manner using the Hessian $\mathbf{H}$ of $\mathcal{R}$:

$$\boldsymbol{\delta}\mathbf{J}\hat{\mathbf{w}} = \mathbf{H}(\hat{\mathbf{w}}, \boldsymbol{\delta}\mathbf{w_b}). \tag{2.14}$$

Here $\mathbf{H}\,(\mathbf{u},\mathbf{v}) \in \mathbb{C}^{\mathrm{N}}$ designates the vector $\mathbf{z}$ such that $\mathbf{z}_i = \sum_{j,k} \mathbf{H}_{ijk}\mathbf{u}_j\mathbf{v}_k$, with:

$$\mathbf{H}_{ijk} = \left.\frac{\partial^2\mathcal{R}_i}{\partial\mathbf{w}_j\partial\mathbf{w}_k}\right|_{\mathbf{w}=\mathbf{w_b}}. \tag{2.15}$$

Similarly to the discussion for the Jacobian $\mathbf{J}$, if compact differential stencils are used, then for each component i only few values of $\mathbf{H}_{ijk}$ are non-zero.

Let us introduce the matrix $\mathbf{H}' \in \mathbb{C}^{\mathrm{N}\times\mathrm{N}}$ such that $\mathbf{H}'\boldsymbol{\delta}\mathbf{w_b} = \mathbf{H}(\hat{\mathbf{w}}, \boldsymbol{\delta}\mathbf{w_b})$ for all $\boldsymbol{\delta}\mathbf{w_b}$. Hence:

$$\mathbf{H}'_{ik} = \sum_j \mathbf{H}_{ijk}\hat{\mathbf{w}}_j = \langle\mathbf{e_i},\mathbf{H}(\hat{\mathbf{w}}, \mathbf{e}_k)\rangle\,. \tag{2.16}$$

Here, $\mathbf{e}_i$ denotes the unit vector on the i^{th} component of the canonical basis of $\mathbb{R}^N$. Equation (2.14) may then be rewritten as:

$$\boldsymbol{\delta}\mathbf{J}\hat{\mathbf{w}} = \mathbf{H}'\boldsymbol{\delta}\mathbf{w_b}. \tag{2.17}$$

Introducing Eq. (2.17) into (2.12), we have:

$$\delta\lambda = \left\langle \tilde{\mathbf{w}}, \mathbf{H}'\boldsymbol{\delta}\mathbf{w_b} \right\rangle = \left\langle \mathbf{H}'^{*}\tilde{\mathbf{w}}, \boldsymbol{\delta}\mathbf{w_b} \right\rangle. \tag{2.18}$$

If we identify this expression with Eq. (2.6), we obtain the following expression of the gradient:

$$\boldsymbol{\nabla}_{\mathbf{w_b}}\lambda = \mathbf{H}'^{*}\tilde{\mathbf{w}}. \tag{2.19}$$

In the view of open-loop control that aims at stabilizing the unstable global modes, we will consider control devices that act by adding volumic source terms to the Navier-Stokes equations. For example, any object in the flow may be represented as a force, while heating or cooling is a source term in the energy equation. If a turbulence model is considered in the governing equations, then control devices that locally modify the turbulent scales of the flow may also be considered. In the following, we consider the impact of a small amplitude source term $\boldsymbol{\delta}\mathbf{f} \in \mathbb{R}^N$, which modifies the baseflow such that $\mathcal{R}\left(\mathbf{w_b} + \boldsymbol{\delta}\mathbf{w_b}\right) + \boldsymbol{\delta}\mathbf{f} = \mathbf{0}$. Linearising this expression about $\mathbf{w_b}$, we obtain the baseflow modifications due to the small amplitude source term: $\boldsymbol{\delta}\mathbf{w_b} = -\mathbf{J}^{-1}\boldsymbol{\delta}\mathbf{f}$. Rewriting equation (2.18), we obtain:

$$\delta\lambda = \left\langle \mathbf{H}'^{*}\tilde{\mathbf{w}}, -\mathbf{J}^{-1}\boldsymbol{\delta}\mathbf{f} \right\rangle = \left\langle -\mathbf{J}^{*-1}\mathbf{H}'^{*}\tilde{\mathbf{w}}, \boldsymbol{\delta}\mathbf{f} \right\rangle. \tag{2.20}$$

The sensitivity of the eigenvalue to the introduction of a source term $\boldsymbol{\nabla}_{\mathbf{f}}\lambda \in \mathbb{C}^N$, which links the eigenvalue variation $\delta\lambda$ to the steady source term $\boldsymbol{\delta}\mathbf{f}$, is thus given by:

$$\delta\lambda = \langle \boldsymbol{\nabla}_{\mathbf{f}}\lambda, \boldsymbol{\delta}\mathbf{f} \rangle \quad \text{with} \quad \boldsymbol{\nabla}_{\mathbf{f}}\lambda = -\mathbf{J}^{*-1}\boldsymbol{\nabla}_{\mathbf{w_b}}\lambda. \tag{2.21}$$

The impact of a small amplitude steady source term on the flow spectrum can therefore be predicted a priori and control maps can be obtained beforehand.

2.2.3 Comparison with a continuous approach

We used up to now the canonical inner product (2.7). Yet, to give physical meaning to the gradient so as to allow comparisons of results (if available) with those obtained from a continuous approach, it may be useful to choose another inner-product, based on a

positive definite hermitian matrix $\mathbf{Q}$ such that:

$$\langle \mathbf{u},\mathbf{v} \rangle|_{\mathbf{Q}} = \mathbf{u}^* \mathbf{Q} \mathbf{v}, \tag{2.22}$$

with the corresponding norm $\|\mathbf{u}\|_{\mathbf{Q}} = \sqrt{\langle \mathbf{u},\mathbf{u} \rangle|_{\mathbf{Q}}}$. The definition of $\mathbf{Q}$ is given in Appendix A.1. Based on this new inner-product, the sensitivities may be defined as follows

$$\delta\lambda = < \boldsymbol{\nabla}_{\mathbf{w_b}} \lambda|_{\mathbf{Q}} , \boldsymbol{\delta} \mathbf{w_b} > \Big|_{\mathbf{Q}} \tag{2.23}$$

$$= < \boldsymbol{\nabla}_{\mathbf{f}} \lambda|_{\mathbf{Q}} , \boldsymbol{\delta} \mathbf{f} > \Big|_{\mathbf{Q}} , \tag{2.24}$$

and one straightforwardly obtains:

$$\boldsymbol{\nabla}_{\mathbf{w_b}} \lambda|_{\mathbf{Q}} = \mathbf{Q}^{-1} \boldsymbol{\nabla}_{\mathbf{w_b}} \lambda \tag{2.25}$$

$$\boldsymbol{\nabla}_{\mathbf{f}} \lambda|_{\mathbf{Q}} = \mathbf{Q}^{-1} \boldsymbol{\nabla}_{\mathbf{f}} \lambda. \tag{2.26}$$

For sake of completeness, the adjoint global mode associated to this new inner-product is:

$$\tilde{\mathbf{w}}|_{\mathbf{Q}} = \mathbf{Q}^{-1} \tilde{\mathbf{w}}. \tag{2.27}$$

To sump up, in order to compute the sensitivity gradients, we need to compute:

1. unstable direct global modes $\hat{\mathbf{w}}$ based on the discrete Jacobian $\mathbf{J}$ (Eq. (2.5));
2. unstable adjoint global modes $\tilde{\mathbf{w}}$ based on the discrete adjoint Jacobian $\mathbf{J}^*$ (Eq. (2.10));
3. $\mathbf{H'}^* \tilde{\mathbf{w}}$ (see Eq. (2.16) for the definition of $\mathbf{H'}$) to obtain the sensitivity of the global mode to baseflow modifications $\boldsymbol{\nabla}_{\mathbf{w_b}} \lambda$ (Eq. (2.19));
4. $-\mathbf{J}^{*-1} \boldsymbol{\nabla}_{\mathbf{w_b}} \lambda$ to obtain the sensitivity of the global mode to the introduction of a steady source term $\boldsymbol{\nabla}_{\mathbf{f}} \lambda$ (Eq. (2.21)).
5. $\boldsymbol{\nabla}_{\mathbf{w_b}} \lambda|_{\mathbf{Q}} = \mathbf{Q}^{-1} \boldsymbol{\nabla}_{\mathbf{w_b}} \lambda$ (Eq. (2.25)) and $\boldsymbol{\nabla}_{\mathbf{f}} \lambda|_{\mathbf{Q}} = \mathbf{Q}^{-1} \boldsymbol{\nabla}_{\mathbf{f}} \lambda$ (Eq. (2.26)) to obtain sensitivities with a physically relevant inner-product (2.22).

2.3 Noise amplifiers

2.3.1 Optimal forcing and response

If the Jacobian matrix $\mathbf{J}$ does not have unstable eigenvalues in (2.5), then the baseflow is stable. However, the flow may exhibit transient growth due to the non-normality of the Jacobian matrix (Trefethen et al. [19], Farrell and Ioannou [20], Schmid and Henningson [21]). As stated in Chapter 1, the quantification of transient growth is of importance as it may significantly affect the flow dynamics.

Noise amplifiers dynamics can be analysed by considering the response $\mathbf{x}$ of the baseflow to a small amplitude forcing $\mathbf{f}$, in particular we have:

$$\frac{d\mathbf{x}}{dt} = \mathcal{R}\left(\mathbf{w_b} + \mathbf{x}\right) + \mathbf{f}. \tag{2.28}$$

Considering an harmonic forcing $\mathbf{f} = \hat{\mathbf{f}}e^{i\omega t}$ with $\hat{\mathbf{f}} \in \mathbb{C}^N$ and looking for a response with similar structure $\mathbf{x} = \hat{\mathbf{x}}e^{i\omega t}$ with $\hat{\mathbf{x}} \in \mathbb{C}^N$, we linearize Eq. (2.28) to obtain:

$$\hat{\mathbf{x}} = \mathscr{R}_\omega \hat{\mathbf{f}}, \tag{2.29}$$

where $\mathscr{R}_\omega = (i\omega\mathbf{I} - \mathbf{J})^{-1}$ is referred to as the global resolvent matrix and $\mathbf{I}$ is the identity matrix. The global resolvent matrix $\mathscr{R}_\omega \in \mathbb{C}^{\mathrm{N}\times\mathrm{N}}$ is defined for any real frequency ω since all eigenvalues of $\mathbf{J}$ are strictly damped. Considering the optimal forcing $\hat{\mathbf{f}}$ that maximizes the energetic gain $\mu^2 \in \mathbb{R}$ of the response, we have:

$$\mu^2 = \sup_{\hat{\mathbf{f}}} \frac{\langle \hat{\mathbf{x}}, \hat{\mathbf{x}} \rangle}{\left\langle \hat{\mathbf{f}}, \hat{\mathbf{f}} \right\rangle}. \tag{2.30}$$

Inserting Eq. (2.29) into Eq. (2.30), we obtain:

$$\mu^2 = \frac{\hat{\mathbf{f}}^* \mathscr{R}_\omega^* \mathscr{R}_\omega \hat{\mathbf{f}}}{\hat{\mathbf{f}}^* \hat{\mathbf{f}}}. \tag{2.31}$$

The previous ratio is a Rayleigh quotient since $\mathscr{R}_\omega^* \mathscr{R}_\omega$ is an Hermitian matrix. The optimal gain μ^2 is real and corresponds to the singular value of the global resolvent $\mathscr{R}_\omega$:

$$\mathscr{R}_\omega^* \mathscr{R}_\omega \hat{\mathbf{f}} = \mu^2 \hat{\mathbf{f}}, \tag{2.32}$$

with $\hat{\mathbf{f}}$ the corresponding optimal forcing. We will denote the maximum gain μ_1 obtained for optimal forcing $\hat{\mathbf{f_1}}$ and response $\hat{\mathbf{x_1}}$. The gain function μ^2 which varies with the frequency ω corresponds to the transfer function of the flow and quantifies if the flow acts like a high, low or broad band filter.

Since the eigenvalue problem (2.32) is Hermitian, the set of normalized optimal forcing $\left(\hat{\mathbf{f}}_\mathbf{i}\right)$ (one set per frequencies ω) defines an orthonormal basis which is adequate to represent the forcing space. The set of optimal responses $(\hat{\mathbf{x}}_\mathbf{i})$ of unit norm can be obtained by solving $\hat{\mathbf{x}}_\mathbf{i} = \mu_i^{-1}\mathscr{R}_\omega\hat{\mathbf{f}}_\mathbf{i}$, and forms an orthonormal basis of the response space. Therefore, if we are given the structure of a forcing term $\hat{\mathbf{F}}$ at the frequency ω, the structure of the response $\hat{\mathbf{X}}$ is obtained using:

$$\hat{\mathbf{X}} = \sum_j \mu_j \left\langle \hat{\mathbf{f}}_\mathbf{j}, \hat{\mathbf{F}} \right\rangle \hat{\mathbf{x}}_\mathbf{j}. \tag{2.33}$$

The corresponding energy response is readily obtained from:

$$\left\langle \hat{\mathbf{X}}, \hat{\mathbf{X}} \right\rangle = \sum_j \mu_j^2 \left\langle \hat{\mathbf{f}}_\mathbf{j}, \hat{\mathbf{F}} \right\rangle^2. \tag{2.34}$$

A consequence of Eq. (2.34) is that to maximize the flow response, the external forcing should drive the flow with a structure as close as possible to the optimal forcing $\hat{\mathbf{f}}_\mathbf{1}$, leading to a response close to $\hat{\mathbf{x}}_\mathbf{1}$. In particular, the dynamical flow response can be a priori predicted using this set of optimal forcing and response given by the number of frequency ω tested. Several studies have shown that a reduced number of optimal forcing and response are sufficient to predict the flow dynamics to external noise (see Dergham et al. [87, 88]).

As aeronautical cases are noisy by nature (turbulence, structural vibrations), one way to control the flow unsteadiness would be to damp the amplifications μ^2 of the external noise. As for the oscillators, we will introduce the sensitivity gradients for noise amplifiers which indicate areas where steady control means would modify the gain μ^2.

2.3.2 Sensitivity gradients of the singular eigenvalue

Let us consider a particular optimal set $\left(\mu^2, \hat{\mathbf{x}}, \hat{\mathbf{f}}\right)$. These quantities are linked to the baseflow through the Jacobian $\mathbf{J}$ in the global resolvent $\mathscr{R}_\omega$. We can hence define the sensitivity gradient of the singular value to a baseflow perturbation $\boldsymbol{\nabla}_{\mathbf{w_b}}\mu^2$ such that a small baseflow perturbation $\boldsymbol{\delta}\mathbf{w_b}$ generates a small variation of the singular value $\delta\mu^2$ with:

$$\delta\mu^2 = \left\langle \boldsymbol{\nabla}_{\mathbf{w_b}}\mu^2, \boldsymbol{\delta}\mathbf{w_b} \right\rangle. \tag{2.35}$$

Note that here the gradient $\boldsymbol{\nabla}_{\mathbf{w_b}}\mu^2 \in \mathbb{R}^N$ is a real vector field. We now derive an explicit expression of $\boldsymbol{\nabla}_{\mathbf{w_b}}\mu^2$ in a discrete framework which has been done up to now in a continuous framework (Sipp et al. [17], Brandt et al. [38]). The equations governing

our optimal forcing and response can be recast in the following form:

$$\hat{\mathbf{x}} = \mu^2 \mathscr{R}_\omega^{-1*} \hat{\mathbf{f}}, \tag{2.36}$$

$$\hat{\mathbf{f}} = \mathscr{R}_\omega^{-1} \hat{\mathbf{x}}. \tag{2.37}$$

Perturbing Eqs. (2.36)&(2.37) with a small baseflow variation we have to the first order, using $\delta \mathscr{R}_\omega^{-1} = -\boldsymbol{\delta}\mathbf{J}$:

$$\boldsymbol{\delta}\hat{\mathbf{x}} = \delta\mu^2 \mathscr{R}_\omega^{-1*} \hat{\mathbf{f}} - \mu^2 \boldsymbol{\delta}\mathbf{J}^* \hat{\mathbf{f}} + \mu^2 \mathscr{R}_\omega^{-1*} \boldsymbol{\delta}\hat{\mathbf{f}}, \tag{2.38}$$

$$\boldsymbol{\delta}\hat{\mathbf{f}} = -\boldsymbol{\delta}\mathbf{J}\hat{\mathbf{x}} + \mathscr{R}_\omega^{-1} \boldsymbol{\delta}\hat{\mathbf{x}}. \tag{2.39}$$

We then respectively multiply Eqs. (2.38)&(2.39) with a complex vector $\tilde{\mathbf{x}}^*$ and $\tilde{\mathbf{f}}^*$ and sum the obtained equations to get:

$$\left[\tilde{\mathbf{x}}^* - \tilde{\mathbf{f}}^* \mathscr{R}_\omega^{-1}\right] \boldsymbol{\delta}\hat{\mathbf{x}} + \left[\tilde{\mathbf{f}}^* - \mu^2 \tilde{\mathbf{x}}^* \mathscr{R}_\omega^{-1*}\right] \boldsymbol{\delta}\hat{\mathbf{f}} = \delta\mu^2 \tilde{\mathbf{x}}^* \mathscr{R}_\omega^{-1*} \hat{\mathbf{f}} - \mu^2 \tilde{\mathbf{x}}^* \boldsymbol{\delta}\mathbf{J}^* \hat{\mathbf{f}} - \tilde{\mathbf{f}}^* \boldsymbol{\delta}\mathbf{J}\hat{\mathbf{x}}. \tag{2.40}$$

We look for $\tilde{\mathbf{x}}^*$ and $\tilde{\mathbf{f}}^*$ such that:

$$\tilde{\mathbf{x}}^* = \tilde{\mathbf{f}}^* \mathscr{R}_\omega^{-1}, \tag{2.41}$$

$$\tilde{\mathbf{f}}^* = \mu^2 \tilde{\mathbf{x}}^* \mathscr{R}_\omega^{-1*}, \tag{2.42}$$

which yields:

$$\tilde{\mathbf{x}} = \mathscr{R}_\omega^{-1*} \tilde{\mathbf{f}}, \tag{2.43}$$

$$\tilde{\mathbf{f}} = \mu^2 \mathscr{R}_\omega^{-1} \tilde{\mathbf{x}}, \tag{2.44}$$

$$\tilde{\mathbf{f}} = \mu^2 \mathscr{R}_\omega^{-1} \mathscr{R}_\omega^{-1*} \tilde{\mathbf{f}}. \tag{2.45}$$

As the singular vectors of $\mathscr{R}_\omega$ are orthogonal we thus have, noting α a complex constant:

$$\tilde{\mathbf{f}} = \alpha \hat{\mathbf{f}}, \tag{2.46}$$

$$\tilde{\mathbf{x}} = \alpha \mathscr{R}_\omega^{-1*} \hat{\mathbf{f}} = \frac{\alpha}{\mu^2} \hat{\mathbf{x}}. \tag{2.47}$$

Finally, Eq. (2.40) reduces to, taking $\alpha = 1$:

$$\frac{\delta\mu^2}{\mu^2} \hat{\mathbf{x}}^* \mathscr{R}_\omega^{-1*} \tilde{\mathbf{f}} = \hat{\mathbf{x}}^* \boldsymbol{\delta}\mathbf{J}^* \tilde{\mathbf{f}} + \tilde{\mathbf{f}}^* \boldsymbol{\delta}\mathbf{J}\hat{\mathbf{x}}, \tag{2.48}$$

$$\frac{\delta\mu^2}{\mu^2} \tilde{\mathbf{f}}^* \hat{\mathbf{f}} = 2\mathrm{Real}\left[\tilde{\mathbf{f}}^* \boldsymbol{\delta}\mathbf{J}\hat{\mathbf{x}}\right]. \tag{2.49}$$

An arbitrary variation of the Jacobian $\boldsymbol{\delta}\mathbf{J}$ induces the following variation of the singular value $\delta\mu^2$:

$$\delta\mu^2 = 2\mu^2 \text{Real}\left[\left\langle \tilde{\mathbf{f}}, \boldsymbol{\delta}\mathbf{J}\hat{\mathbf{x}} \right\rangle\right], \tag{2.50}$$

with $\left\langle \tilde{\mathbf{f}}, \hat{\mathbf{f}} \right\rangle = 1$ and thus $\tilde{\mathbf{f}} = \hat{\mathbf{f}}$. In particular, the previous equation is nearly equivalent to Eq. (2.12) with the optimal forcing $\tilde{\mathbf{f}}$ as the adjoint global mode $\tilde{\mathbf{w}}$ and the optimal response $\hat{\mathbf{x}}$ as the direct global mode $\hat{\mathbf{w}}$. Therefore, using the formalism presented in Section 2.2.2 we finally obtain:

$$\delta\mu^2 = 2\mu^2 \text{Real}\left[\left\langle \mathbf{H}'^{*}\tilde{\mathbf{f}}, \boldsymbol{\delta}\mathbf{w_b} \right\rangle\right], \tag{2.51}$$

where the complex matrix $\mathbf{H}'$ is defined such that $\mathbf{H}'\boldsymbol{\delta}\mathbf{w_b} = \mathbf{H}(\hat{\mathbf{x}}, \boldsymbol{\delta}\mathbf{w_b})$ for all $\boldsymbol{\delta}\mathbf{w_b}$. Noting $\mathbf{e}_i$ the unit vector on the i^{th} component of the canonical basis of $\mathbb{R}^N$, we have:

$$\mathbf{H}'_{ik} = \sum_j \mathbf{H}_{ijk}\hat{\mathbf{x}}_j = \langle \mathbf{e_i}, \mathbf{H}(\hat{\mathbf{x}}, \mathbf{e}_k) \rangle . \tag{2.52}$$

The gradient $\boldsymbol{\nabla}_{\mathbf{w_b}}\mu^2$ takes the form:

$$\boldsymbol{\nabla}_{\mathbf{w_b}}\mu^2 = 2\mu^2 \text{Real}\left[\mathbf{H}'^{*}\tilde{\mathbf{f}}\right]. \tag{2.53}$$

Finally, as for the oscillators, we may also consider the impact on the singular value μ^2 of a small amplitude steady source term $\boldsymbol{\delta}\mathbf{f}$ acting on the baseflow. Similarly to Section 2.2.2, we define the sensitivity gradient of the singular value to the introduction of a source term $\boldsymbol{\nabla}_{\mathbf{f}}\mu^2$, which links the singular value variation $\delta\mu^2$ to the steady source term $\boldsymbol{\delta}\mathbf{f}$. In particular we have:

$$\delta\mu^2 = \left\langle \boldsymbol{\nabla}_{\mathbf{f}}\mu^2, \boldsymbol{\delta}\mathbf{f} \right\rangle \quad \text{with} \quad \boldsymbol{\nabla}_{\mathbf{f}}\mu^2 = -\mathbf{J}^{*-1}\boldsymbol{\nabla}_{\mathbf{w_b}}\mu^2. \tag{2.54}$$

The impact of a small amplitude steady source term on the flow singular values can therefore be predicted a priori and control maps can be obtained beforehand.

2.3.3 Kinetic energy maximization

For the sake of clarity, we used in the previous Section the canonical inner product (2.7). However, for the analysis to have a physical relevancy, we shall use the discrete inner product $\langle , \rangle|_{\mathbf{Q}}$ defined in (2.22). Furthermore, the gain μ^2 can also be defined as the maximization of the kinetic energy E of the response $\hat{\mathbf{x}}$ to the forcing $\hat{\mathbf{f}}$. In particular, as the response contains all the conservative variables, we do not have that $\langle \hat{\mathbf{x}}, \hat{\mathbf{x}} \rangle|_Q = E$. We thus define a pseudo scalar product $\langle , \rangle|_{Q_e}$ such that $\langle \hat{\mathbf{x}}, \hat{\mathbf{x}} \rangle|_{Q_e} = \hat{\mathbf{x}}^*\mathbf{Q_e}\hat{\mathbf{x}} = E$. The computation of the matrix $\mathbf{Q_e}$ is detailed in Appendix A.1, where we show in particular

that $\mathbf{Q_e}$ is real, symmetric and semi-definite positive. The maximization problem in Eq. (2.30) thus becomes:

$$\mu^2 = \sup_{\hat{\mathbf{f}}} \frac{\langle \hat{\mathbf{x}}, \hat{\mathbf{x}} \rangle |_{Q_e}}{\left\langle \hat{\mathbf{f}}, \hat{\mathbf{f}} \right\rangle |_{Q}} = \sup_{\hat{\mathbf{f}}} \frac{\hat{\mathbf{f}}^* \mathscr{R}_\omega^* \mathbf{Q_e} \mathscr{R}_\omega \hat{\mathbf{f}}}{\hat{\mathbf{f}}^* \mathbf{Q} \hat{\mathbf{f}}}. \tag{2.55}$$

This is a generalized Rayleigh quotient since $\mathscr{R}_\omega^* \mathbf{Q_e} \mathscr{R}_\omega$ is symmetric semi-definite positive, and the optimal gain corresponds to the largest eigenvalue of the matrix $\mathbf{Q}^{-1} \mathscr{R}_\omega^* \mathbf{Q_e} \mathscr{R}_\omega$. That is:

$$\mathscr{R}_\omega^* \mathbf{Q_e} \mathscr{R}_\omega \hat{\mathbf{f}} = \mu^2 \mathbf{Q} \hat{\mathbf{f}}. \tag{2.56}$$

The equations governing our optimal forcing and response now become:

$$\mathbf{Q_e} \hat{\mathbf{x}} = \mu^2 \mathscr{R}_\omega^{-1*} \mathbf{Q} \hat{\mathbf{f}}, \tag{2.57}$$

$$\hat{\mathbf{f}} = \mathscr{R}_\omega^{-1} \hat{\mathbf{x}}. \tag{2.58}$$

Perturbing this system as in the previous section, Eq. (2.40) is modified into:

$$\left[\tilde{\mathbf{x}}^* \mathbf{Q_e} - \tilde{\mathbf{f}}^* \mathscr{R}_\omega^{-1}\right] \boldsymbol{\delta} \hat{\mathbf{x}} + \left[\tilde{\mathbf{f}}^* - \mu^2 \tilde{\mathbf{x}}^* \mathscr{R}_\omega^{-1*} \mathbf{Q}\right] \boldsymbol{\delta} \hat{\mathbf{f}} = \delta\mu^2 \tilde{\mathbf{x}}^* \mathscr{R}_\omega^{-1*} \mathbf{Q} \hat{\mathbf{f}} - \mu^2 \tilde{\mathbf{x}}^* \boldsymbol{\delta} \mathbf{J}^* \mathbf{Q} \hat{\mathbf{f}} - \tilde{\mathbf{f}}^* \boldsymbol{\delta} \mathbf{J} \hat{\mathbf{x}}. \tag{2.59}$$

We thus impose:

$$\mathbf{Q_e} \tilde{\mathbf{x}} = \mathscr{R}_\omega^{-1*} \tilde{\mathbf{f}}, \tag{2.60}$$

$$\tilde{\mathbf{f}} = \mu^2 \mathbf{Q} \mathscr{R}_\omega^{-1} \tilde{\mathbf{x}}. \tag{2.61}$$

Here, the matrix $\mathbf{Q_e}$ (defined in Appendix A.1) is not invertible so that the solution of this system is not unique. However, the current analysis only requires to find two valid vectors $\tilde{\mathbf{x}}$ and $\tilde{\mathbf{f}}$. The following choices ensure that Eqs. (2.60)&(2.61) are respected:

$$\tilde{\mathbf{x}} = \frac{\alpha}{\mu^2} \hat{\mathbf{x}}. \tag{2.62}$$

$$\tilde{\mathbf{f}} = \alpha \mathbf{Q} \hat{\mathbf{f}}. \tag{2.63}$$

Finally Eq. (2.59) reduces to, imposing $\alpha = 1$:

$$\frac{\delta\mu^2}{\mu^2} \hat{\mathbf{x}}^* \mathscr{R}_\omega^{-1*} \tilde{\mathbf{f}} = \frac{\mu^2}{\mu^2} \hat{\mathbf{x}}^* \boldsymbol{\delta} \mathbf{J}^* \tilde{\mathbf{f}} + \tilde{\mathbf{f}}^* \boldsymbol{\delta} \mathbf{J} \hat{\mathbf{x}}, \tag{2.64}$$

$$\delta\mu^2 = 2\mu^2 \mathrm{Real}\left[\tilde{\mathbf{f}}^* \boldsymbol{\delta} \mathbf{J} \hat{\mathbf{x}}\right], \tag{2.65}$$

$$= 2\mu^2 \mathrm{Real}\left[< \tilde{\mathbf{f}}, \boldsymbol{\delta} \mathbf{J} \hat{\mathbf{x}} >\right], \tag{2.66}$$

$$\hat{\mathbf{f}}^* \tilde{\mathbf{f}} = < \hat{\mathbf{f}}, \hat{\mathbf{f}} >\Big|_{\mathbf{Q}} = 1. \tag{2.67}$$

We recover Eq. (2.50), the gain variation $\delta\mu^2$ does not depend on the inner-product choice. In order to compare to a continuous approach results if available, we introduce the relevant sensitivity gradients and optimal forcing defined using the inner-product $\langle,\rangle|_{\mathbf{Q}}$ instead of the canonical one $\langle,\rangle$:

$$\begin{aligned}
\delta\mu^2 &= < \boldsymbol{\nabla}_{\mathbf{w_b}}\mu^2\big|_{\mathbf{Q}}, \boldsymbol{\delta w_b} >\Big|_{\mathbf{Q}}, && (2.68)\\
&= 2\mu^2 \mathrm{Real}\left[< \mathbf{Q}^{-1}\mathbf{H}'^{*}\tilde{\mathbf{f}}, \boldsymbol{\delta w_b} >\Big|_{\mathbf{Q}}\right], && (2.69)\\
\delta\mu^2 &= < \boldsymbol{\nabla}_{\mathbf{f}}\mu^2\big|_{\mathbf{Q}}, \boldsymbol{\delta f} >\Big|_{\mathbf{Q}}, && (2.70)
\end{aligned}$$

$$\begin{aligned}
\boldsymbol{\nabla}_{\mathbf{w_b}}\mu^2 &= \mathbf{H}'^{*}\tilde{\mathbf{f}}, && (2.71)\\
\boldsymbol{\nabla}_{\mathbf{w_b}}\mu^2\big|_{\mathbf{Q}} &= \mathbf{Q}^{-1}\mathbf{H}'^{*}\tilde{\mathbf{f}}, && (2.72)\\
\boldsymbol{\nabla}_{\mathbf{f}}\mu^2\big|_{\mathbf{Q}} &= -\mathbf{J}^{*-1}\,\boldsymbol{\nabla}_{\mathbf{w_b}}\mu^2\big|_{\mathbf{Q}}, && (2.73)\\
\tilde{\mathbf{f}} &= \mathbf{Q}\hat{\mathbf{f}}, && (2.74)\\
< \hat{\mathbf{f}}, \hat{\mathbf{f}} >\Big|_{\mathbf{Q}} &= 1. && (2.75)
\end{aligned}$$

Remark: The pseudo scalar product that we defined with the matrix $\mathbf{Q_e}$ can be further modified. The energy maximization can also be performed on a restricted domain of our configuration for example, or a different quantity may be seek for the optimization. The previous demonstration still holds provided that the newly defined matrix $\mathbf{Q_e}$ is still symmetric semi-definite positive.

2.3.4 Forcing restrictions

In a practical experiment the forcing may be localized and does not necessarily include all the conservative variables. It may thus be interesting to use a restrained forcing term $\hat{\mathbf{f}}_{\mathbf{s}} \in \mathbb{S}$ that evolves in a subspace $\mathbb{S} \in \mathbb{C}^{\mathrm{M}} \subset \mathbb{C}^{\mathrm{N}}$ with $M < N$ of the flow configuration (we consider spatially localized forcing and/or a forcing that only acts on considered conservative variables). We thus introduce a prolongation matrix $\mathbf{P} \in \mathbb{C}^{\mathrm{N}\times\mathrm{M}}$ such that if $\hat{\mathbf{f}}_{\mathbf{s}} \in \mathbb{S}$ then $\mathbf{P}\hat{\mathbf{f}}_{\mathbf{s}} \in \mathbb{C}^{\mathrm{N}}$, which effect is to add 0 to the restricted term. Similarly we define the restriction matrix $\mathbf{P}^*$ such that if $\hat{\mathbf{f}} \in \mathbb{C}^{\mathrm{N}}$ then $\mathbf{P}^*\hat{\mathbf{f}} \in \mathbb{S}$. Note that by definition of these matrices we have: $\mathbf{P}^*\mathbf{P} = \mathbf{I}$. In particular, the response $\hat{\mathbf{x}}$ now verifies:

$$\hat{\mathbf{x}} = \mathscr{R}_{\omega}\mathbf{P}\hat{\mathbf{f}}_{\mathbf{s}}. \qquad (2.76)$$

The energy maximization (2.55) remains a generalized Rayleigh quotient which solutions are given by:

$$\mathscr{R}_\omega^* \mathbf{Q_e} \mathscr{R}_\omega \mathbf{P} \hat{\mathbf{f}}_\mathbf{s} = \mu^2 \mathbf{Q} \mathbf{P} \hat{\mathbf{f}}_\mathbf{s}. \tag{2.77}$$

The solutions $\hat{\mathbf{f}}_\mathbf{s}$ of this eigenvalue problem are thus seek in the subspace $\mathbb{S}$ and then extended to our configuration with $\hat{\mathbf{f}} = \mathbf{P}\hat{\mathbf{f}}_\mathbf{s}$.

Following the same perturbation and multiplication method as in the previous sections we now have:

$$\left[\tilde{\mathbf{x}}^* \mathbf{Q_e} - \tilde{\mathbf{f}}^* \mathscr{R}_\omega^{-1}\right] \boldsymbol{\delta}\hat{\mathbf{x}} \quad + \quad \left[\tilde{\mathbf{f}}^* \mathbf{P} - \mu^2 \tilde{\mathbf{x}}^* \mathscr{R}_\omega^{-1*} \mathbf{Q} \mathbf{P}\right] \boldsymbol{\delta}\hat{\mathbf{f}}_\mathbf{s} = \tag{2.78}$$

$$\delta\mu^2 \tilde{\mathbf{x}}^* \mathscr{R}_\omega^{-1*} \mathbf{Q} \mathbf{P} \hat{\mathbf{f}}_\mathbf{s} \quad - \quad \mu^2 \tilde{\mathbf{x}}^* \boldsymbol{\delta}\mathbf{J}^* \mathbf{Q} \mathbf{P} \hat{\mathbf{f}}_\mathbf{s} - \tilde{\mathbf{f}}^* \boldsymbol{\delta}\mathbf{J} \hat{\mathbf{x}}. \tag{2.79}$$

Hence we impose:

$$\mathbf{Q_e} \tilde{\mathbf{x}} = \mathscr{R}_\omega^{-1*} \tilde{\mathbf{f}}, \tag{2.80}$$

$$\mathbf{P}^* \tilde{\mathbf{f}} = \mu^2 \mathbf{P}^* \mathbf{Q} \mathscr{R}_\omega^{-1} \tilde{\mathbf{x}}. \tag{2.81}$$

Once again, the solution of the previous set of equations is not unique. In particular, Eq. (2.81) states that we are only interested in the restriction of the solution $\tilde{\mathbf{f}}$ to the space $\mathbb{S}$. As a consequence, we can use the following choices:

$$\tilde{\mathbf{x}} = \frac{\alpha}{\mu^2} \hat{\mathbf{x}}, \tag{2.82}$$

$$\tilde{\mathbf{f}} = \alpha \mathbf{Q} \mathbf{P} \hat{\mathbf{f}}_\mathbf{s}. \tag{2.83}$$

Finally, we obtain using $\alpha = 1$:

$$\delta\mu^2 = 2\mu^2 \mathrm{Real}\left[< \mathbf{Q}^{-1} \mathbf{H}'^* \tilde{\mathbf{f}}, \boldsymbol{\delta}\mathbf{w_b} > \Big|_\mathbf{Q} \right], \tag{2.84}$$

$$= < \boldsymbol{\nabla}_{\mathbf{w_b}} \mu^2 \big|_\mathbf{Q}, \boldsymbol{\delta}\mathbf{w_b} > \Big|_\mathbf{Q}, \tag{2.85}$$

$$\boldsymbol{\nabla}_{\mathbf{w_b}} \mu^2 |_\mathbf{Q} = \mathbf{Q}^{-1} \mathbf{H}'^* \tilde{\mathbf{f}}, \tag{2.86}$$

$$\tilde{\mathbf{f}} = \mathbf{Q} \mathbf{P} \hat{\mathbf{f}}_\mathbf{s}, \tag{2.87}$$

$$< \mathbf{P}\hat{\mathbf{f}}_\mathbf{s}, \mathbf{P}\hat{\mathbf{f}}_\mathbf{s} > \Big|_\mathbf{Q} = 1. \tag{2.88}$$

2.3.5 Method summary

To sump up, in order to compute the sensitivity gradients for noise amplifiers, we need to compute:

1. the discrete Jacobian $\mathbf{J}$ (Eq. (2.5)) and assess its stability;

2. the inverse of the global resolvent ${\mathscr{R}_\omega}^{-1}$ for a given set of frequency ω, its adjoint ${\mathscr{R}_\omega}^{-1*}$, as well as the matrices $\mathbf{Q}$ and $\mathbf{Q_e}$ and the prolongation and restriction operators $\mathbf{P}$ and $\mathbf{P}^*$;

3. the set of optimal gain μ^2, forcing $\hat{\mathbf{f}}$ and response $\hat{\mathbf{x}}$ obtained solving the eigenvalue problem in Eq. (2.77) and then (2.76) ;

4. $\mathbf{H'}^*\tilde{\mathbf{f}}$ (see Eq. (2.52) for the definition of $\mathbf{H'}$) to obtain the sensitivity of the amplification gain to baseflow modifications $\boldsymbol{\nabla}_{\mathbf{w_b}}\mu^2$ (Eq. (2.71));

5. $-\mathbf{J}^{*-1}\boldsymbol{\nabla}_{\mathbf{w_b}}\mu^2$ to obtain the sensitivity of the amplification gain to the introduction of a steady source term $\boldsymbol{\nabla}_{\mathbf{f}}\mu^2$ (Eq. (2.54)).

6. $\boldsymbol{\nabla}_{\mathbf{w_b}}\mu^2\big|_{\mathbf{Q}} = \mathbf{Q}^{-1}\boldsymbol{\nabla}_{\mathbf{w_b}}\mu^2$ and $\boldsymbol{\nabla}_{\mathbf{f}}\mu^2\big|_{\mathbf{Q}} = \mathbf{Q}^{-1}\boldsymbol{\nabla}_{\mathbf{f}}\mu^2$ to obtain sensitivities with a physically relevant inner-product.

2.4 Concluding remarks

A fully discrete formalism was proposed to define the Jacobian matrix and the sensitivity gradients. The proposed framework is discrete as the equations are first discretized and then linearized. In particular, the sensitivity gradients were shown to be linked to the Hessian of the RANS equations. The definitions of the stability problem and the sensitivity gradients were derived for both both oscillators and noise amplifiers dynamics. Several operators were also introduced for the characterization of noise amplifiers. The numerical methods and procedures used to compute these quantities will be detailed in the next Chapter.

Chapter 3

Numerical aspects

We present in this Chapter the different numerical aspects encountered in the computation of the sensitivity gradients. First, a general view point is taken in Section 3.3.4 regarding the numerical strategy that can be adopted to compute the gradients in a discrete framework. In particular, the choice of algorithms to perform matrix inversion and to solve eigenvalue problems, as well as the question of the storage of the matrices are discussed. Second, the computational procedure used to obtain the Jacobian $\mathbf{J}$ and the matrix $\mathbf{H}'$ from residual evaluations are detailed in Section 3.2. A particular set of vectors is introduced to optimize the procedure, and the choice of linearization parameters is discussed. An adaptation of shape optimization code to compute the sensitivity gradients is proposed. Finally, we introduce the RANS equations used in the application cases in Section 3.3, as well as the available choices of numerical schemes.

3.1 Numerical strategy

3.1.1 Explicit storage of matrices with direct inversions

The procedure to compute the sensitivity gradients presented in Chapter 2 relies on the knowledge of the first (the Jacobian $\mathbf{J}$) and second (the Hessian $\mathbf{H}$) derivatives of the discrete operator $\mathcal{R}(\mathbf{w})$. As mentioned in the Introduction, we follow in this study a strategy based on a finite difference method to obtain both $\mathbf{Ju}$ and $\mathbf{H}(\mathbf{u},\mathbf{v})$ with $\mathbf{u}$ and $\mathbf{v}$ arbitrary vectors. More precisely, we want to evaluate these matrices by repeated evaluations of the residual function. The code may then be used in a black box manner: assuming that the code generates a valid discrete residual $\mathcal{R}(\mathbf{u})$, one may

obtain approximations of $\mathbf{Ju}$ and $\mathbf{H}(\mathbf{u},\mathbf{v})$ with the following first order approximations:

$$\mathbf{Ju} = \frac{1}{\epsilon}\left[\mathcal{R}\left(\mathbf{w_b}+\epsilon\mathbf{u}\right)-\mathcal{R}\left(\mathbf{w_b}\right)\right], \tag{3.1}$$

$$\mathbf{H}\left(\mathbf{u},\mathbf{v}\right) = \frac{1}{\epsilon_1\epsilon_2}[\mathcal{R}\left(\mathbf{w_b}+\epsilon_1\mathbf{u}+\epsilon_2\mathbf{v}\right)-\mathcal{R}\left(\mathbf{w_b}+\epsilon_1\mathbf{u}\right) - \mathcal{R}\left(\mathbf{w_b}+\epsilon_2\mathbf{v}\right)+\mathcal{R}\left(\mathbf{w_b}\right)], \tag{3.2}$$

where ϵ, ϵ_1 and ϵ_2 are small constants. The choice of these constants will be further detailed in Section 3.2.4. In the context of global stability analyses, finite difference methods have recently been used to approximate the discrete Jacobian (De Pando et al. [69], Mack and Schmid [89]). Here, we suggest that these methods may also be useful to compute the sensitivity gradients introduced in Chapter 2.

To validate this idea, we have chosen an "explicit matrix" approach combined with a direct sparse LU solver to perform matrix inversions, which is relevant for small-scale-problems of the order of $10^6 - 10^7$ degrees of freedom for $\mathbf{w}$. The advantage of this strategy is that it yields fast and accurate results. The "explicit matrix" strategy consists in computing and storing all non-zero values of the various matrices involved in Chapter 2. Due to the large size of the meshes this is possible only if these matrices are sparse. The Jacobian structure is intrinsically linked to the stencil width used to discretize $\mathcal{R}$, which we assume to be compact, ensuring the sparse nature of $\mathbf{J}$. Moreover, a similar result holds for matrix $\mathbf{H}'$ (see next section for details). Explicit knowledge of these matrices induces that we also have direct access to $\mathbf{J}^*$ and $\mathbf{H}'^*$ involved in steps 2, 3 and 4 of the procedure summarized at the end of Section 2.2.3, as well as in steps 2, 4, and 5 of the method in Section 2.3.5. The eigenvalue problems in Eqs. (2.5) and (2.10) for oscillators may be solved using Krylov methods with a shift-invert strategy (open source library ARPACK [90]), so as to focus on the least-damped eigenvalues. For noise amplifiers, the eigenvalue problem in Eq. (2.77) can be solved using the power method algorithm of Lanczos. Matrix inversions involved are carried out in the following with a direct sparse LU solver for distributed memory machines (MUMPS see http://graal.ens-lyon.fr/MUMPS/, or SuperLU-dist see http://acts.nersc.gov/superlu/). The inverses are obtained extremely fast but the drawback is the very high requirements in terms of memory (typically around 50 times the memory of the matrix to be inverted). In order to avoid this overshoot in memory, one could use, instead of the direct LU solvers, iterative algorithms such as BICGSTAB with an incomplete LU preconditioner (Mack and Schmid [89]). This would however result in a strong increase in computational time.

3.1.2 On-the-fly computation

For problems with a larger number of degrees of freedom, typically 3D problems, one has to resort to "on the fly" approaches, where the matrix is never stored explicitly. The "on the fly" strategy has been introduced in the context of global stability analyses by Mamun et al. [91], Bagheri et al. [92] and Mack et al. [89]. The objective here is to avoid forming any matrix explicitly in order to save memory. This requires specific algorithms that are solely based on the action of the matrices on a vector. De Pando et al. [69] have shown in the context of laminar compressible flows how to efficiently compute $\mathbf{Ju}$ and $\mathbf{J}^*\mathbf{u}$ by using finite differences with an existing direct numerical simulation code. Also, they showed that time-integration of Eq. (2.3) combined with a Krylov-Schur method and a harmonic extraction technique effectively recovered the least-damped direct and adjoint global modes. From the similarity between oscillators and noise amplifiers, such technique can also be applied to Eq. (2.29) to compute the optimal gain with the corresponding optimal forcing and response. However, these previous studies using "on the fly" strategies were not concerned with the computation of the sensitivity gradients. In the following lines, the formalism introduced for the oscillators is used. We shall remark here that during the computation of the sensitivity to baseflow modifications, the evaluation of $\mathbf{z} = \mathbf{H}'^*\tilde{\mathbf{w}}$ can in principle also be performed "on the fly":

$$\mathbf{z}_i = \sum_j \overline{\mathbf{H}'_{ji}}\tilde{\mathbf{w}}_j = \sum_j \overline{\langle \mathbf{e}_j, \mathbf{H}(\hat{\mathbf{w}}, \mathbf{e}_i)\rangle}\tilde{\mathbf{w}}_j \tag{3.3}$$

$$= \overline{\langle \tilde{\mathbf{w}}, \mathbf{H}(\hat{\mathbf{w}}, \mathbf{e}_i)\rangle}. \tag{3.4}$$

where $\mathbf{H}(\hat{\mathbf{w}}, \mathbf{e}_i)$ can be approximated from Eq. (3.2). This evaluation may be computationally intensive since one Hessian evaluation $\mathbf{H}(\hat{\mathbf{w}}, \mathbf{e}_i)$ has to be performed by degree of freedom so that some optimization may be useful. Nevertheless, since this evaluation is only done once per considered eigenmode, it is less critical than the evaluations of $\mathbf{Ju}$ and $\mathbf{J}^*\mathbf{u}$, required for the time-integration in the eigenvalue problems. The same remark is true in the case of noise amplifiers, as we need to evaluate $\mathbf{z} = \mathbf{H}'^*\tilde{\mathbf{f}}$. Finally, the required inversion $\mathbf{Q}^{-1}\mathbf{u}$ may easily be carried out with a cheap conjugate gradient algorithm with diagonal preconditioning.

3.2 Efficient evaluation of matrices with explicit storage

This section describes the procedure used to efficiently compute the matrices $\mathbf{J}$ and $\mathbf{H}'$ by taking advantage of their structure dependence to the discretization stencil. The choice of the linearization parameters is then discussed. A more intrusive approach suited

for codes containing an existing linearization of the RANS equations such as shape optimization codes will finally be investigated. We consider in the following a case of dimension d solved using finite volume or finite difference methods with a discretization scheme using an n_s points stencil in each direction. We assume the governing equations (2.1) to be discretized on a mesh of size $N_m = I_m \times J_m \times K_m$ for a system of n_c conservative variables. As will be further detailed, the Jacobian is a square matrix of size $N \times N$ where $N = n_c \times N_m$, with a total number of non zero elements n_e.

3.2.1 Example case

As an example case, we consider the following $d = 1$ dimensional model with $n_c = 2$ conservative variables discretized on an $n_s = 2$ points stencil, the discretization step Δx is taken uniform and equal to 1 for simplicity :

$$\mathcal{R}(\mathbf{w}) = \mathcal{R}\begin{pmatrix}\mathbf{a}\\ \mathbf{b}\end{pmatrix} = \begin{pmatrix}\mathbf{b}\partial_x\mathbf{a}\\ \mathbf{a}\partial_x\mathbf{b}\end{pmatrix} \qquad \mathcal{R}_{\mathrm{i}} = \begin{pmatrix}b_i\left[a_{i+1}-a_i\right]\\ a_i\left[b_{i+1}-b_i\right]\end{pmatrix}. \tag{3.5}$$

Linearizing the discrete equations, we obtain the product $\mathbf{Ju}$ in the stencil $(i, i+1, i+2)$:

$$\underbrace{\begin{pmatrix} -b_i & a_{i+1}-a_i & b_i & 0 & 0 & 0\\ b_{i+1}-b_i & -a_i & 0 & a_i & 0 & 0\\ 0 & 0 & -b_{i+1} & a_{i+2}-a_{i+1} & b_{i+1} & 0\\ 0 & 0 & b_{i+2}-b_{i+1} & -a_{i+1} & 0 & a_{i+1}\end{pmatrix}}_{\mathbf{J}} \underbrace{\begin{pmatrix} da_i\\ db_i\\ da_{i+1}\\ db_{i+1}\\ da_{i+2}\\ db_{i+2}\end{pmatrix}}_{\mathbf{u}} \tag{3.6}$$

We foresee that all the Jacobian coefficients can be obtained independently from this matrix vector product using the following set of vectors $\mathbf{u}$:

$$\mathbf{u} = \begin{pmatrix} \vdots \\ da_{i-1} \\ db_{i-1} \\ da_i \\ db_i \\ da_{i+1} \\ db_{i+1} \\ da_{i+2} \\ db_{i+2} \\ \vdots \end{pmatrix} = \underbrace{\begin{pmatrix} \vdots \\ 0 \\ 0 \\ 1 \\ 0 \\ 0 \\ 0 \\ 1 \\ 0 \\ \vdots \end{pmatrix} = \begin{pmatrix} \vdots \\ 1 \\ 0 \\ 0 \\ 0 \\ 1 \\ 0 \\ 0 \\ 0 \\ \vdots \end{pmatrix}}_{\text{da}} = \underbrace{\begin{pmatrix} \vdots \\ 0 \\ 0 \\ 0 \\ 1 \\ 0 \\ 0 \\ 0 \\ 1 \\ \vdots \end{pmatrix} = \begin{pmatrix} \vdots \\ 0 \\ 1 \\ 0 \\ 0 \\ 0 \\ 1 \\ 0 \\ 0 \\ \vdots \end{pmatrix}}_{\text{db}} \tag{3.7}$$

This set corresponds to perturbation vectors $\mathbf{e_i}$ taken every $n_s = 2$ points for each variable **a** and **b** separately. The non zero indices in the perturbation vectors are shifted every $n_c \times n_s = 4$ points to ensure that we only compute one contributing term (da_i, da_{i+1}, db_i or db_{i+1} for example) for each matrix vector product. The Jacobian can thus be obtained using $n_s \times n_c = 4$ residual evaluations. Each line of the Jacobian contains $n_c \times n_s$ non zero coefficients, we thus have $n_e \approx n_c \times n_s \times N = 8N_m$.

3.2.2 Jacobian computation

The Jacobian is computed according to Eq. (3.1) by evaluation of the discrete residuals at each point. Using an n_s points stencil, the discrete residual at point (i, j, k) for the v^{th} variable $\mathcal{R}^{\text{v}}_{\text{ijk}} = \mathcal{R}\left(\mathbf{W}_{\text{lmn}}\right)$ is only a function of the (l,m,n) points linked to (i, j, k) by the discretization stencil, that is at most n_s^d points ($d = 1,2,3$ if we consider respectively a one, two or three dimensional case). As an example, a two dimensional case with $n_s = 5$ is depicted in Fig. 3.1 where the dependency of the residual $\mathcal{R}^{\text{v}}_{\text{ij}}$ towards the stencil is plotted. We foresee from this example that the total number of points n_p which contribute to the residual evaluation at one point may differ from the maximum value n_s^d, that is $n_p \leq n_s^d$ (in the Figure $n_p = 13$ while $n_s^2 = 25$).

The Jacobian coefficients can be interpreted as the contribution of the (l, m, n) point to the linearization around the baseflow of the discretized equations at the point (i, j, k). Linearizing the equations at (i, j, k) for a given variable, we obtain n_c coefficients for each of the n_p contributing points (l, m, n). Therefore the total number of non zero elements in the Jacobian scales as $n_e \approx n_p n_c N = n_p n_c^2 N_m$. Note that n_e corresponds to the maximum number of non zero elements in the matrix and may overpredict the

actual number. The sparsity coefficient of the matrix $S = 1 - n_e/N^2 \approx 1 - n_p/N_m$ is reduced when the stencil width of the system is increased.

Perturbing the baseflow with a vector $\mathbf{e_{lmn}}$ equal to 1 for a given conservative variable at a point (l, m, n) and 0 elsewhere, Eq. (3.1) becomes:

$$\mathbf{J e_{lmn}} = \frac{1}{\epsilon} \left[\mathcal{R} \left(\mathbf{w_b} + \epsilon \mathbf{e_{lmn}} \right) - \mathcal{R} \left(\mathbf{w_b} \right) \right]. \tag{3.8}$$

Due to the stencil dependency, the perturbation only impacts the discrete residuals at the n_p points around (l, m, n) in their evaluation. Therefore, the right hand side of the previous equation yields $n_p n_c$ non zero coefficients of $\mathbf{J}$. These terms correspond to the contribution of (l, m, n) to the linearization of the equations at these n_p points. Therefore the complete linearization of the discrete equations at a point (i, j, k) can be obtained by perturbing individually all the n_p points that intervene in the residual evaluation at (i, j, k) for each conservative variable. The Jacobian coefficients can thus be obtained independently using Eq. (3.8) by defining a set of perturbation vectors $(\mathbf{e_p})$ for each conservative variable and every n_s points in each direction. The matrix is obtained by performing $n_{res} = n_c n_s^d$ residual evaluations (or matrix vector products) and then assembling it explicitly. We shall note here that the residual evaluations for each perturbation vector $\mathbf{e_p}$ are independent from one to another: the computational time of this procedure can be greatly lowered using parallel computation.

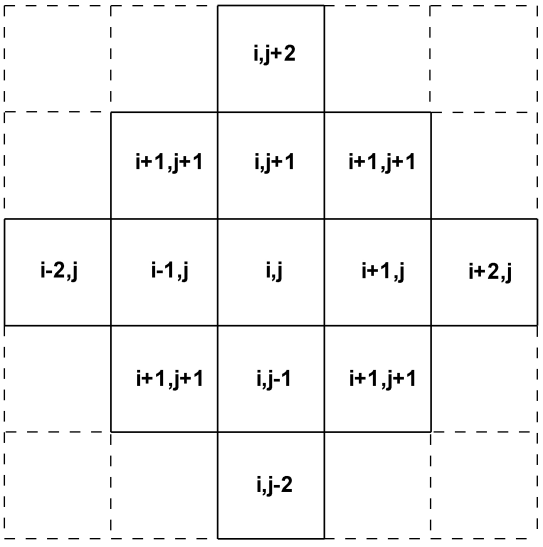

FIGURE 3.1: Example of stencil dependency of the residual evaluated at the point (i, j).

3.2.3 Hessian computation

As detailed in Chapter 2, the computation of the sensitivity gradients mainly requires the computation of the matrix $\mathbf{H}'$. As the structure of $\mathbf{H}'$ depends on the discretization stencil similarly to that of $\mathbf{J}$, a similar perturbation method may be used to compute it. Due to the analogy between the computation of $\mathbf{H}'$ for noise amplifiers and oscillators, we will here use the formalism dedicated to oscillators. Note that the results can be straightforwardly extended to noise amplifiers by changing the roles of the adjoint mode $\tilde{\mathbf{w}}$ with the optimal forcing $\tilde{\mathbf{f}}$, and of the unstable mode $\hat{\mathbf{w}}$ with the optimal response $\hat{\mathbf{x}}$. In particular, using Eq. (2.16) we have:

$$\begin{aligned}\mathbf{H}'\mathbf{e_p} &= \mathbf{H}\left(\hat{\mathbf{w}},\mathbf{e_p}\right) \\ &= \frac{1}{\epsilon_1\epsilon_2}[\mathcal{R}\left(\mathbf{w_b}+\epsilon_1\hat{\mathbf{w}}+\epsilon_2\mathbf{e_p}\right)-\mathcal{R}\left(\mathbf{w_b}+\epsilon_1\hat{\mathbf{w}}\right) \\ &\qquad -\mathcal{R}\left(\mathbf{w_b}+\epsilon_2\mathbf{e_p}\right)+\mathcal{R}\left(\mathbf{w_b}\right)],\end{aligned} \tag{3.9}$$

where $(\mathbf{e_p})$ corresponds to the set of perturbation vectors previously defined. The size of $\mathbf{H}'$ and its number of non zero elements are thus equal to the Jacobian ones. The computational cost of explicitly forming $\mathbf{H}'$ is four times the Jacobian one as two complex residual evaluations have to be performed for each $\mathbf{e_p}$ in Eq. (3.9). In a code where only real structures are available, all the above mentioned evaluations shall be done separately for both real and imaginary parts of the eigenmode $\hat{\mathbf{w}}$. Indeed, as $\boldsymbol{\delta}\mathbf{J}$ and $\boldsymbol{\delta}\mathbf{w_b}$ are real quantities in Eq. (2.17), both real and imaginary parts of Eq. (2.17) can be computed separately.

We previously introduced first order linearization formulas for explanation purpose. In practice, second order formulas are used for the computation of both $\mathbf{J}$ and $\mathbf{H}'$:

$$\mathbf{J}\mathbf{e_p} = \frac{1}{2\epsilon}\left[\mathcal{R}\left(\mathbf{w_b}+\epsilon\mathbf{e_p}\right)-\mathcal{R}\left(\mathbf{w_b}-\epsilon\mathbf{e_p}\right)\right], \tag{3.10}$$

$$\begin{aligned}\mathbf{H}'\mathbf{e_p} &= \frac{1}{4\epsilon_1\epsilon_2}[\mathcal{R}\left(\mathbf{w_b}+\epsilon_1\hat{\mathbf{w}}+\epsilon_2\mathbf{e_p}\right)-\mathcal{R}\left(\mathbf{w_b}+\epsilon_1\hat{\mathbf{w}}-\epsilon_2\mathbf{e_p}\right) \\ &\qquad -\mathcal{R}\left(\mathbf{w_b}-\epsilon_1\hat{\mathbf{w}}+\epsilon_2\mathbf{e_p}\right)+\mathcal{R}\left(\mathbf{w_b}-\epsilon_1\hat{\mathbf{w}}-\epsilon_2\mathbf{e_p}\right)].\end{aligned} \tag{3.11}$$

For both matrix computations, the second order precision procedure is twice more costly than the first order one as twice more residual evaluations have to be performed for each $\mathbf{e_p}$.

3.2.4 Adequate choice of linearization parameters

The linearization parameters ϵ,ϵ_1,ϵ_2 in Eqs. (3.8-3.12) should not be too small to avoid round-off errors and not too large for the approximations to remain accurate. This issue and optimal choices of ϵ have been discussed in detail by Knoll et al. [93] in the context of Jacobian free methods.

Here, we compute each coefficient of the Jacobian individually, so that we actually linearize a scalar equation. The linearizaton parameter can thus be taken as mentioned in [93] : $\epsilon = \epsilon_m (|w| + 1)$, with w the local baseflow value of the considered variable. Noting M_p the machine precision (64 bit machines), An et al. [94] showed that the ϵ_m which minimized the error should be taken equal to $\epsilon_m = \sqrt{M_p} \approx 10^{-8}$ for the first order approximation, and equal to $\epsilon_m = \sqrt[3]{M_p/2} \approx 5.10^{-6}$ for second order ones. Note that when performing second order precision computations, as some conservative variables should remain positive by definition, the imposed perturbation must remain smaller than the baseflow local value. When the previous choice of ϵ does not satisfy this criterion, we imposed ϵ to be 10 times smaller than the local baseflow value $|w|$.

For the computation of $\mathbf{H'}$ which is a second order derivative, ϵ_1 is taken (similarly to Jacobian free methods [89]) such that the unstable mode $\epsilon_1 \hat{\mathbf{w}}$ can be considered as small compared to the baseflow $\epsilon_1 \|\hat{\mathbf{w}}\| = \sqrt{M_p} \|\mathbf{w_b}\|$. This choice of global ϵ_1 ensures that the matrix can be computed in $n_c n_s^d$ residual evaluations. In the case of a local ϵ_1 (where the value of ϵ_1 may differ from one point to another), each local contribution $\mathbf{H_{ijk}}\hat{\mathbf{w}}_\mathbf{j}$ in Eq. (2.16) should be computed independently. This can be done by defining a set of vectors ($\mathbf{e_p}'$) with the same structure as the previously defined set ($\mathbf{e_p}$) but with local non zero values e_{p_j} equal to $\epsilon_1 \hat{w_j}$. For each perturbation vector $\mathbf{e_p}$, the residual evaluation in Eqs. (3.9) and (3.12) should be done for all the $\mathbf{e_p}'$ and then summed as in Eq. (2.16) to obtain the column of $\mathbf{H'}$ given by the considered $\mathbf{e_p}$.The total cost of the method would thus raise to $n_{res} = \left(n_c n_s^d\right)^2$ residual evaluations.

Finally, we also imposed ϵ_2 to be of the form $\epsilon_2 = \epsilon_{m_2} (|w| + 1)$, forthcoming results will show that the choice of ϵ_{m_2} appeared to be more complex as the gradients are more sensitive to this choice. In particular, several values of local ϵ_{m_2} adapted to each flow variable were tested to obtain the best linearization set.

3.2.5 Adaptation of optimization codes

Optimal design methods require the evaluation of aerodynamic quantities with respect to some parametrization of the flow (Sobieszczanski-Sobieski [95]). The solution is obtained using a gradient based optimization process which requires the computation of

the product $\mathbf{Ja}$ where $\mathbf{a}$ is a specific vector field. Note that we consider here a discrete framework where the equations to linearize are the discrete ones. Usually, $\mathbf{J}$ is obtained using an analytical linearization rather than a discrete linearization for precision purpose, as the optimization process is very sensitive to the precision of the Jacobian and its adjoint (Peter and Dwight [72]). However, due to the complexity of the equations to linearize, several simplifications may be done in the linearization process. For example, the thin layer assumption (Candler and MacCormack [96]) may be used so that cross derivatives of the stress tensors in the RANS equations are neglected.

Despite the simplifications achieved in the linearization, such optimization codes can be used to compute the sensitivity gradients. Indeed, the code can be intrusively modified in order to yield a product $\mathbf{Ju}$ for any vector $\mathbf{u}$. Using the same set of vector ($\mathbf{e_p}$) as before, we can obtain all the Jacobian terms by matrix vector evaluations.

The matrix $\mathbf{H'}$ can then be obtained using finite differences applied directly to the Jacobian. Indeed we have from Eq. (2.17):

$$\frac{\mathbf{J}_{\mathbf{w_b}+\epsilon_2\mathbf{e_p}}\hat{\mathbf{w}} - \mathbf{J}_{\mathbf{w_b}}\hat{\mathbf{w}}}{\epsilon_2} = \mathbf{H'e_p}. \tag{3.12}$$

For each vector $\mathbf{e_p}$, the Jacobian associated to the perturbed baseflow $\mathbf{w_b} + \epsilon_2\mathbf{e_p}$ is obtained using the above mentioned Jacobian computation. Subtracting it with the unperturbed baseflow Jacobian and multiplying by the global mode $\hat{\mathbf{w}}$ we obtain $\mathbf{H'e_p}$ so that $\mathbf{H'}$ can be formed explicitly using Eq. (3.12). We shall note that if no approximations are done in the analytical linearization, such a procedure would be more precise then our fully discrete approach since only a first order derivative would be approximated using finite differences.

3.3 RANS equations and turbulence models

3.3.1 Mean field variables

The Navier-Stokes equations in (2.1) can be rewritten as:

$$\frac{d}{dt}\begin{pmatrix}\mathbf{w}^{\mathrm{mf}}\\ \mathbf{w}^{\mathrm{tf}}\end{pmatrix} = \begin{pmatrix}\mathcal{R}^{\mathrm{c,mf}} + \mathcal{R}^{\mathrm{d,mf}}\\ \mathcal{R}^{\mathrm{c,tf}} + \mathcal{R}^{\mathrm{d,tf}} + \mathcal{T}\end{pmatrix} \tag{3.13}$$

where the superscripts mf and tf refer respectively to the mean and turbulent fields of the RANS equations. In particular, $\mathbf{w}^{\mathrm{mf}} = (\rho, \rho\mathbf{U}, \rho E)^T$ where ρ designates the density , $\mathbf{U}$ the velocity and E the total energy of the flow. Terms $\mathcal{R}^{\mathrm{c}}$, $\mathcal{R}^{\mathrm{d}}$ and $\mathcal{T}$ correspond respectively to the convective and diffusive fluxes of the equations and the turbulence

source term. The continuous form of the mean field fluxes in Eq. (3.13) are given by:

$$\mathcal{R}^{\mathrm{c,mf}} = -\begin{pmatrix} \rho\mathbf{U} \\ \rho\mathbf{U}\otimes\mathbf{U} + p\mathbf{I} \\ \rho E\mathbf{U} + p\mathbf{U} \end{pmatrix} \qquad \mathcal{R}^{\mathrm{d,mf}} = \begin{pmatrix} 0 \\ \boldsymbol{\tau} + \boldsymbol{\tau_r} \\ \boldsymbol{\tau}\mathbf{U} + \boldsymbol{\tau_r}\mathbf{U} - \mathbf{q} - \mathbf{q_t} \end{pmatrix}, \tag{3.14}$$

with

$$p = \rho RT \quad \boldsymbol{\tau} = -\frac{2}{3}\mu\left(\nabla\cdot\mathbf{U}\right)\mathbf{I} + 2\mu\mathbf{D} \quad \mathbf{q} = -\frac{c_p\mu}{Pr}\nabla T, \tag{3.15}$$

$$\boldsymbol{\tau_r} = -\frac{2}{3}\mu_t\left(\nabla\cdot\mathbf{U}\right)\mathbf{I} + 2\mu_t\mathbf{D} \quad \mathbf{q_t} = -\frac{c_p\mu_t}{Pr_t}\nabla T, \tag{3.16}$$

p is the pressure, R the perfect gas constant, c_p the heat capacity at constant pressure, μ the viscosity, T the temperature, $\boldsymbol{\tau}$ the viscous tensor, $\mathbf{q}$ the heat flux, $\mathbf{D}$ and $\mathbf{I}$ the strain and identity tensors respectively, μ_t the eddy viscosity (computed with the chosen turbulence model), $\boldsymbol{\tau_r}$ the Reynolds stress tensor, $\mathbf{q_t}$ the flux of diffusion of turbulent enthalpy, Pr and Pr_t the classical and turbulent Prandtl number assumed constants and taken respectively equal to 0.72 and 0.9. The preceding equations were derived using Boussinesq hypothesis and perfect gaz relations. The viscosity is computed using Sutherland's law:

$$\mu = \mu_s\sqrt{\frac{T}{T_s}}\frac{1 + C_s/T_s}{1 + C_s/T}, \tag{3.17}$$

using the constants $\mu_s = 1.71\ 10^{-5}$Pa.s,$C_s = 110.4$ and $T_s = 273$K. The variables $\mathbf{U}, E, k, \omega$ are mass weighted averaged using Favre average whereas the other ones are averaged according to the classical RANS average in time.

For turbulent flows, we chose to use two widely encountered turbulence models, the $k-\omega$ model of Wilcox and the Spalart-Allmaras model. In particular, the turbulent kinetic energy term k in the energy conservative equation is neglected as suggested by dimensional analysis for high Reynolds number flows.

3.3.2 $k-\omega$ model of Wilcox

The $k-\omega$ model of Wilcox [51] introduces the turbulent conservative variables $\mathbf{w}^{\mathrm{tf}} = (\rho k,\, \rho\omega)^T$, where k is the turbulent kinetic energy and ω the rate of dissipation of turbulence. The turbulent fluxes and source terms are then given by:

$$\mathcal{R}^{\mathbf{c,tf}} = -\begin{pmatrix} \rho k\mathbf{U} \\ \rho\omega\mathbf{U} \end{pmatrix}, \qquad \mathcal{R}^{\mathbf{d,tf}} = \begin{pmatrix} \left(\mu + \sigma^*\mu_t\right)\nabla k \\ \left(\mu + \sigma\mu_t\right)\nabla\omega \end{pmatrix}, \tag{3.18}$$

β^*	β	σ^*	σ	γ	K
0.09	0.075	0.5	0.5	$\frac{\beta}{\beta^*} - \frac{\sigma K^2}{\sqrt{\beta^*}}$	0.41

TABLE 3.1: Constants used in the $k-\omega$ model of Wilcox.

$$\mathcal{T} = \begin{pmatrix} \boldsymbol{\tau_r} : \boldsymbol{\nabla}\mathbf{U} - \beta^* \rho k \omega \\ \frac{\gamma}{\nu_t} \boldsymbol{\tau_r} : \boldsymbol{\nabla}\mathbf{U} - \beta \rho \omega^2 \end{pmatrix}, \tag{3.19}$$

where the constants used are summarized in Table 3.1.

The turbulent eddy viscosity is finally defined with:

$$\mu_t = \frac{\rho k}{\omega}. \tag{3.20}$$

3.3.3 Spalart-Allmaras model

The turbulence model of Spalart and Allmaras [65] is a one equation turbulence model which introduces the kinematic viscosity transform $\tilde{\nu}$ with $\mathbf{w}^{\mathrm{tf}} = (\rho\tilde{\nu})$. The turbulent fluxes and source terms are then given by :

$$\mathcal{R}^{\mathbf{c,tf}} = -\left(\rho\tilde{\nu}\mathbf{U}\right) \qquad \mathcal{R}^{\mathbf{d,tf}} = \left(\frac{\mu + \rho\tilde{\nu}}{\sigma_{\tilde{\nu}}} \nabla\tilde{\nu}\right), \tag{3.21}$$

$$\mathcal{T} = \Big(Prod + Cross + Dest + Trans\Big). \tag{3.22}$$

The source terms can be identified as:

- a production term $Prod = C_{b1}\tilde{S}\rho\tilde{\nu}$,
- a cross diffusion term $Diff = \frac{C_{b2}}{\sigma}\nabla\rho\tilde{\nu}\cdot\nabla\tilde{\nu}$,
- a destruction term $Dest = -C_{w1} f_w \rho \frac{\tilde{\nu}^2}{\eta^2}$,
- a transition term $Trans = f_{t2}\left(\frac{C_{b1}}{K^2}\rho\frac{\tilde{\nu}^2}{\eta^2} - C_{b1}\tilde{S}\rho\tilde{\nu}\right)$,

with, noting Ω the vorticity :

$$\begin{array}{lllllllll} \tilde{S} & = & |\Omega| + \frac{\tilde{\nu}}{K^2\eta^2} f_{v2}, & & f_{v2} & = & 1 - \frac{\chi}{1+\chi f_{v1}}, & & f_w & = & g\left(\frac{1+C_{w3}^6}{g^6+C_{w3}^6}\right)^{1/6}, \\ g & = & r + C_{w2}\left(r^6 - r\right), & & f_{t2} & = & C_{t3} e^{-C_{t4}\chi^2}, & & r & = & \frac{\tilde{\nu}}{\tilde{S}K^2\eta^2}. \end{array}$$

C_{b1}	C_{b2}	σ	K	C_{w1}	C_{w2}	C_{w3}	C_{v1}	C_{t3}	C_{t4}	f_{t2}
0.1355	0.622	2/3	0.41	$C_{b1}/K^2 + (1 + C_{b2})/\sigma$	0.3	2	7.1	1.2	0.5	0

TABLE 3.2: Constants used in the Spalart-Allmaras model.

The turbulent eddy viscosity is finally defined with:

$$\mu_t = \rho\tilde{\nu} f_{v1}, \tag{3.23}$$

with :

$$f_{v1} = \frac{\chi^3}{\chi^3 + C_{v1}^3}, \qquad \chi = \frac{\rho\tilde{\nu}}{\mu}. \tag{3.24}$$

The values of the constants for the Spalart-Allmaras model are given in Table 3.2. As we are not interested in the transition to turbulence induced by the turbulence model, we set in this study the transition terms to 0 in the following. The model is designed such that the turbulent variable $\rho\tilde{\nu}$ tends towards the eddy viscosity μ_t far from the walls.

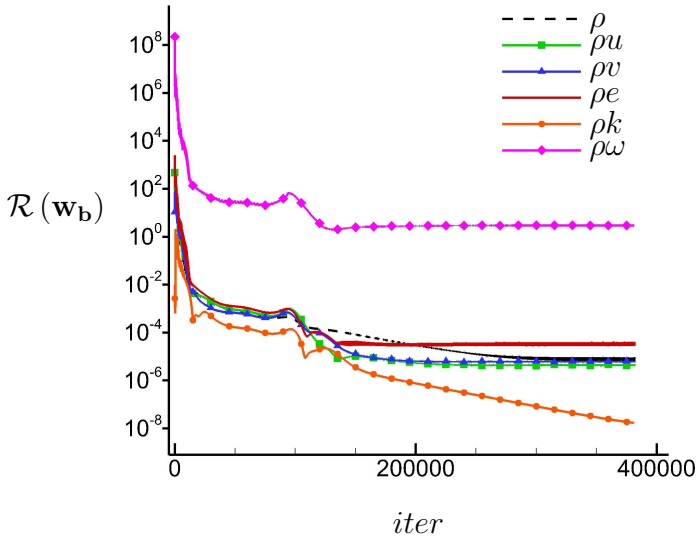

FIGURE 3.2: Typical evolution of the explicit residuals during a baseflow computation using the $k - \omega$ model of Wilcox.

3.3.4 Numerical schemes

We use the finite volume code elsA developed at ONERA (Cambier et al. [97, 98]) to solve the steady RANS and unsteady uRANS equations. The system defined in Eq. (3.13) is solved for each cell (i, j) of volume Ω and surface Σ in its integral formulation :

$$\frac{d}{dt}\mathbf{W_{ij}} = \mathcal{R}_{\mathbf{ij}}^{\mathbf{c}} - \mathcal{R}_{\mathbf{ij}}^{\mathbf{d}} + \mathcal{T}_{\mathbf{ij}} = \mathcal{R}_{\mathbf{ij}}, \tag{3.25}$$

with :

$$\mathbf{W_{ij}} = \frac{1}{\Omega}\int_{\Omega} \mathbf{W} \mathrm{d}\Omega, \qquad \mathcal{T}_{\mathbf{ij}} = \frac{1}{\Omega}\int_{\Omega} \mathcal{T} \mathrm{d}\Omega, \tag{3.26}$$

$$\mathcal{R}^{\mathbf{c,d}}_{\mathbf{ij}} = \frac{1}{\Sigma}\oint_{\Sigma} \mathcal{R}^{\mathbf{c,d}} \cdot \mathbf{n} \mathrm{d}\Sigma = \frac{1}{\Omega}\left(\mathcal{R}^{\mathbf{c,d}}_{\mathbf{i+1/2,j}} + \mathcal{R}^{\mathbf{c,d}}_{\mathbf{i,j+1/2}} + \mathcal{R}^{\mathbf{c,d}}_{\mathbf{i\text{-}1/2,j}} + \mathcal{R}^{\mathbf{c,d}}_{\mathbf{i,j\text{-}1/2}}\right). \tag{3.27}$$

In particular, $\mathcal{R}_{\mathbf{ij}}$ corresponds to the discrete residual operator. In order to check the robustness of the method, several spatial discretization schemes of the mean field convective flux $\mathcal{R}^{\mathbf{c,mf}}_{\mathbf{ij}}$ can be used both for baseflow and Jacobian computations: a central difference formula with Jameson's scalar dissipation and Martinelli's correction (Martinelli [99]), a Roe scheme extended to the second order using MUSCL method (Van Leer [100]) and an AUSM scheme (Mary et al. [101]). The convective flux associated with the turbulence equations $\mathcal{R}^{\mathbf{c,tf}}_{\mathbf{ij}}$ are discretized using the first order Roe scheme with Harten's correction to prevent the occurrence of low eigenvalues (Harten and Hyman [102]). A central difference scheme is used for the turbulent diffusive flux. The viscous flux of the mean field is calculated at the interface by averaging cell-centered values of flux density which is computed from cell-centered evaluation of gradients. The source terms are discretized using estimates of gradients and variables at cell centers. The Zheng limiter operator (Zheng et al. [103] designed to limit the values of $\rho\omega$) is used for the baseflow computation with the $k-\omega$ model, but is switched off for the stability analysis. These discretization choices all lead to an $n_s = 5$ points stencil, an example of the dependency of the residual evaluated at the cell (i, j) being depicted in Fig.3.1. As mentioned in Section 3.2.2, the total number of points $n_p = 13$ contributing to the residual evaluation at one point does not scale with $n_s^2 = 25$ (in a three dimensional case we would have $n_p = 34$ rather than $n_s^3 = 125$). Boundary conditions are imposed by computing the residuals at the interfaces defined by the boundaries. The characteristic equations are integrated to obtain boundary values in the case of inlet or outlet conditions. Turbulent quantities at walls are computed as proposed by Wilcox [51] and Spalart and Allmaras [53]. Note that all these discretization choices combined with turbulence model yield to second order differentiable discrete equations as required for the sensitivity gradients to be defined. Steady state solutions are obtained using a backward-Euler scheme with local time-stepping. Unsteady solutions are computed using the second order implicit Gear scheme. Convergence of the baseflow is assessed by ensuring that the explicit residuals of the mean field equations are small (typically 10^{-11}) and that the residual of the turbulent equations have decreased by several orders of magnitude. A typical evolution of the residuals is given in Fig.3.2 for the deep cavity case described in Chapter 5.

3.3.5 Treatment of boundary conditions

Two types of boundaries can be distinguished: material surfaces, such as adiabatic walls, and permeable boundaries which are introduced to artificially limit the computational domain. In elsA, the boundary conditions are imposed directly in the fluxes evaluation at the boundary in Eq. (3.13). For material surfaces, the boundary condition dictates the values of several conservative variables at the interface defined by the boundary, the missing variables being extrapolated from the computational domain.

For permeable boundaries, the characteristic equations are used in order to compute the conservative variables at the boundary from the computational domain. A particular treatment is performed on permeable boundaries, where the discrete residual $\mathcal{R}\left(\mathbf{W_b} + \boldsymbol{\delta}\mathbf{W_b}\right)$ is evaluated using a pseudo integration in time:

$$\mathcal{R}\left(\mathbf{W_b} + \boldsymbol{\delta}\mathbf{W_b}\right) = \frac{\left(\mathbf{W_b} + \boldsymbol{\delta}\mathbf{W_b}\right)^{n+1} - \left(\mathbf{W_b} + \boldsymbol{\delta}\mathbf{W_b}\right)}{\Delta t}. \tag{3.28}$$

This procedure ensures that unsteady boundary conditions are used in the evaluation of $\mathcal{R}\left(\mathbf{W_b} + \boldsymbol{\delta}\mathbf{W_b}\right)$ and thus in the Jacobian $\mathbf{J}$, and justifies that unsteady perturbations $\mathbf{w}'$ can be considered in Eq. (2.3).

3.3.6 Shape optimization code adaptation

The elsA software includes a shape optimization module in which the discrete RANS equations and various turbulence models were analytically linearized (Peter [104], El Din et al. [105], Peter et al. [106], Renac [107]). We modified this code as stated in Section 3.2.5 in order to enable the computation of both matrices $\mathbf{J}$ and $\mathbf{H}'$, for the turbulence model $k-\omega$ model of Wilcox and the Roe scheme for the mean field convective fluxes, other terms being discretized as described above. Nonetheless, the analytical linearization in the module was done using the thin layer assumption [96], so that we expect to observe some differences when comparing results obtained with this strategy to those obtained by the fully discrete approach.

3.4 Concluding remarks

A fully discrete method was proposed where the discrete equations are linearized using finite differences. Such a procedure is generic regarding the system of equations and can be used in a black box manner. The resolution of an eigenvalue problem being mandatory to perform linear stability analysis, several strategies for matrices inversion

were proposed. An explicit storage of matrices strategy was adopted, which allows immediate access to adjoint matrices required for the computation of the sensitivity gradients. Both direct and adjoint problems are solved using direct methods for matrices inversions. This strategy is fast and accurate and exploits the sparsity of the Jacobian matrix. It however remains costly in terms of computational memory. An on-the-fly strategy was hence described to tackle three dimensional configurations. An efficient procedure was proposed to compute the Jacobian and the Hessian of the RANS equations from residual evaluations, which introduce a particular set of vector intrinsically linked to the stencil discretization. The choice of linearization parameters was also discussed, and a possible adaptation of shape optimization codes to perform linear stability analysis and compute the sensitivity gradients was proposed. Finally, the complete system of equations used in this study and their numerical discretization were described. We will now test the proposed tools and formalisms on several cases to assess the validity of our method.

Chapter 4

Validation on laminar flows

Two incompressible laminar cases are analysed as validation cases for our method in this Chapter, where we reproduce former studies results obtained using a continuous approach. In a first time, we consider in Section 4.1 the oscillator dynamics of the wake behind a two dimensional cylinder. The critical Reynolds number at which the baseflow becomes unstable is determined, and the sensitivity gradients are computed. Ours results show good agreement with those obtained by Marquet et al. [32] on an identical configuration. In a second time, we analyse in Section 4.2 the noise amplifier dynamics of a two dimensional evolving boundary layer. Optimal perturbations are found to correspond to Tollmien-Schlichting waves as expected. The sensitivity gradients are then computed and reproduce the results obtained by Brandt et al. [38].

4.1 Wake behind a two dimensional cylinder

4.1.1 Configuration

We consider a two dimensional cylinder of diameter D in a uniform upstream flow of velocity $\mathbf{U}_\infty = U_\infty \mathbf{e_x}$. As we use a compressible code which does not allow us to impose the incompressibility condition, we set the Mach number to $M = 0.2$. The stagnation temperature is set to 292.5K, and the flow is governed by the laminar Navier-Stokes equations. All quantities are made dimensionless using the cylinder diameter D, the upstream velocity U_∞, density ρ_∞ and viscosity μ_∞, the viscosity being computed using Sutherland's law. The flow characteristics are thus entirely determined by imposing the Reynolds number $R_e = \rho_\infty U_\infty D/\mu_\infty$. This configuration mimics the study by Marquet et al. [32].

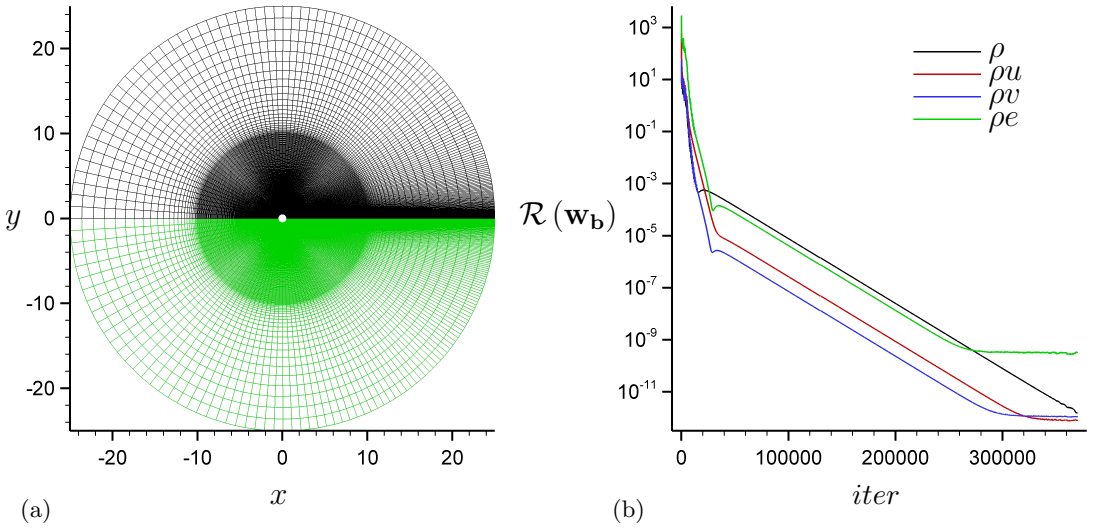

FIGURE 4.1: (a): Mesh discretization of the cylinder. (b): History of residual convergence with the number of iterations during baseflow computation for $R_e = 47$.

The mesh used for the simulation is depicted in Fig.4.1(a). Non-reflexion conditions with upstream flow properties are imposed on the outer part of the configuration while a viscous adiabatic condition is imposed on the cylinder. In order to ease the convergence of the steady solution, the symmetry of the configuration with respect to the plane $y = 0$ is exploited. The baseflow is first computed on a half domain (in black in Fig.4.1(a)) imposing symmetry conditions at the frontier $y = 0$, and is then symmetrized to obtain the baseflow on the full domain required for the stability analysis. The Roe scheme extended to second order (MUSCL) is used for the discretization of the convective flux. The convergence history of the residual for the different conservative variables is depicted in Fig.4.1(b). The steady solution is converged as the different residuals reach a plateau lower than 10^{-8}, ensuring $\mathcal{R}(\mathbf{w_b}) = 0$.

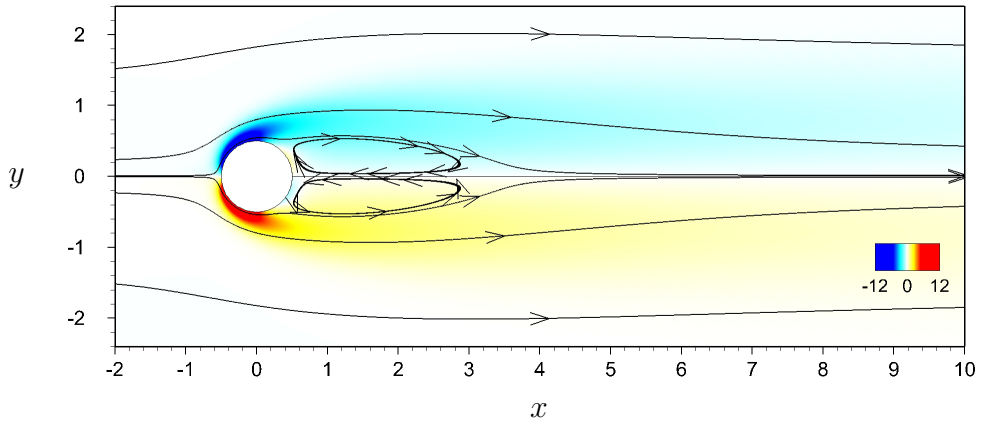

FIGURE 4.2: Velocity streamlines and vorticity contours of the baseflow obtained for $R_e = 47$.

The baseflow streamlines and vorticity contours computed for $R_e = 47$ are plotted

in Fig.4.2. The vorticity is mainly located on the upstream surface of the cylinder. A symmetric recirculation bubble is observed behind the cylinder, with a length (measured from the rear stagnation point) of $L = 3.3$ in agreement with the literature. In the next two Sections, we will follow the method summarized in Section 2.2.3 and compare the computed results with those of Marquet et al. [32].

4.1.2 Critical Reynolds number

As a first validation step, we compute several baseflows in the range $R_e = 40 - 70$. Once each baseflow is obtained, the Jacobian matrix is extracted as presented in Section 3.2.2 and its stability is assessed. The evolution of the least stable eigenvalue growth rate σ and frequency $f = \omega/2\pi$ with the Reynolds number are respectively plotted in Figs.4.3(a) and 4.4(a). We recover a critical number around 47 for which the baseflow becomes unstable with a frequency around $f = 0.117$. For comparison purpose, we plotted in Figs.4.3(b) and 4.4(b) the same results computed by Marquet et al. [32]. Excellent agreement is observed for the growth rate variation σ.

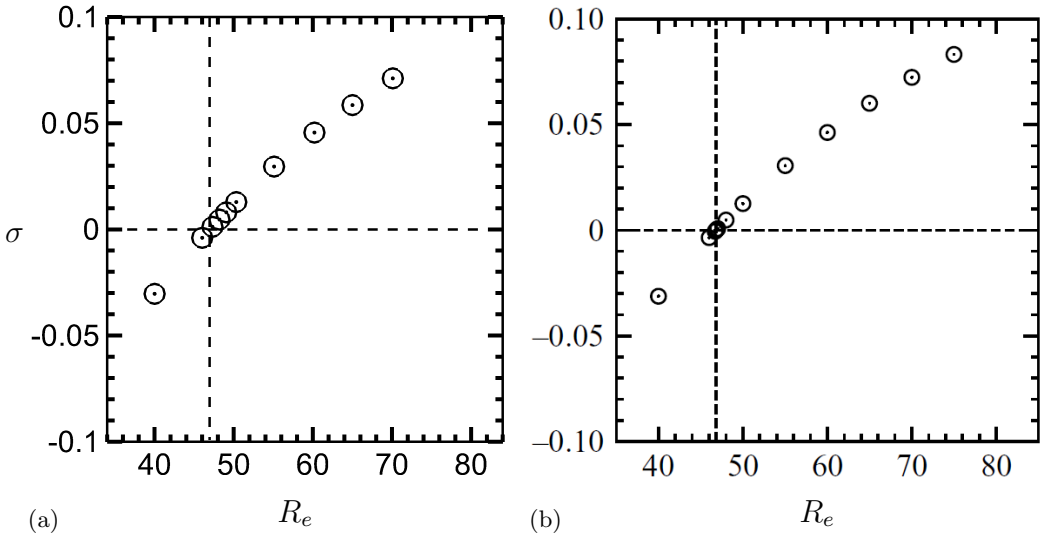

FIGURE 4.3: Comparison of the evolution of the least stable eigenvalue growth rate σ with the Reynolds number R_e between the current study (a) and the results of Marquet et al. [32] (b).

The frequency variation is shifted by 10^{-3} in our case which is still in good agreement with these previous results. Note that this difference is probably linked to numerical errors. These results suggest that the Jacobian matrix $\mathbf{J}$ is correctly computed with our fully discrete approach.

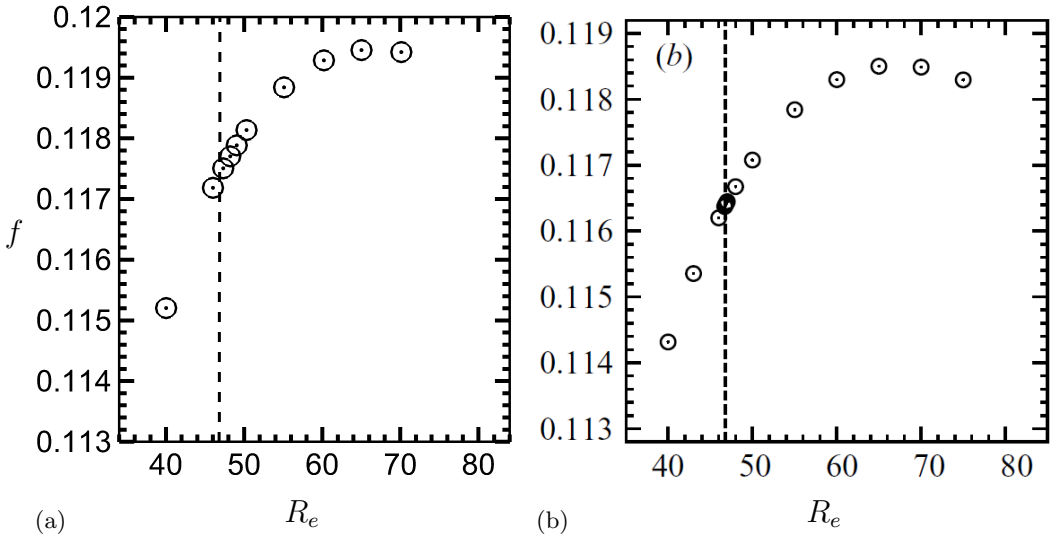

FIGURE 4.4: Comparison of the evolution of the least stable eigenvalue frequency f with the Reynolds number R_e between the current study (a) and the results of Marquet et al. [32] (b).

4.1.3 Direct and adjoint unstable mode

We then consider in more detail the unstable case $R_e = 47$ and perform steps 1 & 2 of Section 2.2.3. The streamwise component ρu spatial structure of the unstable mode $\hat{\mathbf{w}}$ is plotted in Fig.4.5(a) together with the one computed by Marquet et al. [32] in Fig.4.5(b). Note that a mode is defined up to a phase and a normalization which are not given in [32] so that scales are not given here. The mode is antisymmetric and propagates downstream with the formation of typical structures linked to Kelvin-Helmholtz instabilities.

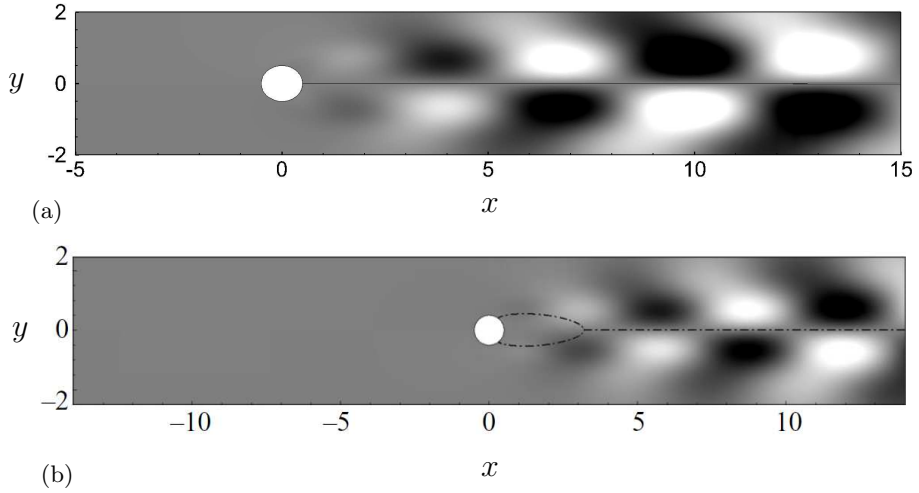

FIGURE 4.5: Comparison of the streamwise component of the unstable mode $\hat{\mathbf{w}}$ at $R_e = 47$ (a) with the study by Marquet et al. [32] (b). The real part is plotted.

The adjoint equations in Eq. (2.10) are solved and the adjoint mode $\tilde{\mathbf{w}}$ computed. We depicted in Fig.4.6(a) the streamwise component of the adjoint mode $\tilde{\mathbf{w}}|_{\mathbf{Q}}$ which is once again compared with the results of Marquet et al. [32] in Fig.4.6(b). The discrete inner-product $\mathbf{Q}$ is used here to compare our results to the continuous approach used in [32], with $\mathbf{Q}$ a diagonal matrix whose terms correspond to the surface of the mesh cells such that:

$$\forall\,(\mathbf{u},\mathbf{v}) \qquad <\mathbf{u},\mathbf{v}>=\sum_{i,j} u_i^* v_i \Omega_{ij} = \mathbf{u}^*\mathbf{Q}\mathbf{v}. \tag{4.1}$$

Both direct and adjoint mode structures are similar to the one computed by Marquet et al. [32]. The adjoint mode propagates upstream while direct mode propagate downstream which comes from the opposite sign of the transport equations in the direct and adjoint problems (see Chomaz [18], Sipp and Lebedev [68]). In particular, the non-normality of the Jacobian matrix $\mathbf{J}$ is recovered here as the spatial structure of both modes $\hat{\mathbf{w}}$ and $\tilde{\mathbf{w}}$ are clearly separated.

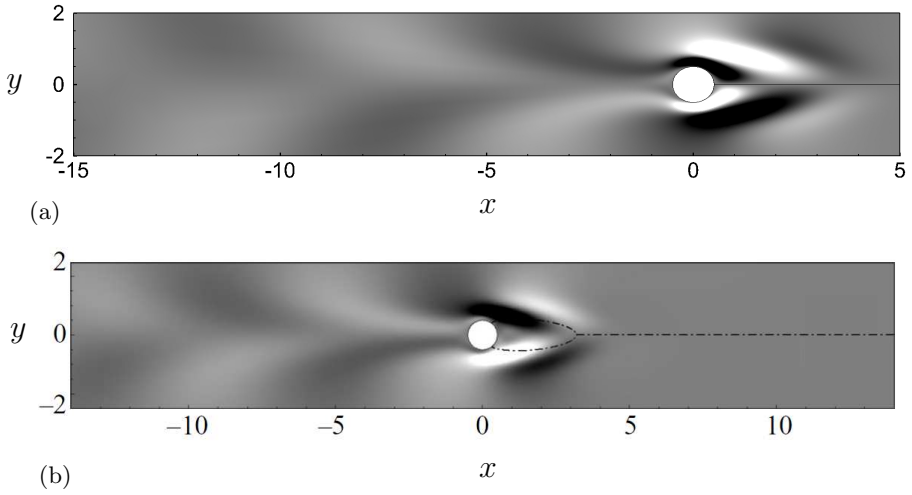

FIGURE 4.6: Comparison of the streamwise component of the adjoint unstable mode $\tilde{\mathbf{w}}|_{\mathbf{Q}}$ at $R_e = 47$ (a) with the study by Marquet et al. [32] (b). The real part is plotted.

4.1.4 Sensitivity gradient to baseflow perturbations

We then perform step 3 of Section 2.2.3 and compute the matrix $\mathbf{H}'$ as presented in Section 3.2.3. The linearization parameters discussed in Section 3.2.4 are set to $\epsilon_1 = 1.0$ and $\epsilon_2 = 5 \times 10^{-6}$. We should mention that as we work using dimensionless variables, all variables are of comparable order between one another (unity). The problem is thus well scaled and the choice of ϵ_2 is facilitated.

The sensitivity gradient of the eigenvalue to baseflow perturbations $\boldsymbol{\nabla}_{\mathbf{w_b}}\lambda$ is then computed according to Eq. (2.19). The real part of sensitivity gradient $\boldsymbol{\nabla}_{\mathbf{w_b}}\lambda$ corresponds

to the sensitivity gradient of the eigenvalue growth rate $\boldsymbol{\nabla}_{\mathbf{w_b}}\sigma$ while its imaginary part relates to the sensitivity of the unstable mode frequency $\boldsymbol{\nabla}_{\mathbf{w_b}}\omega$.

For comparison purpose, we consider the sensitivity gradient of the growth rate to baseflow perturbations occurring on the momentum component $\boldsymbol{\nabla}_{\rho\mathbf{U}}\sigma|_{\mathbf{Q}}$ which we depicted in Fig.4.7(a). It is a vector field represented by its amplitude, its orientation being given by the arrows. Our result clearly differ from the one computed by Marquet et al. [32] in Fig.4.7(b). A similar difference is observed in Figs.4.8(a) and 4.8(b) for the sensitivity gradient of the frequency to baseflow perturbations occurring on the momentum component $\boldsymbol{\nabla}_{\rho\mathbf{U}}\omega|_{\mathbf{Q}}$.

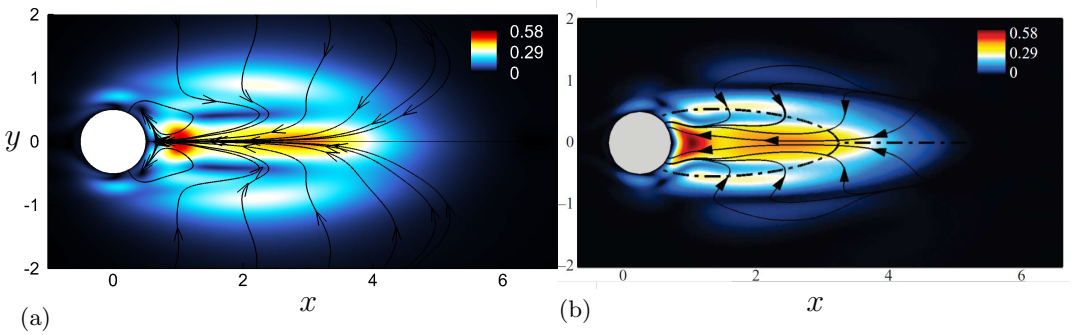

FIGURE 4.7: Comparison of the growth rate sensitivity of the unstable eigenvalue to baseflow perturbation $\boldsymbol{\nabla}_{\rho\mathbf{U}}\sigma|_{\mathbf{Q}}$ (a) with the study by Marquet et al. [32] (b).

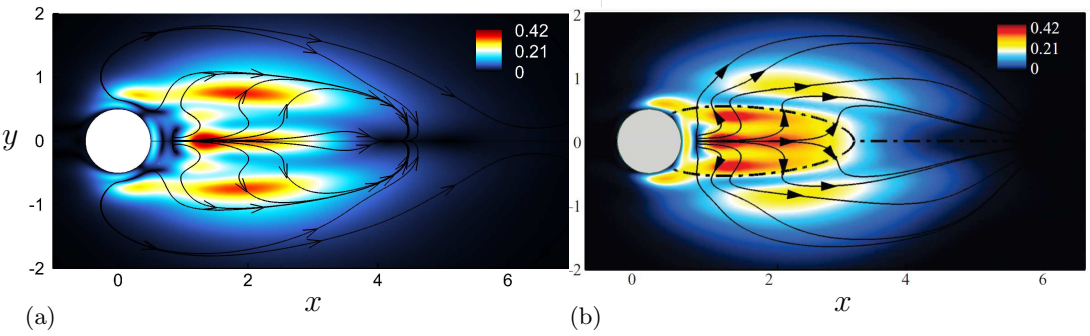

FIGURE 4.8: Comparison of the frequency sensitivity of the unstable eigenvalue to baseflow perturbation $\boldsymbol{\nabla}_{\rho\mathbf{U}}\omega|_{\mathbf{Q}}$ (a) with the study by Marquet et al. [32] (b).

Although our results differ from [32], we recover similar tendencies: far from the cylinder the sensitivities decay to zero due to the spatial separation of the direct and adjoint global modes, while highest magnitudes are reached inside the recirculation region, and the gradients are similarly oriented in the recirculation bubble.

We claim that these differences between both studies come from the compressibility of our equations and do not affect the validity of our results. Indeed, in [32], the equations are incompressible so that the quantity plotted in Fig.4.7(b) actually corresponds to

$\boldsymbol{\nabla}_{\mathbf{U}}\sigma$. Furthermore, although the gradient $\boldsymbol{\nabla}_{\mathbf{w_b}}\lambda$ carries physical information, an arbitrary baseflow modification is not physically relevant. As a consequence, comparing the impact of two arbitrary baseflow perturbations with different dynamics (a compressible and an incompressible one) does not make sense. Hence, such a difference between both gradients is not necessarily surprising. The fact that both results are similarly oriented is however reassuring as $\boldsymbol{\nabla}_{\rho\mathbf{U}}\sigma|_{\mathbf{Q}}$ indicates us that the instability is reduced when blowing inside the recirculation bubble, a fact known from experiments.

For both results to be compared, a constraint with a physical meaning should be applied to these gradients to enable a relevant comparison. A not so simple way to do this would be to compute the divergence free part of the gradients and compare them. Indeed, as the dynamics is mostly incompressible, only the divergence free part of the gradient works in the eigenvalue variation. Computing the divergence free part of the gradients should thus lead to a good overlapping of both studies. However, this approach is complex and would require the datas computed in [32].

We chose to set a different constraint on the gradients by imposing the baseflow modification to stem from a steady force. As stated in Section 2.2.2, the baseflow perturbation induced by a steady force can be computed using the inverse of the Jacobian $\mathbf{J}^{-1}$. In particular, such a perturbation takes into account the inherent physics of the problem, notably the fact that the flow occurs at a low Mach number. This choice naturally leads to the definition of the sensitivity gradient to a steady force perturbation $\boldsymbol{\nabla}_{\mathbf{f}}\lambda$, which are now relevant quantities to be compared with the results in Marquet et al. [32].

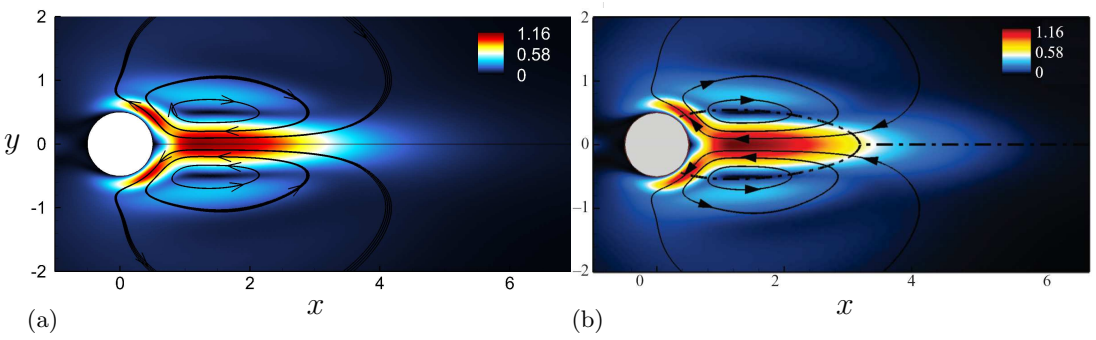

FIGURE 4.9: Comparison of the amplitude and direction of the momentum component of the growth rate sensitivity to a steady force $\boldsymbol{\nabla}_{\mathbf{f}}\sigma|_{\mathbf{Q}}$ (a) with the study by Marquet et al. [32] (b).

We thus computed this gradient to a steady force perturbation and decomposed it once again into its real and imaginary parts. The amplitude and direction of the momentum component of the growth rate sensitivity to a steady force $\boldsymbol{\nabla}_{f}\sigma|_{\mathbf{Q}}$ and of the frequency sensitivity to a steady force $\boldsymbol{\nabla}_{f}\omega|_{\mathbf{Q}}$ are respectively plotted in Figs.4.9(a) and 4.10(a).

They show excellent agreement with those computed by Marquet et al. [32] which are represented in Figs.4.9(b) and 4.10(b).

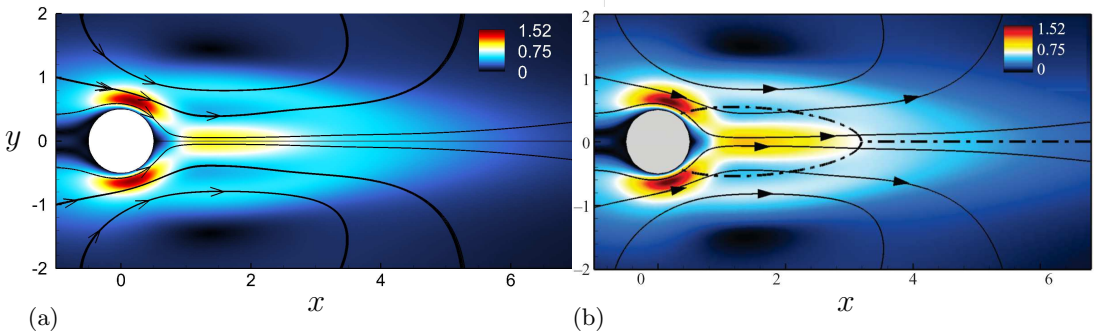

FIGURE 4.10: Comparison of the amplitude and direction of the momentum component of the frequency sensitivity to a steady force $\boldsymbol{\nabla}_{\mathbf{f}}\omega|_{\mathbf{Q}}$ (a) with the study by Marquet et al. [32] (b).

Three regions in the vicinity of the cylinder and extending a few diameters downstream may be identified: the separation region near the separation point on the cylinder, the recirculation region, and the outer region corresponding to the region half a diameter in size surrounding the recirculation region. Two strong local maxima of the growth rate sensitivity to a steady force may be distinguished. The first is located in the vicinity of the separation point and the second in the recirculation region, close to the centerline. A local force oriented in the opposite direction to the arrows plotted in Fig.4.9(a) induces a negative variation of the growth rate which is proportional to the local magnitude of the sensitivity function. Therefore, near the separation and inside recirculation regions, a local force is stabilizing when oriented downstream. The opposite is true in the outer region. The frequency sensitivity is oriented downstream everywhere in the flow in Fig.4.10(a). In particular, a stabilizing local force is associated with an increase of the frequency both near the separation and inside recirculation regions.

These results are in excellent agreement with the results of Marquet et al. [32], suggesting that the proposed method is a valid candidate to perform stability analysis of laminar flows. Furthermore, this approach allowed us to validate our gradients in the case of oscillators dynamics.

4.2 Evolving boundary layer over a flate plate

4.2.1 Configuration

We consider a uniform flow $\mathbf{U}_\infty = U_\infty \mathbf{e_x}$ impinging on a flat plate located at $(x, y) = (0, 0)$ and extending up to $x = 1.25$. We impose the Mach number $M = 0.3$ with a static

temperature $T_\infty = 283$K, which poorly affects the results compared to the incompressible case as will be shown in the following. We use a reference length L shorter than the flat plate, and set the Reynolds number based on L to $R_e = 6 \times 10^5$. The viscosity is computed according to Sutherland's law, and all quantities are made dimensionless using the upstream velocity $\mathbf{U}_\infty$, temperature $\mathbf{T}_\infty$, density ρ_∞ and the reference length L. The computational domain and the imposed boundary conditions are sketched in Fig.4.11(a).

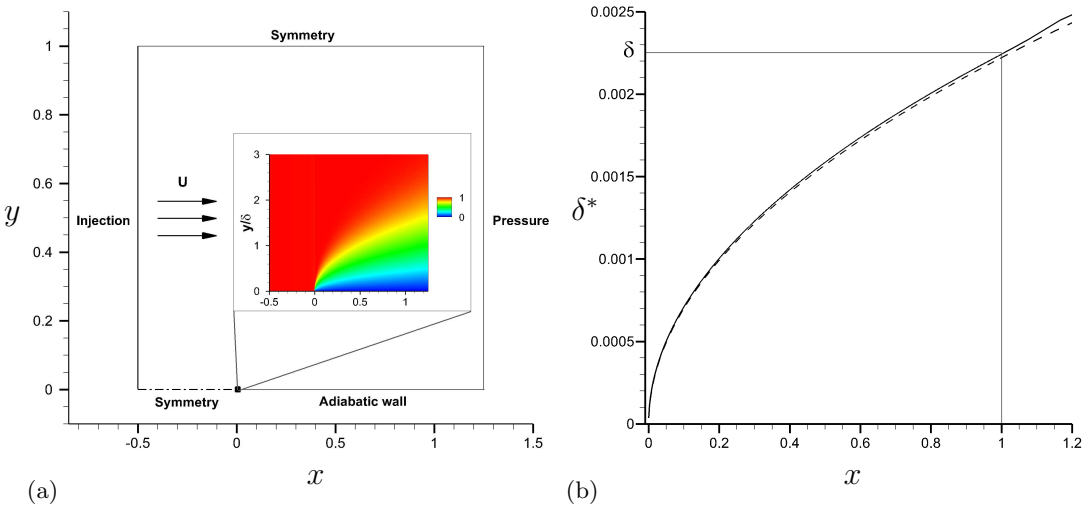

FIGURE 4.11: (a): Domain and boundary conditions. In the inlet are depicted streamwise velocity contours of the baseflow (in boundary layer units). (b): Comparison of the computed displacement thickness δ^* (plain line) with the Blasius boundary layer solution (dotted line).

We impose an injection condition at the entrance of the domain ($x = -0.5$), a symmetry condition on the upper part ($y = 1.0$), and set the pressure p_∞ at the exit ($x = 1.25$). The flat-plate boundary is taken as an adiabatic wall while a symmetry condition is imposed upstream of the plate for $x \in [-0.5, 0]\,, y = 0$. Roe scheme extended to second order is used for the discretization of the convective flux. The domain is discretized on y using a tangential evolution of the discretization step imposing for the first cell on the wall $\Delta y = 10^{-5}$. A uniform discretization on the plate is used for $x \in [0, 1]$ with $\Delta x = 2 \times 10^{-4}$. A tangential evolution for the increase of the discretization step size is finally used to meet the inlet and outlet boundary conditions. This configuration mimics the study of Brandt et al. [38].

The baseflow $\mathbf{w_b}$ is first computed, the streamwise velocity contours near the edge of the plate can be observed in the inlet of Fig.4.11(a). Note that as this case is stable, the convergence of the baseflow is easily obtained. For validation purpose, we compute the displacement thickness δ^* along the plate and compare it in Fig.4.11(b) to the analytical expression $\delta^* = 1.72 R_e^{-1/2} \sqrt{x}$ obtained for the asymptotic Blasius similarity solution.

The development of the boundary layer is observed to be very close to the Blasius solution similarly to [38]. In the following, we will refer to the quantity δ defined as the displacement thickness at $x = 1$, and the frequency $F = 10^6\omega/R_e$ will be used for convenience. We will follow the method summarized in Section 2.3.5 in order to characterize the dynamics of the boundary layer.

4.2.2 Optimal gain

The noise amplifier dynamics of the boundary layer is analysed by considering the optimal energetic gain μ^2 for a given harmonic forcing at the frequency ω. Following step 1, we first extract the Jacobian matrix $\mathbf{J}$ according to the procedure detailed in Section 3.2.2. The resolvent matrix $\mathscr{R}_\omega$ is then computed for several values of harmonic forcing at the pulsation ω. Similarly to [38], the energy maximization is restricted to the domain $x \in [0, 1]$ (with no restriction on y), we thus use the pseudo-scalar product $\mathbf{Q_e}$ for the energy maximization as described in Section 2.3.3. The previously introduced inner-product $\mathbf{Q}$ is used for the normalization of the forcing terms. Finally, as explained in Section 2.3.4, we impose a restricted forcing $\hat{\mathbf{f}}_\mathbf{s}$ solely acting on the momentum components. The prolongation operator $\mathbf{P}$ is thus straightforwardly obtained by adding 0 to the extended vector $\hat{\mathbf{f}} = \mathbf{P}\hat{\mathbf{f}}_\mathbf{s}$. All quantities required in step 2 (Section 2.3.5) are now defined and we can thus perform step 3 solving Eqs. (2.77) and (2.76).

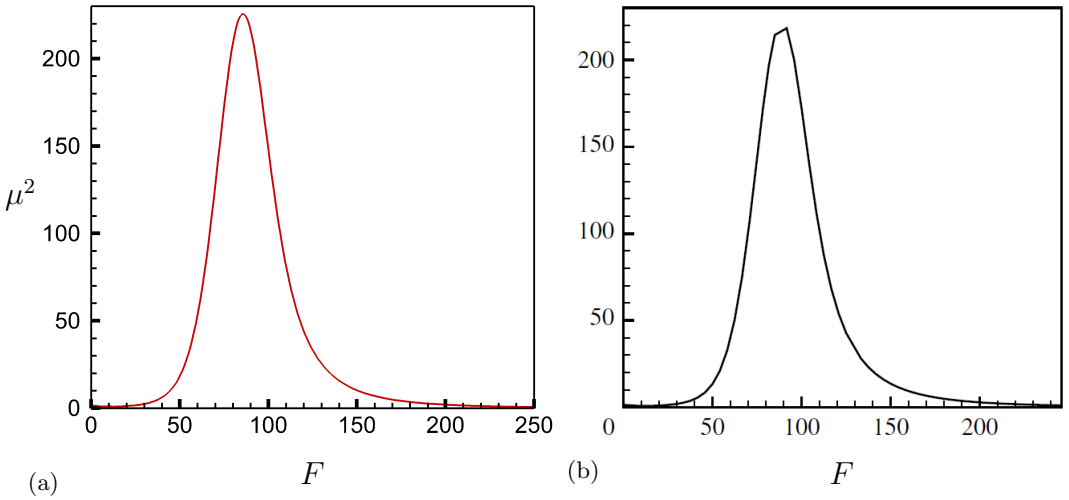

FIGURE 4.12: Comparison of the optimal gain μ^2 variation with the frequency F between the current study (a) and the results by Brandt et al. [38] (b).

The variation of the gain μ^2 with the frequency F is plotted in Fig.4.12(a) and shows excellent agreement with the one computed by Brandt et al. [38] depicted in Fig.4.12(b). We recover a maximum gain around the frequency $F = 88$ with an optimal gain of $\mu^2 = 225$ close to [38]. We can notice the noise amplifier dynamics of the boundary layer

which acts as a filter that enables strong amplifications of harmonic forcing located within the range $F \in [50,150]$.

	I_{max}	J_{max}	Number of cells	dx/dy	λ/dx
mesh	3567	249	888×10^3	28.5	133
coarse x	1817	249	452×10^3	57	67
coarse $2x$	867	249	215×10^3	125	30
coarse y	3567	149	531×10^3	28.5	133
coarse xy	1817	149	270×10^3	57	67
fine y	3567	349	1.24×10^6	28.5	133

TABLE 4.1: Properties of the different meshes used for the gain function convergence. dx/dy is given for the first discretization cell near the flat plate.

4.2.3 Mesh convergence

In order to better comprehend the impact of the mesh choice onto our results, we varied the discretization and computed the gain functions for several meshes described in Table 4.1. For each mesh, the baseflow $\mathbf{w_b}$ is first computed, the Jacobian matrix $\mathbf{J}$ is then extracted and finally the gain μ^2 is calculated for several frequencies F ranging in the interval $F \in [50,150]$.

The variations between the meshes correspond to a modification of the discretization of the boundary layer. In the streamwise direction x, as the mesh is uniformly discretized, we vary the discretization step (dividing it by 2 in coarse x, and 4 in coarse $2x$). In the crosswise direction y, we increase (fine) or decrease (coarse) the number of discretization points. As the discrete step dy follows a tangential repartition, these variations mainly impact the discretization within the boundary layer. The different mesh characteristics are described in Table 4.1.

We shall remark here that Brandt et al. [38] used finite elements in their study with triangular isosceles cells for the discretization. As the boundary layer mainly develops in the crosswise direction, such a procedure is computationally intense since the configuration is over discretized in the x direction. Using finite volumes here, we are able to stretch the cells in the x directions, we thus also give in Table 4.1 the stretching dx/dy of the first discrete cell near the wall (note that finite elements methods also allow such stretching).

The different gain function are plotted in Fig.4.13 together with the one depicted in Fig.4.12(a). Several remarks can be made. We do observe a convergence of the gain curve with the mesh, but notice that both the gain value and the location of the maximum of the curve are strongly influenced by the mesh discretization. The discretization

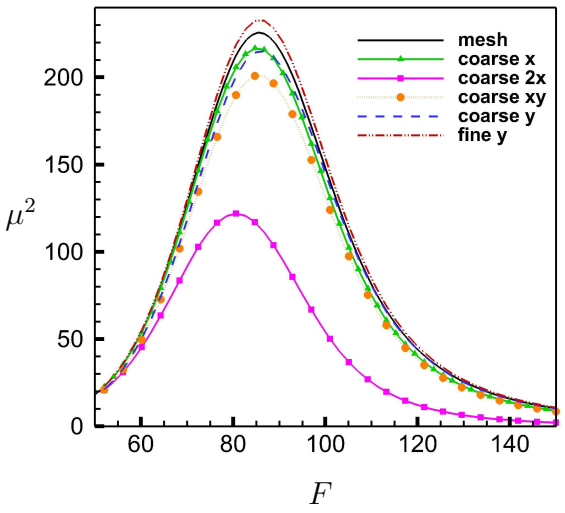

FIGURE 4.13: Convergence of the gain function μ^2 with the mesh discretization.

in the streamwise direction x appear to be of fundamental importance in order to accurately compute the gain μ^2. We can remark that most discretization points are used to discretize the streamwise direction which is generally not the case for traditional analysis of boundary layers but necessary for stability analysis here. This is most likely due to the quick evolution of optimal forcing and response in this direction as will be observed in Figs.4.14(a) and 4.15(a). We evaluated the wave length λ of the optimal answer in Fig.4.15(a) and gave in Table 4.1 the ratio λ/dx which indicate for each mesh the number of discrete points in one wavelength. The discretization in the y direction seems to have a poorer impact on the gain curve. Note that the final mesh used (mesh) does not necessarily yields the completely converged curve although it provides good agreement with [38].

	$N \times 10^{-6}$	M_v	$n_e \times 10^{-6}$	$n_e^{obt} \times 10^{-6}$	n_e^{obt}/N^2	M_J
mesh	4.4	35MB	289	15.2	7.7×10^{-6}	2.4GB
coarse x	2.3	18MB	147	77.4	1.5×10^{-5}	1.2GB
coarse $2x$	1.1	8 MB	70	36.9	3.2×10^{-5}	0.6GB
coarse y	2.7	21MB	173	90.8	1.3×10^{-5}	1.4GB
coarse xy	1.4	11MB	88	46.2	2.5×10^{-5}	0.7GB
fine y	6.2	49MB	405	213	5.5×10^{-6}	3.3GB

TABLE 4.2: Matrix and vector properties for the different meshes used with $n_c = 4$ and $n_{res} = 2 \times 100$.

Finally, in order to give an idea of the typical costs of our method, we depicted in Table 4.2 the characteristic dimensions of our problem for the different meshes used. We recall that we consider here a two dimensional flow, we thus have $n_c = 4$ conservative variables, and require $n_{res} = 2 \times 100$ residual evaluations to compute the Jacobian matrix with second order precision. We detailed in Table 4.2 the vector size N as well as M_v the

memory cost of storing one vector. Similarly, the theoretical n_e and obtained n_e^{obt} number of elements of the Jacobian are given, together with the ratio n_e^{obt}/N^2 quantifying the Jacobian sparsity, and the memory cost of storing the matrix M_J. Note again that the formula giving the total number of elements n_e was derived in Section 3.2.2, assuming that all the conservative variables intervene in each equations. This is not necessarily the case which explains the lower number of actual non zero elements obtained n_e^{opt}.

4.2.4 Optimal forcing and response

In the following, we further characterize the forcing frequency case $F = 100$. The spatial structures of the optimal forcing $\tilde{\mathbf{f}}$ and response $\hat{\mathbf{x}}$ are respectively depicted in Figs.4.14(a) and 4.15(a), and compared to the one computed by Brandt et al. [38] in Figs.4.14(b) and 4.15(b). Note that Brandt et al. used a parabolic step upstream of their flat plate in order to ease the computation of the baseflow. We used instead an infinitesimally small flat plate and thus we added a black rectangle to our figures in order to ease the comparison with their results.

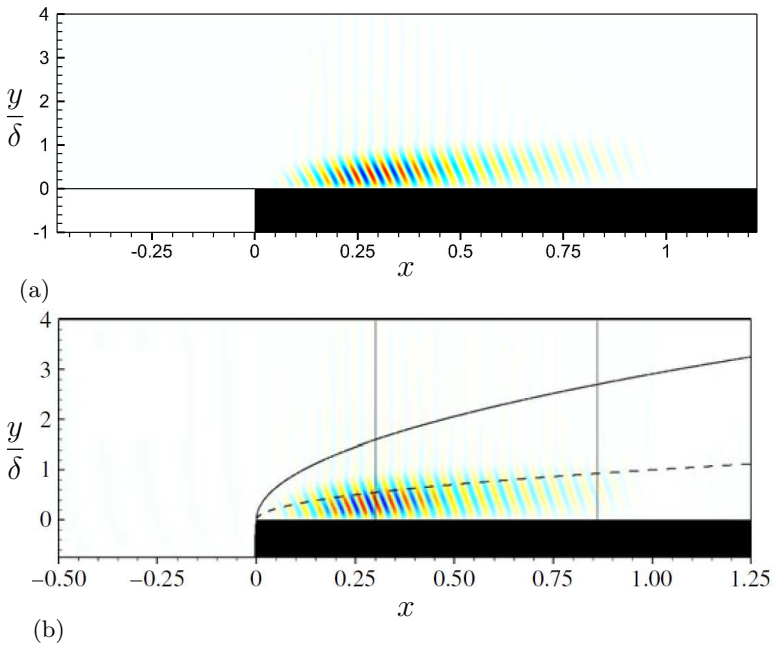

FIGURE 4.14: Comparison of the streamwise component of the optimal forcing $\tilde{\mathbf{f}}$ at $F = 100$ (a) with the study by Brandt et al. [38] (b).

Both optimal forcing and optimal response show good agreements with [38]. Note once again that these terms are defined up to a phase and a normalization so that scales were not plotted. We can observe a slight difference between the response terms in Figs.4.15(a) and 4.15(b) for $x > 1$ which probably comes from the strong decrease of mesh refinement we imposed in this zone. However, as this area of the flow is not

taken into account in the optimization process for the gain computation, such a small discrepancy poorly affects our results.

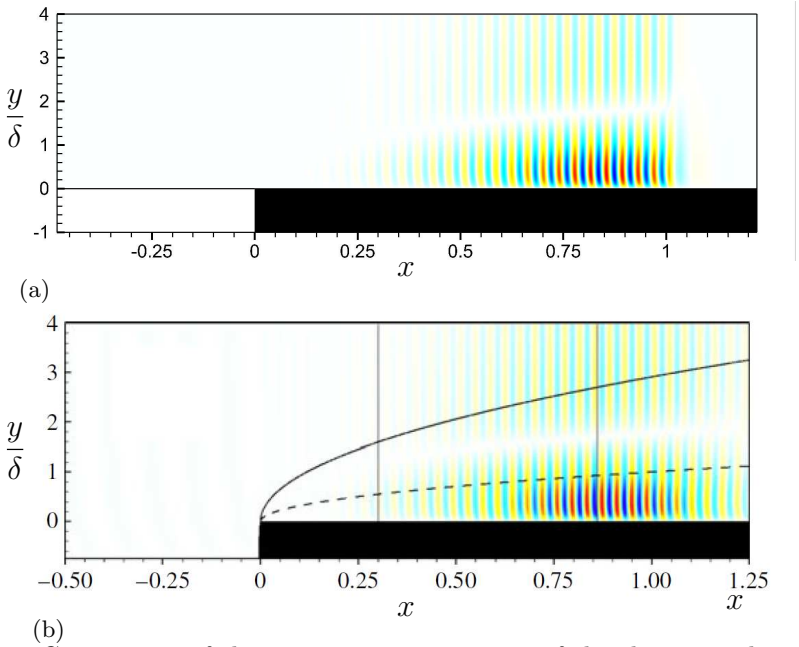

FIGURE 4.15: Comparison of the streamwise component of the the optimal response $\hat{\mathbf{x}}$ at $F = 100$ (a) with the study by Brandt et al. [38] (b).

The optimal response consists of a series of waves clearly localized downstream of the flat plate and reaches a maximum around $x = 0.9$. These structures correspond to Tollmien-Schlichting waves. Inversely, the optimal forcing is localized upstream and reaches a maximum around $x = 0.25$. The non-normality of the Jacobian matrix $\mathbf{J}$ is once again recovered in the comparison of the spatial structure of the optimal forcing and response. Indeed, the disturbance $\tilde{\mathbf{f}}$ is dominated by its streamwise component, while the optimal response $\hat{\mathbf{x}}$ is equally distributed on its streamwise and cross-stream components. The streamwise forcing is dominant because the forcing is leaning against the shear of the baseflow, suggesting that the well-known Orr mechanism is also at play to efficiently initiate the Tollmien-Schlichting instability as explained in Åkervik et al. [108].

4.2.5 Gain sensitivity to baseflow perturbation

Following step 4 (Section 2.3.5), the matrix $\mathbf{H}'$ is then computed as presented in Section 3.2.3, setting the perturbation parameters discussed in Section 3.2.4 to $\epsilon_1 = 1.0$ and $\epsilon_2 = 5 \times 10^{-6}$. Similarly to the cylinder case, the variables are of similar order of magnitude near unity. The gain sensitivity to baseflow perturbation $\boldsymbol{\nabla}_{\mathbf{w_b}}\mu^2$ is then computed according to Eq. (2.53). We depicted in Fig.4.16(a) the obtained field $\boldsymbol{\nabla}_{\mathbf{w_b}}\mu^2|_{\mathbf{Q}}$.

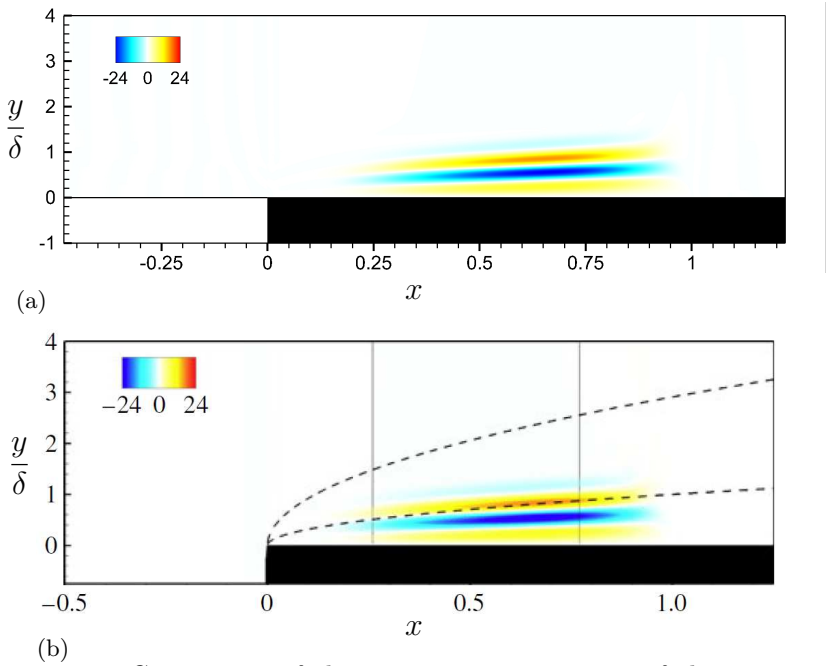

FIGURE 4.16: Comparison of the streamwise component of the gain sensitivity to baseflow perturbation $\nabla_{\mathbf{w_b}}\mu^2|_{\mathbf{Q}}$ at $F = 100$ (a) with the study by Brandt et al. [38] (b).

We observe an excellent agreement with the results of [38] which are depicted in Fig.4.16(b). This field is weakly varying in the streamwise direction but exhibits strong variations in the cross-stream direction. The baseflow is found to be sensitive to external perturbations only in the vicinity of the flat plate. We shall remark that contrarily to the cylinder case, both incompressible and compressible gradients are identical. In Fig.4.16(b), Brandt et al. [38] depicted the divergence free part of the gradient. We believe that this similarity is due to the fact that in this case both divergence free and non-divergence free part of the gradient are nearly identical.

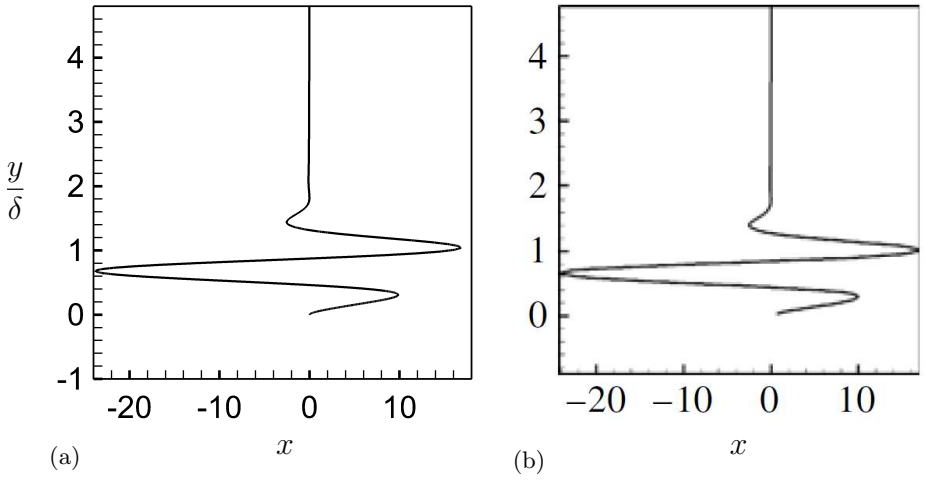

FIGURE 4.17: Comparison of the wall normal gain sensitivity to baseflow perturbation at the station $x = 0.7$ for $F = 100$ (a) with the study by Brandt et al. [38] (b). The y coordinate is here normalized with the local displacement thickness δ^* ($x = 0.7$)

A final validation step is taken by considering the wall normal gain sensitivity to baseflow perturbation at the station $x = 0.7$ in Fig.4.17(a) and comparing it with the results of [38] in Fig.4.17(b) (the streamwise component of the gradient is considered). Both variation of the sensitivity gradient with y (in boundary layer units) are found identical. These results demonstrate that our gradients are correctly computed in the case of laminar flows.

4.3 Concluding remarks

The oscillator dynamics of a two-dimensional cylinder was studied and the critical Reynolds number for flow instability was recovered. The sensitivity gradients to baseflow perturbations and steady force were computed and show good agreement with those computed by Marquet et al. [32]. The noise amplifier dynamics of a boundary layer was also analysed. The optimal gain curve was computed and optimal forcing and response structure detailed. The sensitivity gradient of the optimal gain to baseflow perturbation was finally extracted and reproduce the results obtained by Brandt et al. [38]. The coherence observed with previous results demonstrates that both oscillators and noise amplifiers dynamics can be characterized using our fully discrete formalism in the case of laminar flows. Moreover, it also validates the laminar computation of our gradients. We will now extend this validation to a compressible turbulent flow in the next Chapter.

Chapter 5

Sensitivity analysis of a turbulent compressible flow over a deep cavity

We explore in this Chapter the dynamics of a turbulent compressible flow over a deep cavity. The flow configuration was experimentally characterized by Forestier et al. [83], while Larchevêque et al. [84] showed that three-dimensional large-eddy simulations reproduced the flow dynamics. Further experimental analyses including steady control were carried out by Illy et al. [109] and Yamouni [110]. In a first hand, this case will enable us to demonstrate the valuable information that both stability and sensitivity analysis provide compared to experimental results. In particular, the coherence of the physical information obtained suggest the relevancy and the correctness of the current method. In a second hand, the fully discrete procedure proposed in this study will be extensively analysed on this configuration. Genericity of the method with the system of equations, influence of the numerical scheme and physical modeling onto the results, convergence with the linearization parameters, and finally validity of the gradients will be demonstrated.

The configuration, baseflow computation and unsteady dynamics of the cavity will first be detailed in Section 5.1, and typical size of the Jacobian matrices will also be presented. Section 5.2 is dedicated to the linear study of the cavity dynamics. The unstable modes are presented and their physical properties analysed. The impact of the mesh discretization onto the spectrum as well as the equations choice are also investigated. Finally, the convergence of the eigenvalues with the linearization parameter is proven and the properties of the adjoint modes are detailed. The sensitivity analysis is performed in Section 5.3 were the sensitivity gradients are computed. The validity of the gradients is tested

using a discrete evaluation of eigenvalue variation. A previsional control map using a small steady cylinder as a means to control the flow is computed. Finally, a particular analysis of the linearization of the Spalart-Allmaras turbulence model is performed in Section 5.4.

5.1 Characterization of the cavity

5.1.1 Configuration

We consider a two dimensional cavity of height $D = 0.12$m and width $L = 0.05$m ($L/D = 0.42$) as illustrated in Fig.5.1(a). The flow is compressible with a Mach number $M = 0.8$, stagnation conditions being equal to 94400Pa for the pressure and 292.5K for the temperature. The Reynolds number based on the free stream velocity U_∞, density ρ_∞, temperature T_∞, the cavity length L and Sutherland's law for the viscosity is equal to $R_e = 860000$. We impose a turbulent parallel profile with a boundary layer thickness δ=2.3mm at the inlet of the domain. The lower part of the domain is composed of an adiabatic wall, while a wall slip condition is imposed on the upper part of the domain, the outlet static pressure p_∞ being fixed at 61900Pa. All quantities are made dimensionless using the free stream variables ρ_∞,U_∞,T_∞ and the cavity length L.

	x	y	Discretization points	Number of cells
Bloc 1	$-1 \leq x_1 \leq 0$	$0 \leq y_1 \leq 2$	151×221	33000
Bloc 2	$0 \leq x_2 \leq 1$	$-2.4 \leq y_2 \leq 2$	401×601	240000
Bloc 3	$1 \leq x_3 \leq 5$	$0 \leq y_3 \leq 2$	101×221	22000

TABLE 5.1: Definition of the blocs and their discretization properties.

The mesh used for the simulations is depicted in Fig.5.1(a) and is composed of three vertical blocs. For each block, we either use a tangential or semi-tangential law for the evolution of the discretization step. The cells adjacent to the cavity corners are squares of size $\Delta x = 7.0E-05$ imposing $\Delta y^+ = 1.4$ on the upstream wall, ensuring that the first discretization points are inside the viscous sublayer. Each bloc properties are summarized in Table 5.1, yielding a total number of cells $N_m = 295000$. The various discretization schemes proposed in Section 3.3.4 for the convective flux are used as well as both Spalart-Allmaras and $k-\omega$ Wilcox turbulence models.

5.1.2 Baseflow computation

Convergence of the baseflow is assessed by ensuring that the explicit residuals of the mean field equations are small (typically 10^{-8}) and that the residual of the turbulent equations have decreased by several orders of magnitude. Streamlines and streamwise velocity component of the baseflow $\mathbf{w_b}$ obtained with the Roe scheme and the $k-\omega$ model of Wilcox are plotted in Fig.5.1(b).

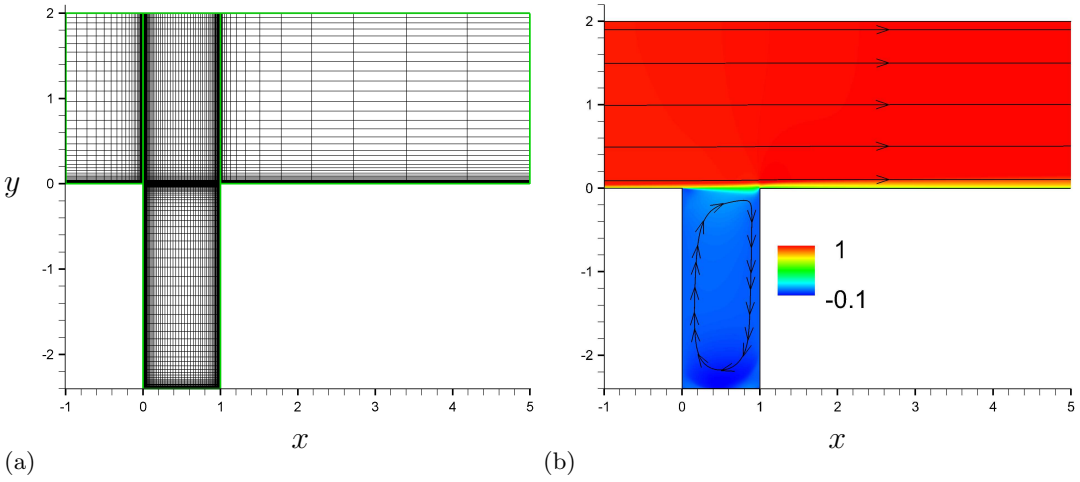

FIGURE 5.1: (a): Mesh discretization example. (b): Baseflow streamlines and streamwise velocity contours.

We observe the formation of a mixing layer induced by the presence of a large recirculation bubble inside the cavity, growing from the upstream corner of the cavity. This configuration corresponds to the experimental study of Forestier et al. [83] who characterized this flow to be unsteady with a dominant frequency around 2000 Hz ($\omega = 2.4$). The mixing layer is subject to Kelvin-Helmholtz instabilities which lead to the creation of vortices that impact the downstream corner of the cavity. This impact generates pressure waves propagating upstream that perturb the mixing layer sustaining the instability mechanism. This mechanism of aeroacoustic feedback was proposed by Rossiter [111].

In order to compare the results obtained with the different turbulence models and discretization schemes regardless of their dependence to the baseflow, we chose to keep the depicted baseflow for all stability computations (regardless of the equations to linearize for the stability analysis). Similarly to the work of Deck et al. [112], a conversion function is applied to compute $\rho\tilde{\nu}$ for the Spalart-Allmaras model from ρk and $\rho\omega$ by matching the eddy viscosity of both models.

5.1.3 Unsteady dynamics

The unsteady RANS equations closed with the $k-\omega$ model of Wilcox are known to well reproduce the frequency selection of the natural flow as well as the dynamics of the large scale structures of the turbulence (Lawson and Barakos [9]). We integrate Eq. (2.1) in time for a field $\mathbf{w}(t)$ initialized from the baseflow $\mathbf{w}(0) = \mathbf{w_b}$. We thus observe at small times of the computation the natural growth of an arbitrary perturbation due to numerical noise and superimposed onto the baseflow. The evolution of the pressure extracted at the downstream corner of the cavity is plotted in the lower inward of Fig.5.2(a).

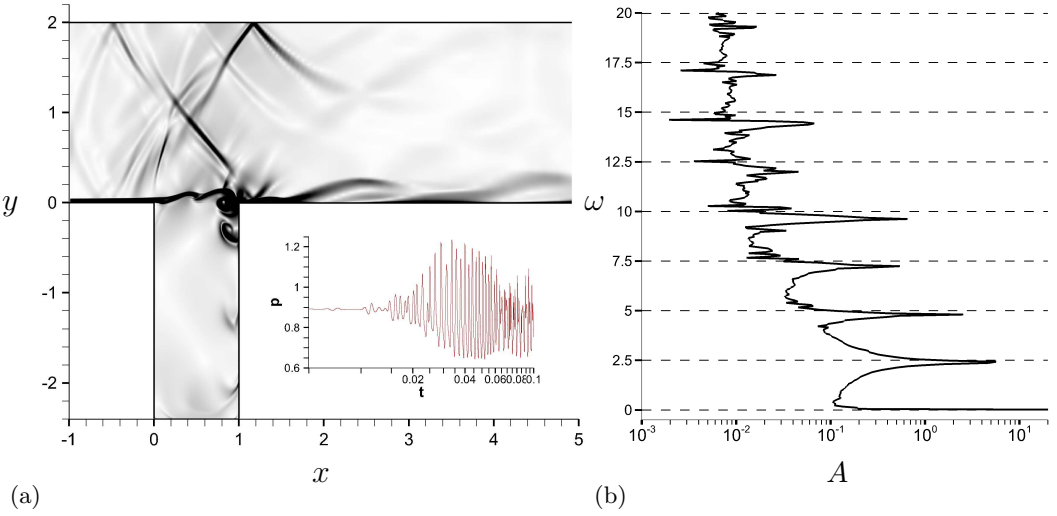

FIGURE 5.2: (a): Contours of the norm of the density gradient $\|\nabla\rho\|$ for a arbitrary time in the periodic regime. In the inward is depicted the pressure signal extracted at the downstream corner of the cavity for small times. (b): Spectrum amplitude A (arbitrary scale) of the flow computed with the unsteady simulation results. We recover the fundamental frequency around $\omega = 2.4$ as well as several harmonics.

We observe at small times features corresponding to unstable modes evolution: the perturbation oscillates and grows inside an exponential envelope. At larger times the perturbation saturates and a periodic regime establishes. We depicted in Fig.5.2(a) the contours of the norm of the density gradient $\|\nabla\rho\|$ at an arbitrary time in the periodic regime. We recover features of the aeroacoustic feedback mechanism of Rossiter [111] with the vortex formation, the impact on the downstream corner and the propagation of pressure waves. Finally, we compute the flow spectrum using the extracted pressure signal. The uRANS spectrum is depicted in Fig.5.2(b): we recover the natural frequency around 2000Hz ($\omega = 2.4$) as well as several harmonics, in agreement with the experimental study of Forestier et al. [83]. The unsteady RANS equations reproduce well the flow dynamics especially the frequency selection. A stability analysis of the baseflow

is thus performed in order to link the uRANS unsteadiness to unstable mode(s) of the steady RANS solution $\mathbf{w_b}$.

5.1.4 Memory cost of Jacobian computation, storage and inversion

The baseflow $\mathbf{w_b}$ being computed, the Jacobian matrix $\mathbf{J}$ is extracted with the method presented in Section 3.2 and stored on disk. The method requires $n_{res} = 25n_c$ residual evaluations (times 2 for second order precision) and each vector of size N shall be stored. The quantities characterising the Jacobian size for both $k-\omega$ and Spalart-Allmaras turbulence models are summarized in Table 5.2, where we introduce M_v and M_J the memory costs of storing a real vector and the Jacobian matrix respectively.

Model	n_c	N	M_v	n_{res}	n_e	n_e^{obt}	n_e^{obt}/N^2	M_J
Spalart-Allmaras	5	1475.10^3	11 MB	125	96.10^6	63.10^6	3.10^{-05}	0.9 GB
$k-\omega$	6	1770.10^3	14 MB	150	138.10^6	80.10^6	3.10^{-05}	1.2 GB

TABLE 5.2: Jacobian matrix dimensions.

We can remark that the obtained number of non zero elements n_e^{obt} is about 30 percent lower than the maximum potential non zero elements n_e introduced in Section 3.2. This is not surprising as all conservative variables do not intervene in each equation. The matrices are sparse with very small ratio of non zero elements to their size n_e^{obt}/N^2.

Model	Max memory	Number of procs	Memory per proc	Time per proc
Spalart-Allmaras	52 GB	24	2.1 GB	214 s
$k-\omega$	65 GB	24	2.7 GB	256 s

TABLE 5.3: Jacobian matrix inversion cost.

The eigenvalue problem in Eq. (2.5) is then solved using a shift and invert strategy with direct inversion of the matrix as described in Section 3.1.1. Direct inversions are fast and accurate but require large amount of memory. We show in Table 5.3 the total computational cost of one direct inversion of a complex matrix (we use complex shifts to focus on some particular eigenvalues) in terms of maximum amount of memory, number of processors and computational time per processors. The maximum memory is reached during the LU factorization of the matrix and is about 50 times the matrix size, the inversions being quickly processed. We foresee that the increase of memory would become prohibitive for very large systems ($n_e^{obt} > 10^9$). Note that the scope of this study is not to propose an optimal method in terms of computational time or memory cost to compute the sensitivity gradients, but lies in the discrete definition and computation of

these quantities. However, the method overview presented in Section 3.1.2 presents a fully on-the-fly approach for optimization of this procedure.

5.2 Flow dynamics analysis

5.2.1 Linear stability versus unsteady simulations

We first consider the results obtained with the $k-\omega$ model of Wilcox and the Roe scheme for the convective flux discretization. Solving the eigenvalue problem in Eq. (2.5) we obtain the set of unstable eigenvalues depicted in Fig.5.3(a): the cavity flow dynamics corresponds to an oscillator. We recover a spectrum similar to the one computed by Yamouni et al. [113] for a laminar compressible flow in a square cavity. We observe an upper branch (modes $1-7$, denoted with square symbols □) seemingly corresponding to Kelvin-Helmholtz modes and a lower branch (modes $8-13$, denoted with circle symbols ○) that we attribute to acoustic modes.

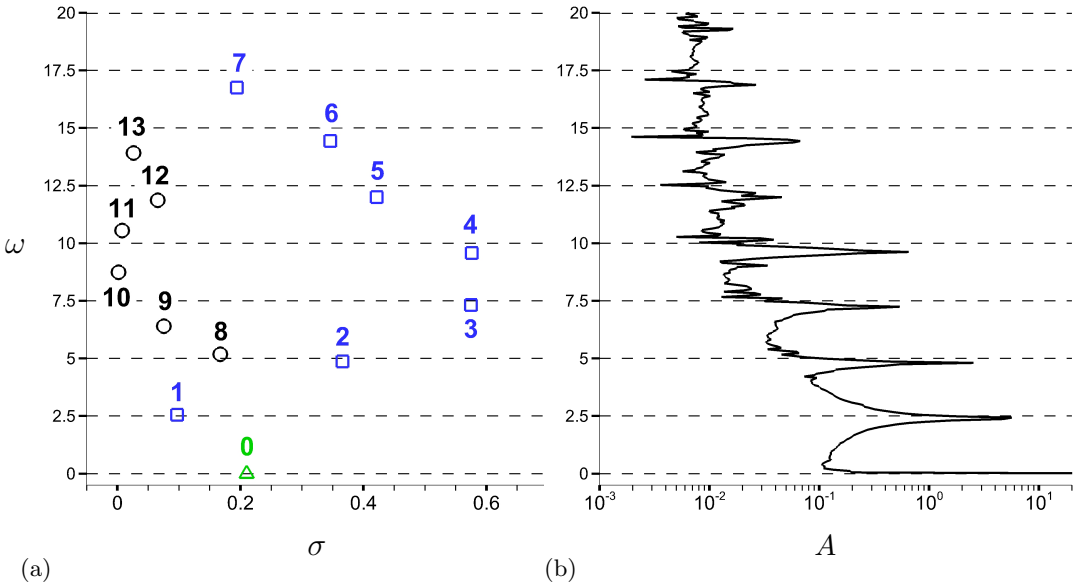

FIGURE 5.3: (a): Stability analysis spectrum, we observe an upper branch denoted with square symbols (□) and a lower branch denoted with circles (○). (b): Spectrum extracted from the unsteady simulation.

Comparing both stability and unsteady simulations spectra in Figs.5.3(a) and 5.3(b), we observe that both spectrum for modes $1-7$ overlap reasonably well in terms of frequency selection. We recover the fundamental mode (mode 1) which exhibits a frequency close to the natural flow frequency ($\omega = 2.4$), as well as several of its harmonics (modes $2-7$) with frequencies close to the unsteady signal. The fundamental mode is not the most amplified mode but is found to dominate the unsteady dynamics of the flow at large

times when integrating the unsteady equations. These results tend to suggest that the flow unsteadiness is linked to the unstable modes of the steady RANS equations.

	I_1	J_1	I_2	J_2	I_3	J_3	N
mesh 0	151	221	401	601	101	221	295000
mesh 1	101	221	151	301	61	121	64200
mesh 2	151	81	201	151	101	81	50000
mesh 3	301	121	401	301	201	121	180000
mesh 4	151	121	401	301	101	121	150000
mesh 5	151	221	201	601	101	221	175000

TABLE 5.4: Properties of the different configurations used for the analysis of the mesh discretization influence onto the spectrum.

5.2.2 Mesh discretization impact on the spectrum

The impact of the mesh discretization on the spectrum was investigated by considering the different configurations presented in table 5.4 where mesh 0 designates the mesh finally chosen. As our discretization step follows a tangential evolution, the impact of changing the number of discretization points is not trivial, but basically consists in adding or removing discretization points near the walls and in the mixing layer area. The spectrum convergence is studied using the adaptation of the elsA optimization code as presented in Section 3.2.5 for the $k-\omega$ model of Wilcox. The reason for this choice is that this analysis was performed at the beginning of this study when only this tool was available to perform stability analysis. The obtained spectra are depicted all together in Fig.5.4.

A first striking observation is that the frequency ω of the different modes is poorly affected by the mesh discretization while the growth rate σ is strongly impacted. Mesh 1 and 2 are poorly discretized and lead to very different growth rates for modes $5, 6, 7$ as well as spurious modes that disappear when refining the discretization. Mesh 3 and mesh 4 correspond to variations of mesh 1 where we increase the number of discretization points in x on the whole configuration for mesh 3 and only in bloc 2 for mesh 4. They both lead to identical spectra suggesting that the zone of interest for mesh refinement is located in bloc 2 where the mixing layer develops. Finally, mesh 5 was obtained by increasing the number of discretization points in y compared to mesh 1. It appears to have a strong impact on the modes growth rate suggesting that mesh $1-5$ lack points in the crosswise direction of the flow. We finally choice to use mesh 0 where the mixing layer is particularly well refined in bloc 2 for both x and y directions. Although the impact of the mesh discretization is not uniform on all the modes most eigenvalues are converged for mesh 0. We can notice some differences between mesh 0 and mesh 5 which

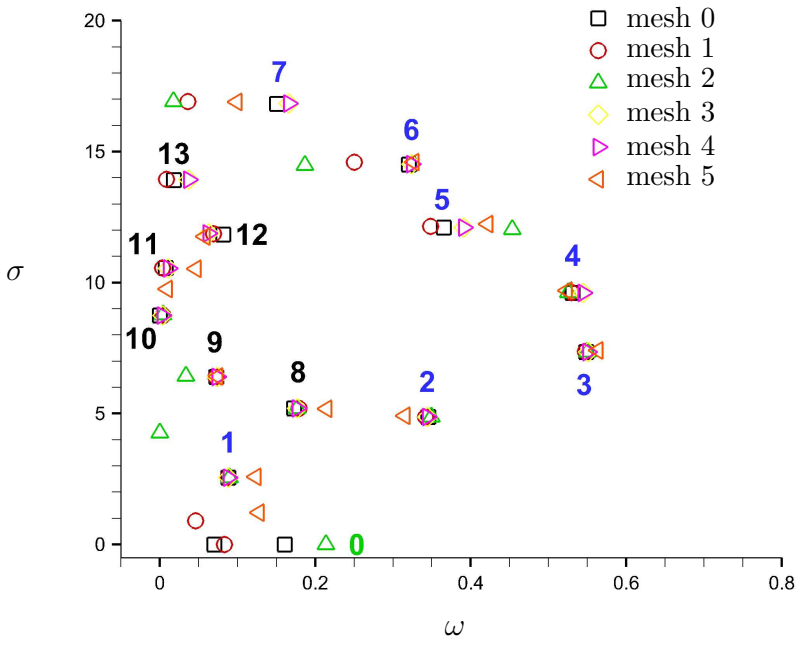

FIGURE 5.4: Variation of the spectrum with the different mesh presented in Table 5.4. The modified elsA optimization code is used with the $k-\omega$ model of Wilcox.

may be linked to the fact that the cells are strongly stretched in the x direction for mesh 5.

5.2.3 Unstable modes analysis

The upper branch of the spectrum in Fig.5.3(a) is composed of the fundamental mode (mode 1), which exhibits a frequency close to the natural flow frequency around 2000Hz ($\omega = 2.4$), as well as several of its harmonics (modes $2-7$). These modes correspond to dynamical modes linked to the aeroacoustic feedback mechanism proposed by Rossiter [111]. We depicted in Fig.5.5 the real part of the mode 1 spatial structure which dominates the flow dynamics at large times. Kelvin-Helmholtz instabilities grow from the upstream edge and propagate downstream. The turbulent fluctuations are located within the unstable Kelvin-Helmholtz like structures, with the downstream propagation of region of low and high values of turbulent kinetic energy (ρk) and dissipation rate ($\rho\omega$). Note that in order to give sense to the comparison of modes scales, all modes are phased at $(x = -1, y = 0)$ and normalized by setting the norm of their momentum equal to 1.

The upper branch modes structures also present acoustic resonance patterns. As we consider compressible equations, acoustic resonance may occur in the cavity as suggested by East [114]. The coupling between the aeroacoustic feedback and acoustic resonance mechanism was further characterized by Yamouni et al. [113]. They showed that the

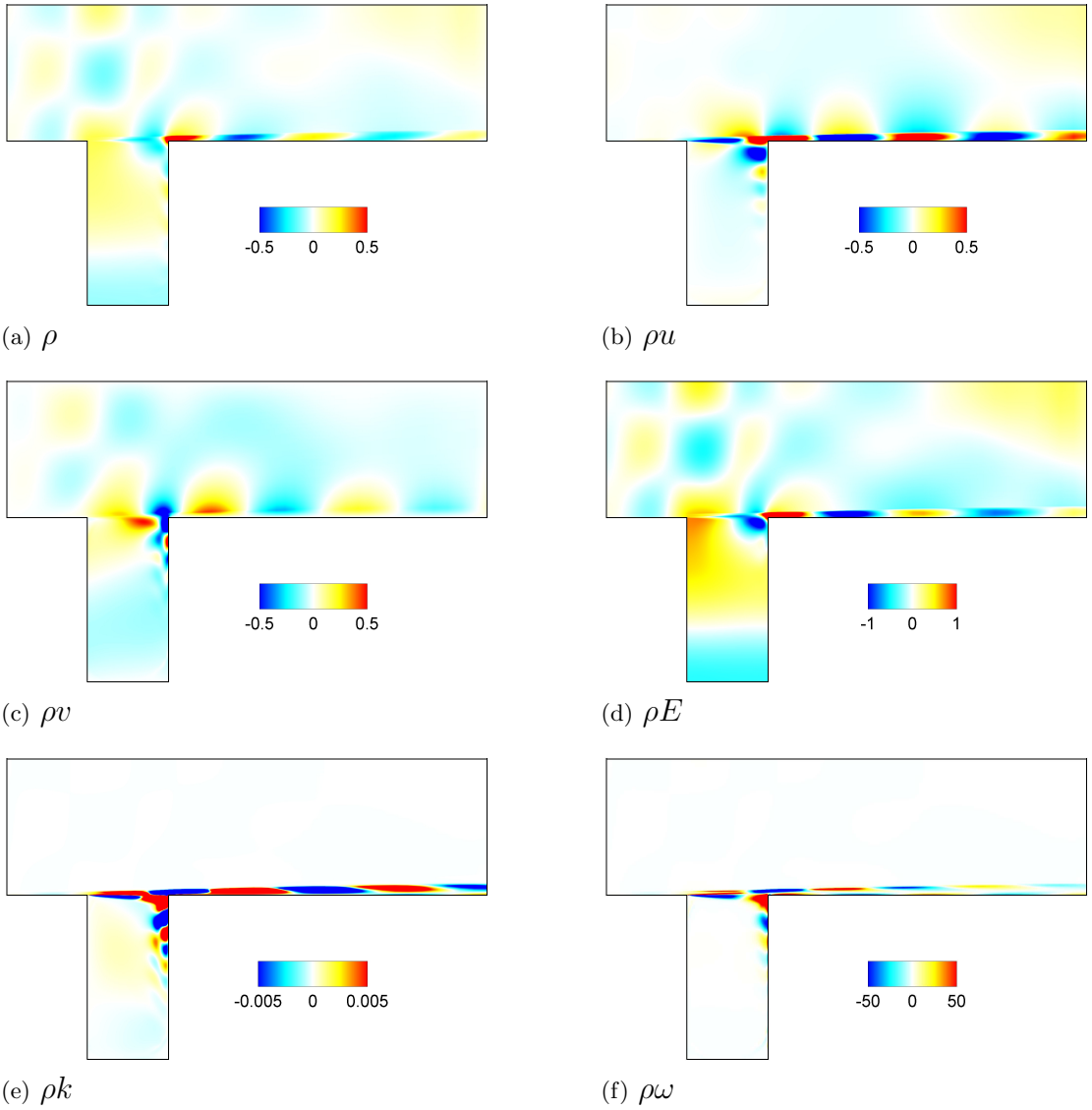

(a) ρ (b) ρu

(c) ρv (d) ρE

(e) ρk (f) $\rho \omega$

FIGURE 5.5: Spatial structure of the fundamental mode (mode 1) obtained with the $k-\omega$ model of Wilcox.

most unstable mode corresponds to an aeroacoustic mode for which acoustic resonance occurs.

The lower branch (modes $8-13$) of unstable eigenvalues in Fig.5.3(a) refers to unstable modes with smaller amplification rates and which exhibit strong patterns of acoustic resonance. As an example we compare in Fig.5.6 the spatial structure of the density of the fundamental mode and mode 10. We clearly see stronger resonance patterns compared to mode 1 (same scaling is used). These modes are likely to be acoustic resonance modes which became unstable under the excitation of Kelvin-Helmholtz instabilities.

Remark: The spatial structure of the unstable non-oscillating mode (mode 0, denoted

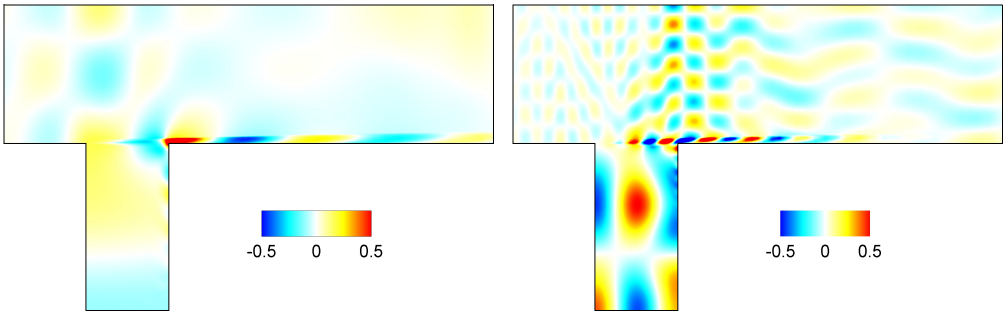

(a) mode 1 (b) mode 10

FIGURE 5.6: Comparison between the real part of the ρ component spatial structure of a Kelvin-Helmoltz mode (mode 1) and an acoustic mode (mode 10), same scaling is used in both figures.

with a triangle symbol ▽ in Fig.5.3(a)) differs from the other modes. It is not located near the mixing layer but near the upstream wall of the cavity around $(0, -0.4)$. As will be shown below, this mode is extremely sensitive to the numerical discretization and the turbulence modeling. These observations lead us to believe that it is a spurious mode.

5.2.4 Influence of the system of equations

The impact of the physical modeling is investigated using the Roe scheme with the baseflow obtained in Section 5.1.2. We plot in Fig.5.7 the spectrum computed with the $k-\omega$ and Spalart-Allmaras turbulence models, with uncoupled equations and with the modified elsA optimization code. Uncoupled equations correspond to the mean field equations in Eq. (3.13) for which the turbulent viscosity is frozen in the linearization process, so that turbulent fluctuations are not considered (see studies by Cossu et al. [23], Juan and Jiménez [58], Hwang and Cossu [60]).

A first interesting result is that the model choice (◇, ▽ and ○ in Fig.5.7) mainly affects the growth rate of the modes but not their frequency. This result is in agreement with Rossiter's mechanism where the frequency selection is only linked to the cavity width and Mach number. As for the amplification rate, we do observe some discrepancy between the intrusively modified elsA code (□) and our fully discrete method (◇) suggesting that the thin layer assumption may have some impact on the spectrum in this configuration.

The modelling does not have a strong impact on the modes although some tendency can be observed. Uncoupling the equations seems to increase most unstable modes growth rate suggesting that the discarded term representing eddy viscosity fluctuations μ_t' is likely to dissipate some energy. On the contrary, the Spalart-Allmaras modes seem to be more dissipative with smaller growth rates. The cavity modes $(8-13)$ are less affected by the physical modelling as they correspond to acoustic resonance mode that are more

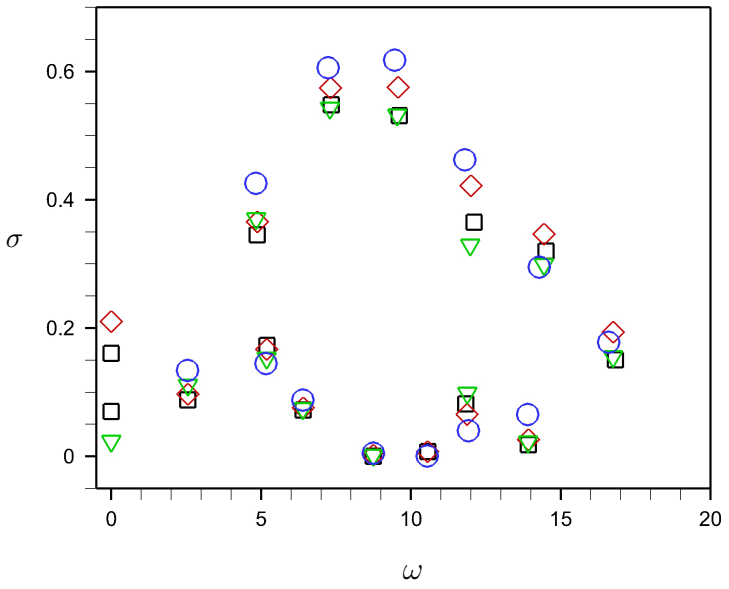

FIGURE 5.7: Impact of the physical modeling on the spectrum: □ elsA optimization code, ◇ $k-\omega$ model of Wilcox, ▽ Spalart-Allmaras model, ○ Uncoupled equations.

inviscid in nature.

The spatial structure of the Spalart-Allmaras fundamental mode is plotted in Fig.5.8. Comparing the mode structure with the one obtained using the $k-\omega$ Wilcox model in Fig.5.5, we observe strong similarities between both modes structures for the mean field variables. In order to compare the relative contributions of the different component fluctuations to the baseflow, we summarize in Table 5.5 for each conservative variable the ratio of the mode maximum value to the baseflow maximum value (here for mode 1). This ratio being defined up to an arbitrary amplitude, we rescale it by setting the variable ρ ratio to 1 for both modes.

Model	ρ	ρu	ρv	ρE	ρk	$\rho\omega$	$\rho\tilde{\nu}$	μ_t
Spalart-Allmaras	1	5	2	1	.	.	0.8	0.8
$k-\omega$	1	6	2	1	13	48	.	1.5

TABLE 5.5: Ratio for each conservative variable of the maximum value of mode 1 to the maximum value of the baseflow.

We observe that the turbulent fluctuations obtained using both turbulence models strongly impact the baseflow compared to the mean field variables, suggesting that the turbulent quantities do seem to play a role in the instability mechanism. Hence, assuming frozen eddy viscosity fluctuations does have an impact on the obtained flow

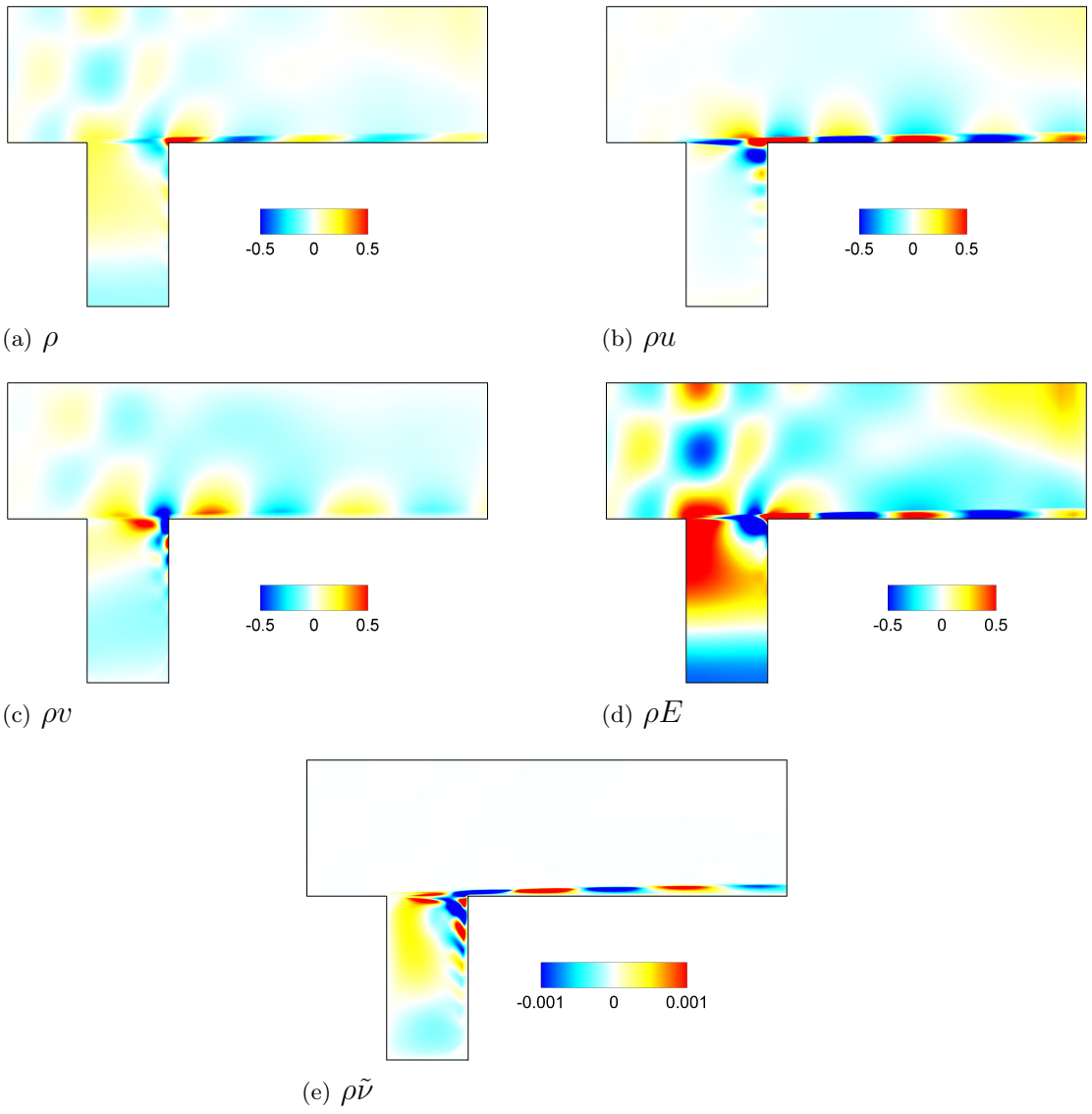

(a) ρ (b) ρu

(c) ρv (d) ρE

(e) $\rho\tilde{\nu}$

FIGURE 5.8: Spatial structure of the fundamental mode (mode 1) obtained with the Spalart-Allmaras turbulence model of Wilcox.

dynamics. In order to compare the impact of both turbulence models, we compute the eddy viscosity fluctuation μ_t' associated with the mode fluctuations. Denoting mode fluctuations with $'$ to distinguish them from baseflow quantities, the eddy viscosity fluctuation μ_t' associated to a given mode for the $k-\omega$ model of Wilcox is defined by:

$$\mu_t + \mu_t' = \frac{(\rho + \rho')\left(\rho k + (\rho k)'\right)}{\left(\rho\omega + (\rho\omega)'\right)}. \tag{5.1}$$

That is to the first order:

$$\mu_t' = \frac{\rho k}{\rho\omega}\rho' + \frac{\rho}{\rho\omega}(\rho k)' - \frac{\rho\rho k}{(\rho\omega)^2}(\rho\omega)'. \tag{5.2}$$

For the Spalart-Allmaras turbulence model we have:

$$\mu_t' = \mu\left(\frac{\mu_t}{\mu}\right)' + \frac{\mu_t}{\mu}\mu', \tag{5.3}$$

$$\left(\frac{\mu_t}{\mu}\right)' = \frac{4\chi^3\left(\chi^3 + C_{v1}^3\right) - 3\chi^6}{\left(\chi^3 + C_{v1}^3\right)^2}\chi', \tag{5.4}$$

$$\chi' = \frac{(\rho\tilde{\nu})'}{\mu} - \frac{\rho\tilde{\nu}}{\mu^2}\mu', \tag{5.5}$$

$$\tag{5.6}$$

$$\mu' = \frac{\mu_s}{\sqrt{T_s}}\frac{1 + C_s/T_s}{1 + C_s/T}\left[\frac{1}{2\sqrt{T}} + \frac{\sqrt{T}C_s}{T^2\left(1 + C_s/T\right)}\right]T', \tag{5.7}$$

$$\begin{aligned} T' &= -\frac{T}{\rho}\rho' + \frac{\gamma - 1}{\rho R}(\rho E)' \\ &+ \frac{\gamma - 1}{\rho R}\left[-\frac{\rho u}{\rho}(\rho u)' + 0.5\frac{(\rho u)^2}{\rho^2}\rho' - \frac{\rho v}{\rho}(\rho v)' + 0.5\frac{(\rho v)^2}{\rho^2}\rho'\right]. \end{aligned} \tag{5.8}$$

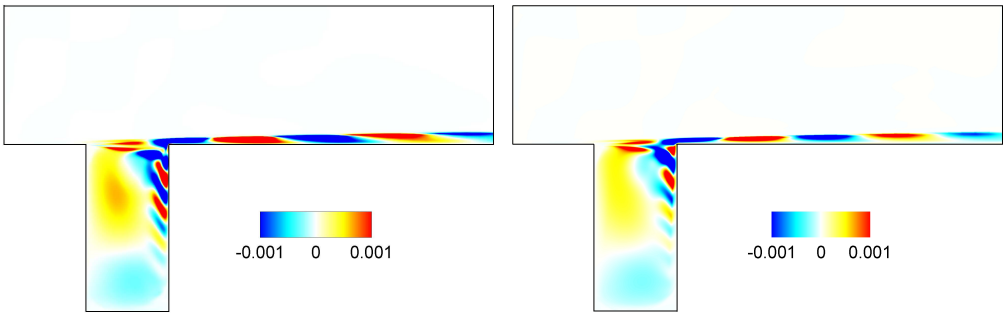

(a) $k - \omega$ model of Wilcox (b) Splalart-Allmaras model

FIGURE 5.9: Eddy viscosity fluctuation μ_t' induced by mode 1 using both turbulence model.

We can observe in Fig.5.9 that both turbulence models lead to very similar fluctuation fields μ_t' in terms of structure and order of magnitude. The eddy viscosity fluctuations are mainly located in the path of the unstable modes.

Finally, the impact of the numerical scheme was investigated for both turbulence models using the different schemes presented in Section 3.3.4. Results obtained are depicted in Figs.5.10(a) for the $k - \omega$ model of Wilcox and 5.10(b) the Spalart-Allmaras model. As expected, the spectrum is poorly affected by the choice of numerical discretization, especially for the Kelvin-Helmholtz branch $(1 - 7)$.

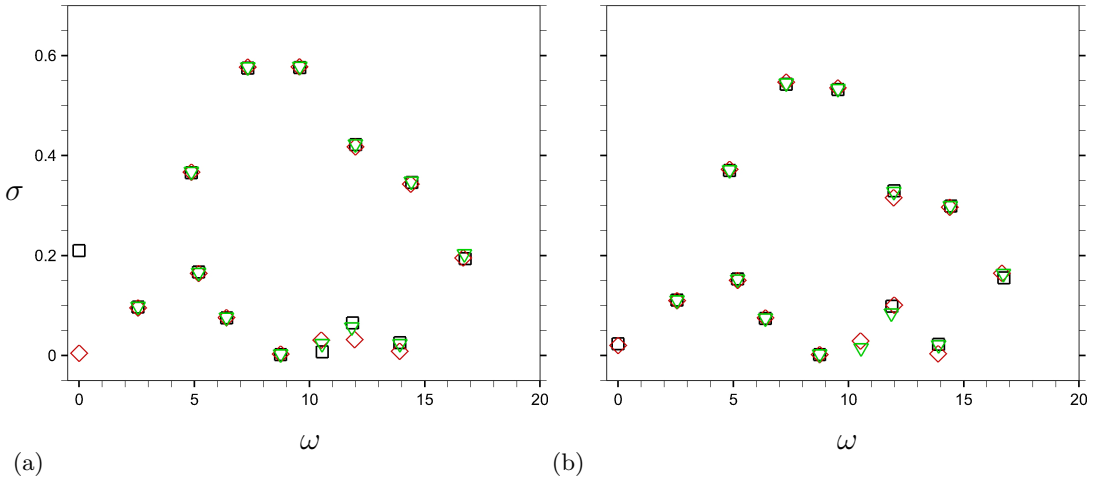

FIGURE 5.10: Influence of the discretization scheme on the spectrum, □ Roe scheme, ◇ Jameson scheme, ▽ AUMS scheme. (a): $k-\omega$ model of Wilcox. (b): Splalart-Allmaras model.

5.2.5 Spectrum convergence with the linearization parameter

As stated in Section 3.2.4, the linearization parameter ϵ_m should be chosen carefully. In order to check the convergence of the method with ϵ_m, we extracted the set of eigenvalues λ_{ϵ_m} for Jacobian matrices computed with various values of ϵ_m. The spectrum is found converged for $\epsilon_m < 10^{-5}$, we thus use as a reference the set of eigenvalues λ_0 obtained using the optimal $\epsilon_m = 5.10^{-6}$. We then compute the relative error $err = |\lambda_{\epsilon_m} - \lambda_0| \,/\, |\lambda_0|$ as a function of the different ϵ_m used. We plot in Figs.5.11(a) and 5.11(b) the base 10 logarithm of the relative error for the dynamical branch eigenvalues (modes $1-7$) and interpolate the different sets with linear fits. Note that the curves were arbitrarily shifted from each other to ease visualization.

The slopes a obtained with the linear fit evaluation as well as the regression parameter R^2 are summarized in Table 5.6 for the different modes and both turbulence models. We observe a strong convergence of the method for the $k-\omega$ model of Wilcox with a slope coefficient of 2 for nearly all the modes, the convergence coefficients for the Spalart-Allmaras modes being lower but close to 2.

Mode number	1		2		3		4		5		6		7	
Parameters	a	R^2	a	R^2	a	R^2	a	R^2	a	R^2	a	R^2	a	R^2
Spalart-Allmaras	1.8	0.99	2.0	0.99	2.1	0.99	2.0	0.99	1.9	0.99	1.7	0.99	1.6	0.98
$k-\omega$	2.00	0.99	1.97	0.99	1.99	0.99	1.99	0.99	1.97	0.99	2.00	0.99	2.02	0.99

TABLE 5.6: Linear fit parameters of the eigenvalues convergence with ϵ_m.

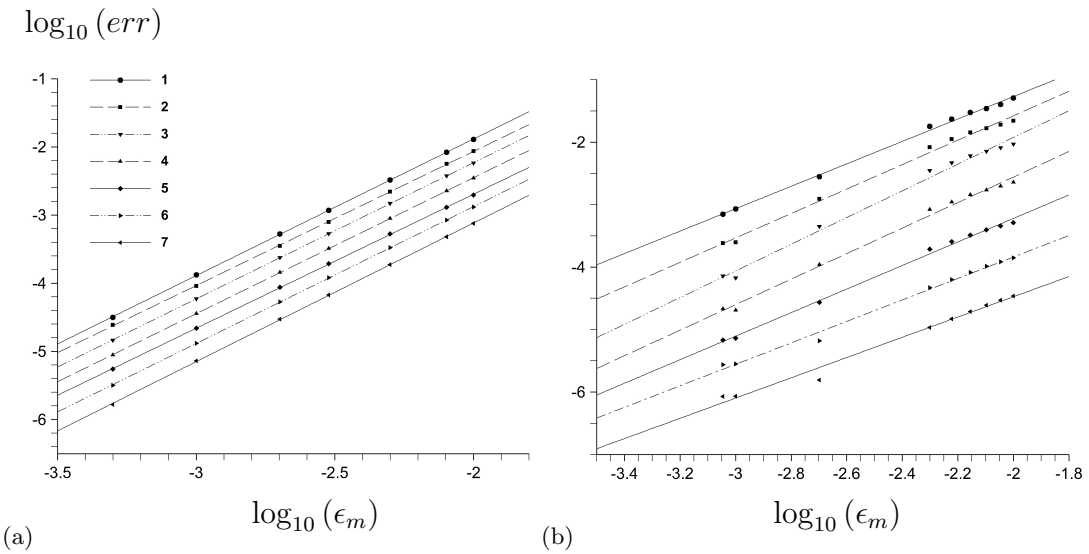

FIGURE 5.11: Convergence with ϵ_m of the upper branch unstable eigenvalues $(1-7)$ for both turbulence models. (a): $k-\omega$ model of Wilcox. (b): Spalart-Allmaras model.

5.2.6 Adjoint modes

As detailed in Section 2.2.2, the resolution of the adjoint problem in Eq. (2.10) is necessary to evaluate the sensitivity gradients. We use the discrete inner-product defined such that :

$$\forall\,(\mathbf{u},\mathbf{v}) \qquad <\mathbf{u},\mathbf{v}>=\sum_{i,j} u_i^* v_i \Omega_{ij} = \mathbf{u}^*\mathbf{Q}\mathbf{v}, \tag{5.9}$$

where $\mathbf{Q}$ is a diagonal matrix whose terms correspond to the surface of the mesh cells. The spatial structure of the fundamental adjoint mode $\tilde{\mathbf{w}}|_{\mathbf{Q}}$ for the $k-\omega$ model of Wilcox is plotted in Fig.5.12.

Note that the adjoint mode is normalized according to Eq. (2.10). As for the direct modes, turbulent scales and mean field quantities present similar structures. Adjoint modes are mostly located upstream the leading edge of the cavity: direct modes propagate downstream while adjoint modes propagate upstream, which comes from the opposite transport of the perturbations by the baseflow in the direct and adjoint linear operators (Sipp and Lebedev [68]). The structure of the adjoint modes obtained with the Spalart-Allmaras model are similar to those obtained with the $k-\omega$ model of Wilcox.

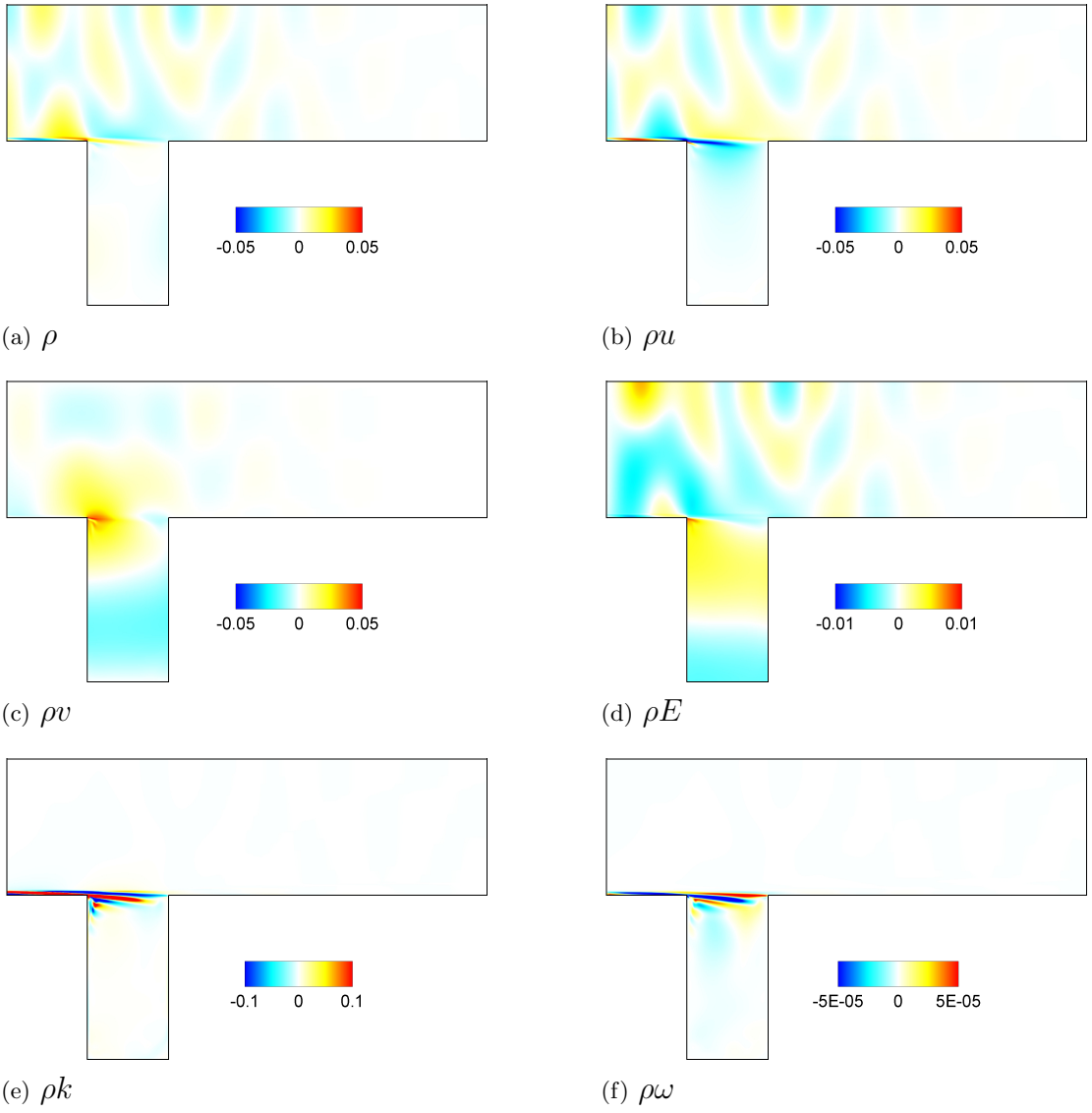

(a) ρ (b) ρu

(c) ρv (d) ρE

(e) ρk (f) $\rho \omega$

FIGURE 5.12: Real part of the spatial structure of the adjoint mode 1 obtained with the $k-\omega$ model of Wilcox.

5.3 Sensitivity analysis

5.3.1 Sensitivity gradient to baseflow perturbations $\nabla_{\mathbf{w_b}}\lambda$

Once both direct and adjoint modes are available, we compute the sensitivity gradient to baseflow perturbations $\nabla_{\mathbf{w_b}}\lambda|_{\mathbf{Q}}$ as presented in Section 2.2.2. As stated by Marquet et al. [32], the sensitivity analysis to baseflow modifications is appropriate to determine which regions of the baseflow participate to the development of the instabilities. The gradient $\nabla_{\mathbf{w_b}}\lambda|_{\mathbf{Q}}$ is a complex vector field, its real part corresponds to the sensitivity of the growth rate to baseflow perturbation $\nabla_{\mathbf{w_b}}\sigma|_{\mathbf{Q}}$ while its imaginary part refers to the sensitivity of the mode frequency to baseflow perturbation $\nabla_{\mathbf{w_b}}\omega|_{\mathbf{Q}}$.

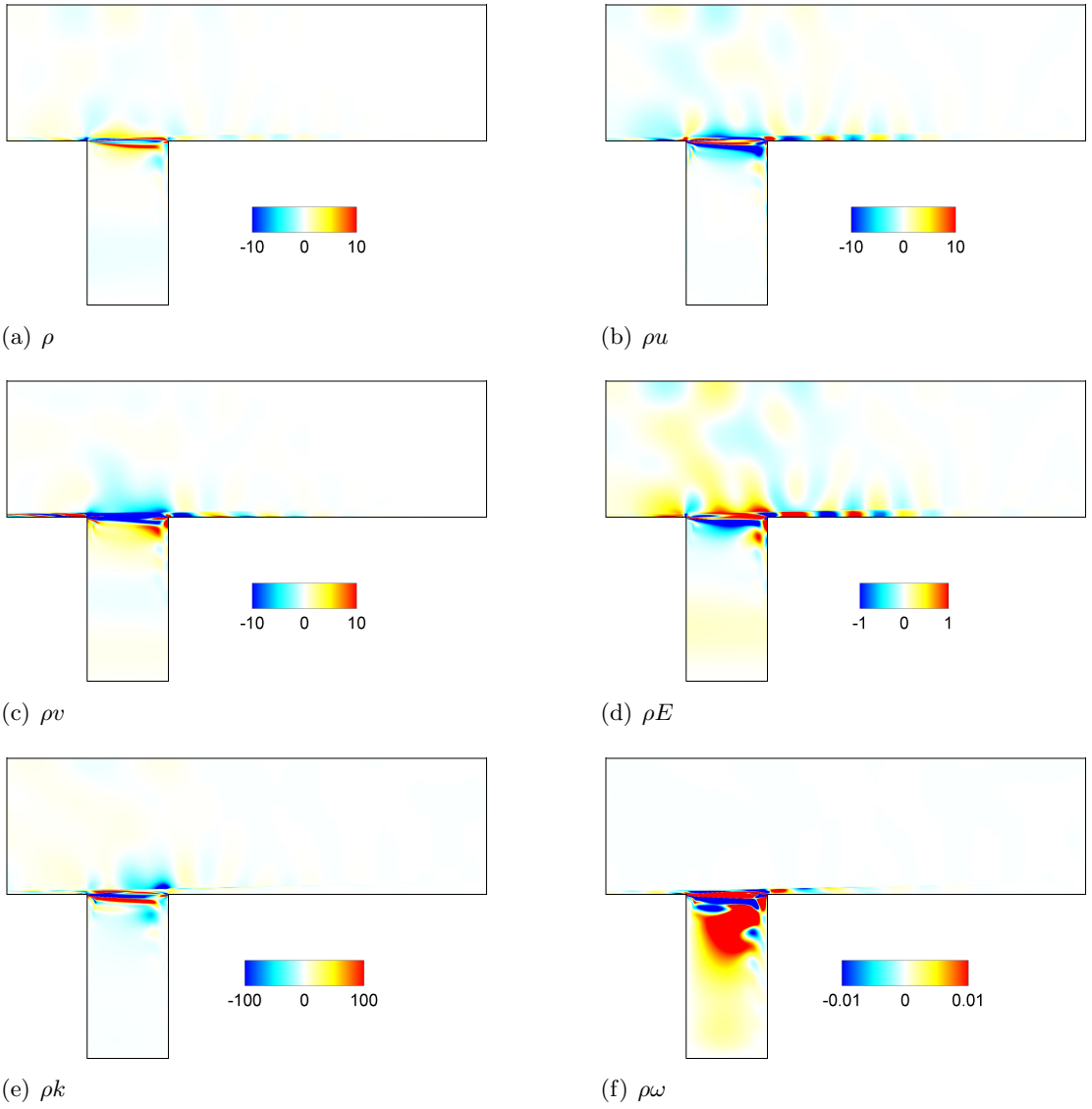

(a) ρ (b) ρu

(c) ρv (d) ρE

(e) ρk (f) $\rho \omega$

FIGURE 5.13: Growth rate sensitivity to baseflow perturbations $\boldsymbol{\nabla}_{\mathbf{w_b}}\sigma|_{\mathbf{Q}}$ of mode 1 obtained with the $k-\omega$ model of Wilcox.

We depicted the gradient $\boldsymbol{\nabla}_{\mathbf{w_b}}\sigma|_{\mathbf{Q}}$ in Fig.5.13 for mode 1 obtained with the $k-\omega$ model of Wilcox and the Roe scheme. We observe that the eigenvalue is mostly sensitive to perturbations of the baseflow in the mixing layer area which corresponds to the region where Kelvin-Helmholtz instabilities are active. We should also mention that the gradient $\boldsymbol{\nabla}_{\mathbf{w_b}}\omega|_{\mathbf{Q}}$ has a similar structure in terms of location as the sensitivity of the growth rate.

From a physical point of view, the gradient $\boldsymbol{\nabla}_{\mathbf{w_b}}\lambda$ corresponds to the baseflow perturbation that yields the strongest eigenvalue variation [32]. From a numerical point of view, it indicates which areas of the baseflow shall be well captured by the mesh discretization in order to accurately compute the eigenvalues.

5.3.2 Validation of the gradient $\boldsymbol{\nabla}_{\mathbf{w_b}}\lambda$

In order to validate our gradients, we first compare the results obtained in the fully discrete approach with those obtained with the modified elsA code using the method presented in Section 3.2.5. Both methods lead to similar gradient fields but with slightly different amplitudes suggesting the equivalence of both methods. As an example, we plot in Figs.5.14(a) and 5.14(b) the ρk component of $\boldsymbol{\nabla}_{\mathbf{w_b}}\sigma|_{\mathbf{Q}}$ obtained using both methods.

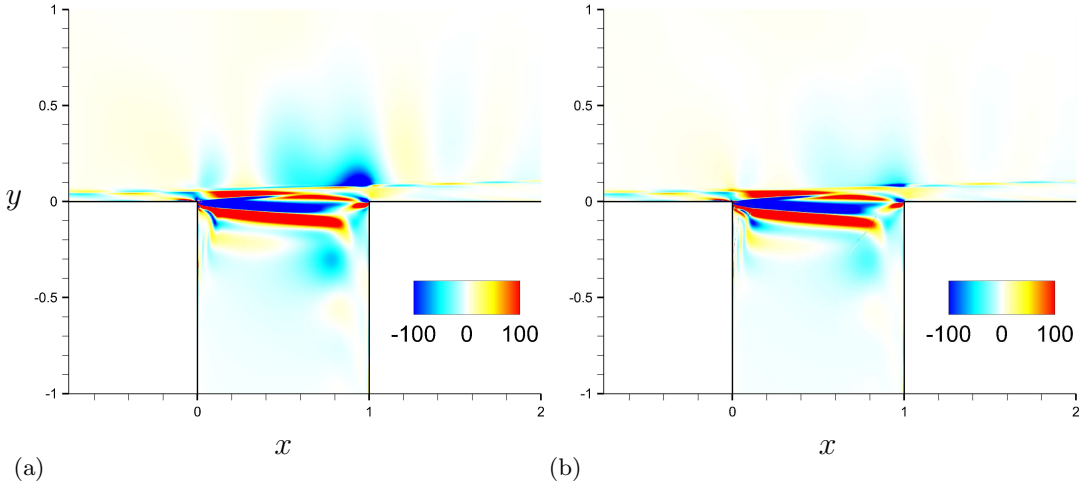

FIGURE 5.14: Comparison of the ρk component of the growth rate sensitivity to baseflow perturbations $\boldsymbol{\nabla}_{\mathbf{w_b}}\sigma|_{\mathbf{Q}}$ obtained with our fully discrete method (a), and the modified elsA code (b). The $k-\omega$ model of Wilcox is used.

The validity of the gradient is then further tested by comparing for a given direction $\mathbf{w_1}$, the eigenvalue variation predicted by our gradient $\delta\lambda = \langle\boldsymbol{\nabla}_{\mathbf{w_b}}\lambda,\beta\mathbf{w_1}\rangle$, to the eigenvalue variation obtained with a finite difference method, $\delta\lambda_1 = [\lambda(\mathbf{w_b}+\beta\mathbf{w_1}) - \lambda(\mathbf{w_b})]$ (where β is a small parameter to remain in the linear domain). The Jacobian matrices $\mathbf{J}|_{\mathbf{w_b}+\beta\mathbf{w_1}}$ and $\mathbf{J}|_{\mathbf{w_b}}$ are extracted and their spectrum computed, leading to the discrete evaluation of $\delta\lambda_1$.

Note that the discrete evaluation of $\delta\lambda_1$ is a complex issue in itself: the baseflow perturbation $\beta\mathbf{w_1}$ shall be small compared to the baseflow $\mathbf{w_b}$ although its various components may scale differently from one another. In order to ease the computation of $\delta\lambda_1$, we can use the fact that by linearity the full perturbation effect of $\beta\mathbf{w_1}$ can be computed from the contributions of its various components separately. Indeed, if $\mathbf{w_1} = \boldsymbol{\rho_1} + \boldsymbol{\rho U_1} + \boldsymbol{\rho V_1} + \boldsymbol{\rho E_1} + \boldsymbol{\rho k_1} + \boldsymbol{\rho\omega_1}$, where $\mathbf{x_1}$ corresponds to a perturbation vector where only the conservative variable x_1 is perturbed, we have by linearity (using

the $k-\omega$ model for example):

$$\begin{aligned}
\delta\lambda_1 &= \langle \boldsymbol{\nabla}_{\mathbf{w_b}}\lambda, \beta\mathbf{w_1}\rangle\,, && (5.10)\\
&= \beta(\,\langle \boldsymbol{\nabla}_{\mathbf{w_b}}\lambda, \boldsymbol{\rho_1}\rangle + \langle \boldsymbol{\nabla}_{\mathbf{w_b}}\lambda, \boldsymbol{\rho U_1}\rangle + \langle \boldsymbol{\nabla}_{\mathbf{w_b}}\lambda, \boldsymbol{\rho V_1}\rangle && (5.11)\\
&+ \langle \boldsymbol{\nabla}_{\mathbf{w_b}}\lambda, \boldsymbol{\rho E_1}\rangle + \langle \boldsymbol{\nabla}_{\mathbf{w_b}}\lambda, \boldsymbol{\rho k_1}\rangle + \langle \boldsymbol{\nabla}_{\mathbf{w_b}}\lambda, \boldsymbol{\rho\omega_1}\rangle\,),\\
&= \beta\left(\delta\lambda_{1,\rho} + \delta\lambda_{1,\rho U} + \delta\lambda_{1,\rho V} + \delta\lambda_{1,\rho E} + \delta\lambda_{1,\rho k} + \delta\lambda_{1,\rho\omega}\right). && (5.12)
\end{aligned}$$

We thus impose a perturbation on the ρ component for example $\boldsymbol{\rho_1}$, compute the associated Jacobian matrix $\mathbf{J}|_{\mathbf{w_b}+\beta\boldsymbol{\rho_1}}$ and the corresponding new eigenvalue $\lambda_{\mathbf{w_b}+\beta\boldsymbol{\rho_1}}$. The discrete eigenvalue variation $\delta\lambda_{1,\rho} = \dfrac{1}{\beta}\left(\lambda_{\mathbf{w_b}+\beta\boldsymbol{\rho_1}} - \lambda_{\mathbf{w_b}}\right)$ can then be evaluated and compared to the one obtained with our gradient $\delta\lambda_\rho = \langle \boldsymbol{\nabla}_{\mathbf{w_b}}\lambda, \boldsymbol{\rho_1}\rangle$. We can thus validate our gradient component by component.

We chose $\mathbf{w_1} = \mathbf{w_b}$ along with a small value for β and restricted $\mathbf{w_1}$ to each conservative variable independently as previously stated. As a consequence, we perturb independently each quantity (ρ, ρU ...) of the baseflow ($\mathbf{w_b} + \beta\mathbf{w_1}$) on the full domain.

We summarized in Table 5.7 the relative difference $\dfrac{|\delta\lambda_{1,x} - \delta\lambda_x|}{|\delta\lambda_x|}$ between both eigenvalue variation prediction for each conservative variable perturbations x. We observe that the gradient is correctly evaluated up to within 3% for the Spalart-Allmaras model and 0.4% for the $k-\omega$ model for each perturbation vector. Once again, the method seems to give better results using the $k-\omega$ model of Wilcox.

$\mathbf{w_1}$	ρ	ρu	ρv	ρE	ρk	$\rho\omega$	$\rho\tilde{\nu}$
Spalart-Allmaras	0.01	0.001	0.02	0.01	.	.	0.03
$k-\omega$	0.003	0.001	0.004	0.002	0.0004	0.002	.

TABLE 5.7: Relative difference between eigenvalue variation predicted with the sensitivity gradient and a discrete evaluation. The evaluation is performed on each component of the gradient independently.

This validation process also enables us to determine accurately the best set of ϵ_2 values in Eqs. (3.9) and (3.12). The perturbation parameter was fixed with $\epsilon_2 = \epsilon_{m_2}\,(|w|+1)$ where $|w|$ is the local baseflow value. The best set of ϵ_{m_2} is obtained using different values of ϵ_{m_2} adapted to each conservative variable: these values are summarized in Table 5.8.

Model	ρ	ρu	ρv	ρE	ρk	$\rho\omega$	$\rho\tilde{\nu}$
Spalart-Allmaras	10^{-4}	10^{-4}	10^{-5}	10^{-3}	.	.	10^{-6}
$k-\omega$	10^{-5}	10^{-5}	10^{-5}	10^{-3}	10^{-6}	10^{-4}	.

TABLE 5.8: Linearization parameter ϵ_{m_2} used for the computation of the sensitivity gradient to baseflow perturbations $\boldsymbol{\nabla}_{\mathbf{w_b}}\lambda$.

The sensitivity gradient $\boldsymbol{\nabla}_{\mathbf{w_b}}\lambda$ indicates where and how a baseflow perturbation would affect the unstable eigenvalues and consists in a first step in view of steady control. The question is then how to generate this baseflow perturbation with a meaningful control device, which we consider here as a steady volumic source term in the governing equations. It is thus of interest to consider the sensitivity gradient to a steady force $\boldsymbol{\nabla}_{\mathbf{f}}\lambda$.

5.3.3 Steady control

Sensitivity gradient of the unstable eigenvalue to a steady force $\boldsymbol{\nabla}_{\mathbf{f}}\lambda$ is readily obtained from the sensitivity gradient to baseflow perturbations $\boldsymbol{\nabla}_{\mathbf{w_b}}\lambda$ through Eq. (2.21). This gradient indicates locations in the flow were a steady force $\boldsymbol{\delta}\mathbf{f}$ could lead to stabilization/destabilization of the unstable modes [32].

Rather than looking at the gradient fields $\boldsymbol{\nabla}_{\mathbf{f}}\lambda|_{\mathbf{Q}}$, we propose to consider the impact of an infinitesimal control cylinder located at (x,y) on the eigenvalue variation $\delta\lambda$ using Eq. (2.21). Similarly to Marquet et al. [32], the local force $\boldsymbol{f}_{xy}$ that the cylinder exerts on the fluid is taken as a first approximation as proportional and opposite to the drag experienced by the cylinder placed in the baseflow:

$$\mathbf{f}_{xy} \propto -\mathbf{U}_{xy}/\Omega_{xy} \tag{5.13}$$

where Ω_{xy} corresponds to the volume of the cell located at (x,y). The choice of such a simple model to represent the effort of the control cylinder is motivated by the fact that we are mainly interested in the direction of the eigenvalue variation (stabilization or destabilization). More sophisticated models can be found in (Marquet et al. [32], Meliga et al. [66]).

Computing this force for each cell location in our mesh, we obtain the eigenvalue variation field $\delta\lambda_{xy}$ which indicates how the eigenvalue is impacted by the presence of an infinitely small control cylinder located at (x,y). The real part of $\delta\lambda_{xy}$ corresponds to the growth rate variation $\delta\sigma_{xy}$ of the mode while its imaginary part refers to its frequency change $\delta\omega_{xy}$. In particular, negative values of $\delta\sigma_{xy}$ indicate that the mode growth rate is decreased when the cylinder is located at (x,y), which thus induces a stabilizing effect. On the opposite, if $\delta\sigma_{xy}$ is positive then the cylinder destabilizes the mode and no control effect shall be observed.

We plot in Fig.5.15 the field $\delta\sigma_{xy}$ for the different turbulence models that were studied (the maximum value was set to 1 in each Figure). We observe that the control maps slightly differ from one modeling to another. In all cases, we recover a stabilization

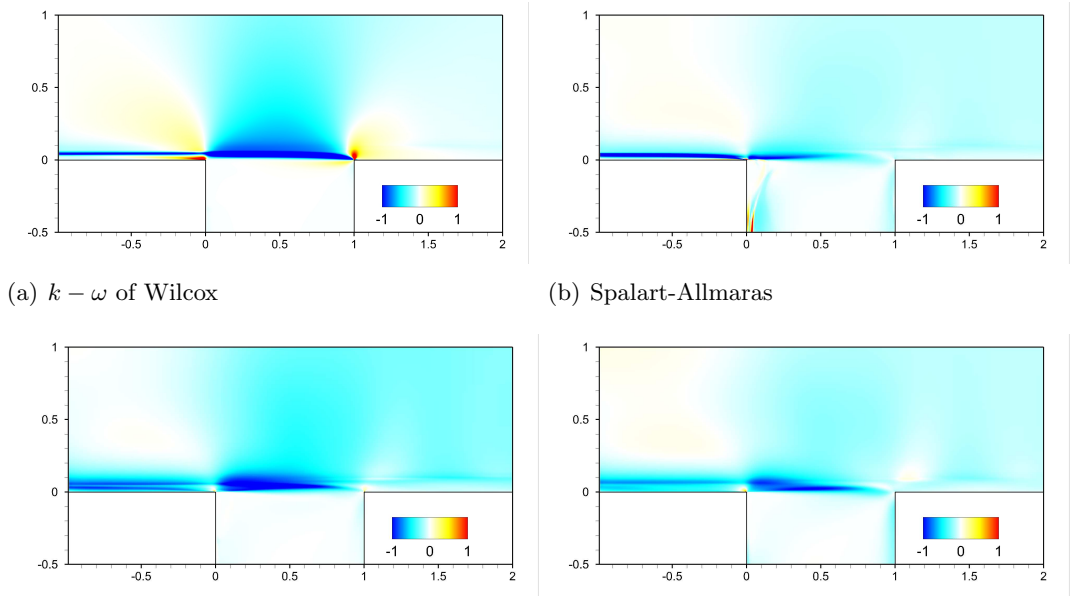

(a) $k-\omega$ of Wilcox

(b) Spalart-Allmaras

(c) elsA optimization code

(d) Frozen eddy viscosity

FIGURE 5.15: Variation of the eigenvalue growth rate $\delta\sigma_{xy}/\|\lambda\|$ due to the presence of a control cylinder at (x,y) (mode 1). Blue regions indicate that the amplification rate is lowered while increased in the red regions.

region in blue near $y = 0.05$ that extends upstream and downstream of the leading edge of the cavity. We shall mention that for all models, stabilizing regions $\delta\sigma_{xy} < 0$ also correspond to region where the presence of the cylinder induces an increase of the mode frequency $\delta\omega_{xy} > 0$. These results are in agreement with the experimental study by Illy et al. [109] whom configuration was similar. They controlled the flow using a small steady cylinder located at the station $(-0.1, y)$ with $0 \leq y \leq 0.22$. They found a critical region $0.05 < y < 0.12$ in which the cylinder had to be placed to control the flow unsteadiness. A small destabilizing region is also obtained just upstream the leading edge of the cavity. We observe small differences between the elsA optimization code results and our fully discrete approach (Figs.5.15(a) & 5.15(c)) which are probably linked to the approximations done in the linearization of the optimization code.

Finally, we depicted in Fig.5.16 the control map experimentally obtained by Sami Yamouni [110] for a similar configuration where the flow was controlled using a small cylinder. A pressure sensor was placed at the downstream edge of the cavity enabling the computation of the controlled flow spectrum. The impact of the cylinder is measured by integrating the spectrum and subtracting it to the natural case. Blue regions in Fig.5.16 correspond to areas where the control cylinder significantly lower the noise emission of the natural flow, while red regions correspond to areas where the cylinder poorly affect the natural case. We observe similar tendencies with the control maps presented in Figs.5.15, with a stabilizing region near the upstream corner of the cavity that

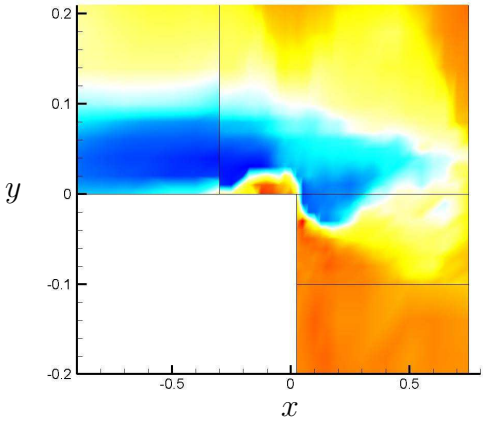

FIGURE 5.16: Control map experimentally obtained by Sami Yamouni [110] with a small control cylinder. Blue regions indicate areas where the control cylinder significantly lower the noise emission of the natural flow, while red regions correspond to areas where the control device poorly affect the natural flow.

extends far upstream. Our results are thus in relatively good agreement with the experimental datas and suggest that sensitivity analysis does provide interesting information regarding steady control of turbulent flows.

5.4 Detailed analysis of the Spalart-Allmaras model

Comparing the numerical tests performed on both turbulence models, the Spalart-Allmaras appeared to have poorer features then the $k-\omega$ model. Indeed, both spectrum convergence with ϵ in Fig.5.11(b) and gradient validation in Table 5.7 are slightly stronger when using the $k-\omega$ model. These observations lead us to further investigate the results obtained with the Spalart-Allmaras model.

5.4.0.1 Discontinuities in the gradient

The streamwise component of the growth rate sensitivity to baseflow perturbations $\boldsymbol{\nabla}_{\mathbf{w_b}}\sigma|_{\mathbf{Q}}$ is depicted in Fig.5.17(a). We clearly observe the appearance of several discontinuities in three different areas A, B, C of the field, these discontinuities being present in all the other components of the gradient. These results suggest that the linearization of the Spalart-Allmaras turbulence model is more difficult then expected. Surprisingly enough, these discontinuities do not seem to strongly affect the gradient validation and vanish when computing the sensitivity gradient to a steady force $\boldsymbol{\nabla}_{\mathbf{f}}\lambda$. However, as such discontinuities remain problematic, we chose to have a deeper insight into this turbulence model in order to identify the source(s) of these discontinuities.

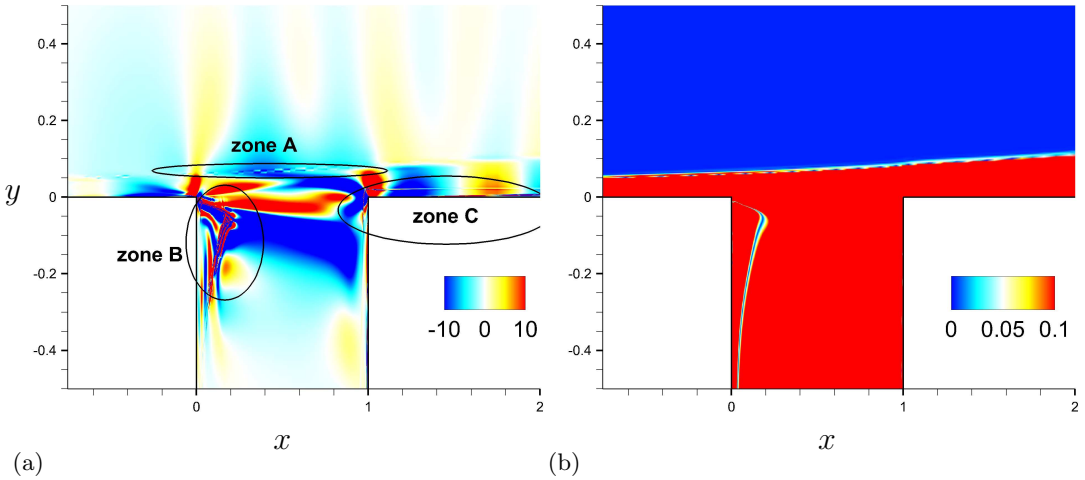

(a) (b)

FIGURE 5.17: (a): Streamwise component of the growth rate sensitivity to baseflow perturbations $\nabla_{\mathbf{w_b}}\sigma|_{\mathbf{Q}}$ computed using the Spalart-Allmaras turbulence model. Three regions of discontinuities are identified. (b): Saturated levels on the vorticity modulus $|\Omega|$ of the baseflow. We clearly observe a correlation between the discontinuities in zone A and B and the 0 values of the vorticity.

5.4.0.2 Numerical origin

In a first hand, a closer look to the definition of $\tilde{S} = |\Omega| + \frac{\tilde{\nu}}{K^2\eta^2} f_{v2}$ in Section 3.3.3 reveals that the modulus of the vorticity $|\Omega|$ is not a continuously differentiable term near 0. Note that $\tilde{S}$ intervenes in the computation of both the production and destruction source terms of the model. The saturated level of the vorticity module of the baseflow $\mathbf{w_b}$ are depicted in Fig.5.17(b), where we clearly notice a correlation between the discontinuities observed in the gradient in Fig.5.17(a) and the zone were the vorticity modulus is close to 0.

A simple way to adapt the code into a continuously differentiable manner is to replace the vorticity modulus $|\Omega|$ with $\sqrt{\Omega^2 + M^2} - M$ where M is a small constant. For $M = 0$, we recover the initial formulation while for $M \neq 0$ this adaptation only impacts the areas where $|\Omega| \approx M$. We plotted in Fig.5.18(a) the new gradient field obtained for $M = 0.1$. The discontinuities in zone A have disappeared and the discontinuities in zone B are strongly damped while zone C remains unaffected.

We shall mention that we found several limiters implemented in the elsA code for the source terms of the model which may lead to non-differentiable equations:

- the cross diffusion term is bounded by the production term with

$$Cross = min\,(Cross, 20Prod),$$

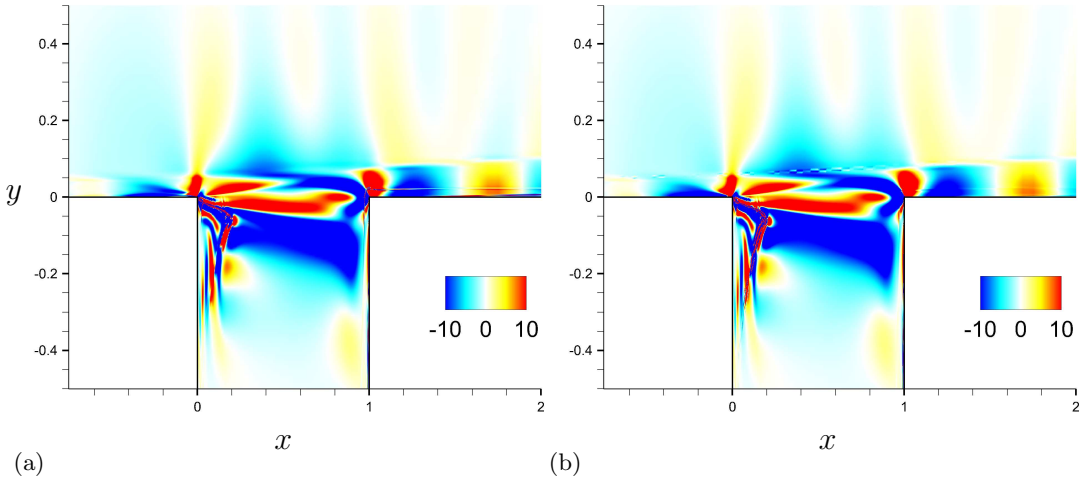

FIGURE 5.18: Streamwise component of the growth rate sensitivity to baseflow perturbations $\nabla_{\mathbf{w_b}}\sigma|_{\mathbf{Q}}$ computed with a modified Spalart-Allmaras turbulence model. (a): the constant $M = 0.1$ is used for the computation of $\tilde{S}$. (b): The term f_w is frozen in the residual evaluation.

- during the destruction term computation, the computation of the quantity $\tilde{r}$ is limited with

$$\tilde{r} = max\left[0, min\left(10, \frac{1}{max\left(\tilde{S}, 10^{-15}\right)} \frac{\rho\tilde{\nu}}{\rho} \frac{1}{\kappa^2\eta^2}\right)\right].$$

Although these limiters are not responsible for the discontinuities observed in our case, their presence in CFD code (generally for numerical convergence) may limit the black box use of our fully discrete method.

The zone C discontinuities were found to arise from the linearization of the term f_w in the destruction term (see Section 3.3.3 for a complete definition). This function seems extremely hard to linearize to the second order using finite differences. Hoping that this term would not have a strong contribution to the final gradient, we computed the gradient by freezing this function in the residual evaluation of the gradient, using the f_w function computed from the baseflow. The new gradient field is depicted in Fig.5.18(b) were discontinuities in zone C have vanished. The gradient does not seem to be strongly affected by this modification.

5.4.0.3 Corrected gradient

The previous remarks lead us to recompute the gradients. The constant $M = 0.1$ was used for the Jacobian matrix computation as the zero vorticity lines are clearly responsible for discontinuities while linearizing the turbulence model. Both direct and

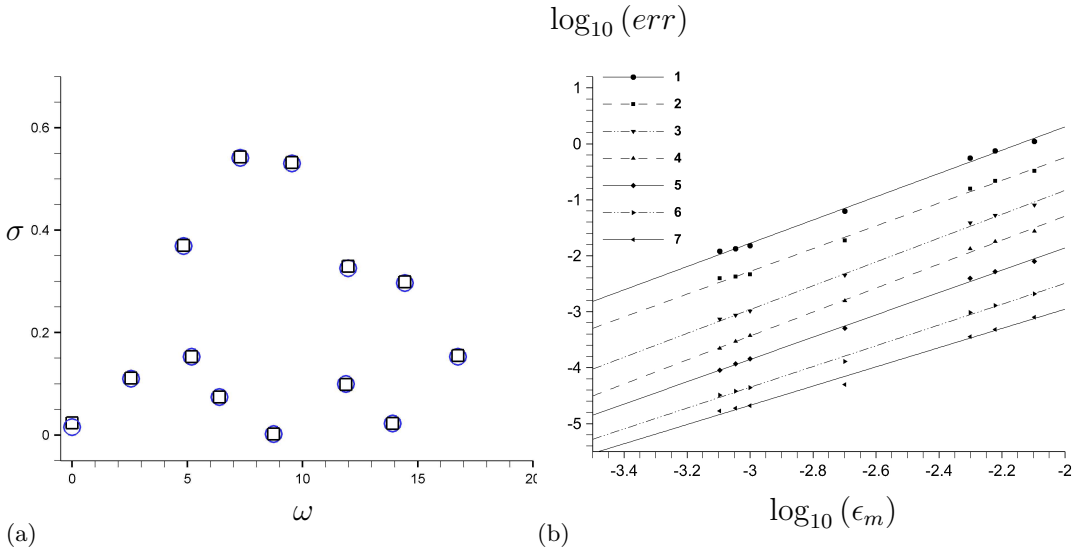

(a) (b)

FIGURE 5.19: (a): Impact of the parameter $M = 0.1$ used for the Jacobian matrix computation onto the spectrum: □ spectrum obtained using the classical Spalart-Allmaras model $M = 0$, ○ spectrum obtained using $M = 0.1$. The spectrum is poorly affected by the modification. (b): Spectrum convergence with ϵ using $M = 0.1$ for the Jacobian computation.

adjoint modes are computed and are found identical to the previous ones. The spectrum is poorly affected by this modification as can be noticed in Fig.5.19(a). Note that the term f_w was linearized for the Jacobian computation. Indeed we observed that the sensitivity gradients were greatly modified if f_w was frozen in the Jacobian computation. The spectrum convergence is re-investigated similarly to Section 5.2.5. The eigenvalues convergence for mode $1-7$ with the linearization parameter ϵ_m are shown in Fig.5.19(b). The convergence is not strongly affected as can be observed in Table 5.9 where we compare the regression coefficients R and the convergence slopes a with the case $M = 0$.

Mode number	1		2		3		4		5		6		7	
Parameters	a	R^2	a	R^2	a	R^2	a	R^2	a	R^2	a	R^2	a	R^2
$M = 0$	1.8	0.99	2.0	0.99	2.1	0.99	2.0	0.99	1.9	0.99	1.7	0.99	1.6	0.98
$M = 0.1$	2.1	0.99	2.0	0.99	2.1	0.99	2.1	0.99	2.0	0.99	1.9	0.99	1.7	0.99

TABLE 5.9: Linear fit parameters of the eigenvalues convergence with ϵ_m for the Spalart-Allmaras turbulence model.

We then compute the sensitivity gradient to baseflow perturbations $\boldsymbol{\nabla}_{\mathbf{w_b}}\lambda$ using the constant $M = 0.1$ and freezing the computation of f_w in the residual evaluation. The different components of the growth rate sensitivity gradient $\boldsymbol{\nabla}_{\mathbf{w_b}}\sigma|_{\mathbf{Q}}$ are depicted in Fig.5.20. All forms of discontinuities have vanished.

Finally, the sensitivity gradient to a steady force $\boldsymbol{\nabla}_{\mathbf{f}}\lambda$ is computed using both the new Jacobian matrix and sensitivity gradient $\boldsymbol{\nabla}_{\mathbf{w_b}}\lambda$. We depicted in Fig.5.21(a) the predicted impact of a control cylinder onto the mode 1 growth rate $\delta\sigma_{xy}$ obtained with our modified Spalart-Allmaras model. We compare it to the one initially computed in Section 5.3.3

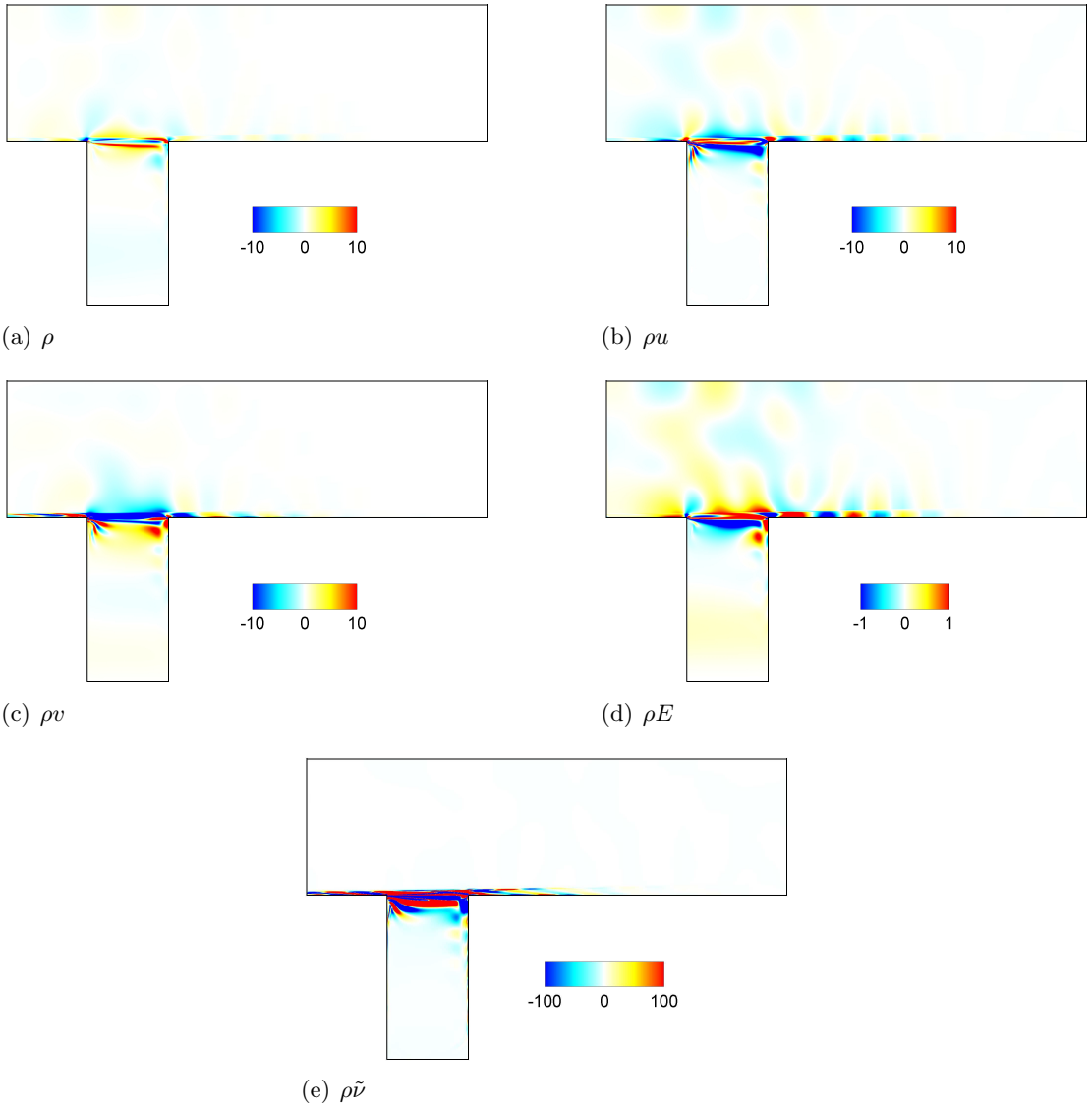

(a) ρ (b) ρu

(c) ρv (d) ρE

(e) $\rho\tilde{\nu}$

FIGURE 5.20: Growth rate sensitivity to baseflow perturbations $\boldsymbol{\nabla}_{\mathbf{w_b}}\sigma|_{\mathbf{Q}}$ of mode 1 obtained with the modified Spalart-Allmaras model. The constant $M = 0.1$ is used and the term f_w is frozen.

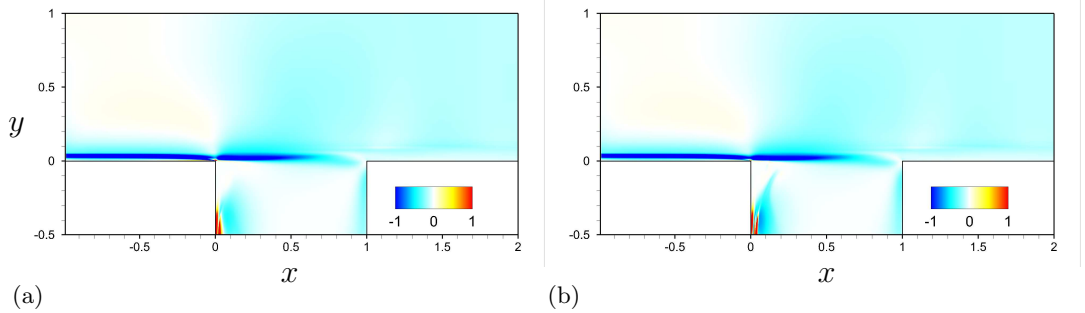

(a) (b)

FIGURE 5.21: Variation of the eigenvalue growth rate $\delta\sigma_{xy}/\|\lambda\|$ due to the presence of a control cylinder at (x,y) (mode 1) for the Spalart-Allmaras. (a): modified model with $M = 0.1$ and freezing the function f_w. (b): model version implemented in elsA.

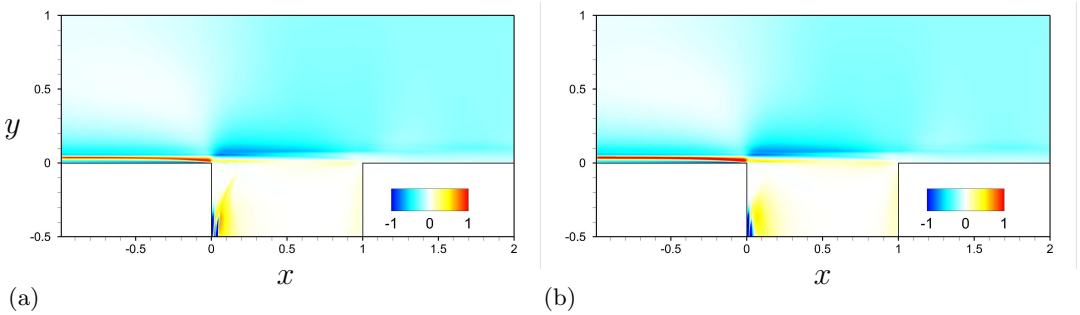

(a) (b)

FIGURE 5.22: Variation of the eigenvalue frequency $\delta\omega_{xy}/\|\lambda\|$ due to the presence of a control cylinder at (x,y) (mode 1) for the Spalart-Allmaras. (a): modified model with $M = 0.1$ and freezing the function f_w. (b): model version implemented in elsA.

an re-plotted in Fig.5.21(b). Both control maps compare reasonably well suggesting that the added modifications poorly affect our final results. Similarly, the impact of the control cylinder onto the mode frequency $\delta\omega_{xy}$ computed with our modified version is depicted in Fig.5.22(a) and can be compared to the control map initially obtained in Fig.5.22(b). As a consequence, the proposed modification seems to barely affect the final results but improve significantly the linearization process of the Spalart-Allamaras turbulence model.

5.5 Concluding remarks

A turbulent compressible flow over a deep cavity was considered as a test case study for our fully discrete formalism. The flow dynamics is modeled using the RANS equations closed with a turbulence model, and the natural flow unsteadiness is recovered when integrating in time the unsteady RANS equations in agreement with experimental results. A stability analysis was then performed using our fully discrete method. The discrete equations were linearized using finite differences applied to the evaluation of the Navier-Stokes residual $\mathcal{R}$. The stability of the flow is assessed by solving the direct and adjoint eigenvalue problems linked to the Jacobian matrix $\mathbf{J}$.

The flow is found to be unstable with the existence of several unstable modes. The fundamental frequency of the flow as well as several harmonics were shown to be linked to aero-acoustic modes associated with a feedback mechanism. The agreement between the linear stability analysis and the unsteady simulations suggest that the flow unsteadiness is linked to the existence of these unstable modes. Typical structures of Kelvin-Helmholtz instabilities are recovered when considering the spatial structure of the modes. The acoustic features of the flow were also captured as we observed acoustic resonance modes excited by Kelvin-Helmholtz instabilities. In the view of open loop control, the sensitivity gradient of the unstable eigenvalue to baseflow perturbations

$\boldsymbol{\nabla}_{\mathbf{w_b}}\lambda$ was computed. The flow was found to be mostly sensitive near the mixing layer and upstream of the cavity. Finally, the sensitivity gradient to a steady force $\boldsymbol{\nabla}_{\mathbf{f}}\lambda$ was extracted, indicating interesting areas of the flow where a steady force could lead to the stabilization of the unstable eigenvalue. A previsional control map using a steady cylinder as a mean to control the flow was derived for the fundamental mode. The cylinder was found to have a stabilizing effect on the mode near and upstream of the leading edge of the cavity, in agreement with experimental results.

Numerous numerical tests were performed to analyse the robustness and validity of our fully discrete method. Mesh discretization was found to poorly affect the unstable modes frequency but did influence their growth rate. The impact of the linearization parameter onto the Jacobian computation was characterized. The spectrum was observed to converge to the second order with the linearization parameter attesting the precision of the Jacobian computation. The genericity of the method with the system of equations was also investigated. As expected, the numerical scheme poorly affect the results. On the contrary, the choice of turbulence model had a slight impact on the growth rates of the unstable eigenvalues but not on their frequency. Still, similar features were obtained using both $k-\omega$ of Wilcox and Spalart-Allmaras turbulence model. The sensitivity gradients were validated using a discrete evaluation of the eigenvalue. In particular, steady control maps computed with the different models lead to similar areas near and upstream of the mixing layer to investigate flow control. The gradient were found to correctly predict the eigenvalue variation with an error lower then 3%. Finally, a particular analysis of the Spalart-Allmaras model was performed and a modification was proposed to improve the linearization of the model. The modifications were shown to poorly modify our results.

To conclude, the cavity configuration appeared as a robust case to test our method. The performed numerical validations demonstrate that our fully discrete formalism does enable the computation of the discrete Jacobian and sensitivity gradients. The code can be used in a black-box manner and no analytical derivations need to be performed. The coherence of the linear stability results with experimental datas and unsteady simulations suggest the relevancy of linear stability analysis to characterize unsteady dynamics of turbulent flows modeled using RANS equations.

Chapter 6

Application cases

As the novelty of the present work consists in the development of a new tool to perform linear stability analysis, we will present in the following three studies that were conducted within and in parallel to this Ph.D at the DAFE, and using the formalisms and tools that we previously presented. These three cases allowed us to further analyse the information carried out by stability analysis and verify on other dynamics the validity of our tools. The role of this Chapter is to give an insight of the applications of the developed methods rather than to fully characterize new configurations. We will thus focus on specific results such as unstable modes, adjoint modes, gain curves, or sensitivity maps made available thanks to our tools, and will not present the integrality of the performed work (parametric study, mesh convergence...). A brief overview to place each study in its context will be given, which may lack references as these works were not the core of this Ph.D. We will first detail two analyses concerned with the dynamics of shock wave/boundary layer interactions (SWBLI). In Section 6.1.1, the oscillator dynamics of a transonic shock over an airfoil will be analysed. This work was performed in collaboration with Fulvio Sartor an other Ph.D student at the DAFE. We will then detail in Section 6.1.2 some results obtained by Fulvio Sartor who analysed the noise amplifier dynamics of a strong shock over a curved wall. As a last case, the characterization of a supersonic under-expanded jet in a co-flow as an oscillator will be presented in Section 6.2, a study performed by Samir Benedine during his Master's thesis at the DAFE.

6.1 Shock wave/boundary layer interactions

As detailed by Dolling [115], SWBLI have been extensively studied over the last decades. Such interactions are present in many aeronautical applications and generally induce undesirable features such as drag rise, massive flow separation, shock unsteadiness, and high

wall heating. SWBLI remain a challenging problem which encompasses compressibility, turbulent effects and separation. The question of the origin of SWBLI unsteadiness remains open. Investigating the linear stability of a laminar SWBLI on a flat plate, Robinet [71] was the first to link SWBLI unsteadiness to the existence of a steady three-dimensional unstable mode. More recently, Touber and Sandham [116] performed a stability analysis on a mean-flow computed from a three dimensional LES simulations, and found that the most unstable mode was steady and two dimensional. As previously stated, Crouch et al. [63] analysed the SWBLI over an airfoil and linked the buffeting onset to the existence of a globally unstable mode of the RANS equations. These previous studies suggest that linear stability analysis may be an interesting tool to characterize flow unsteadiness in SWBLI.

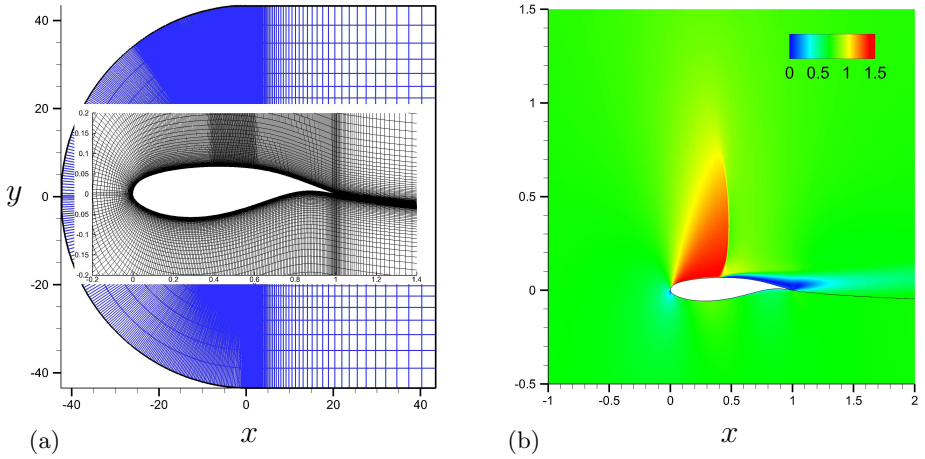

FIGURE 6.1: (a): Mesh discretization of the profile OAT15A. (b): Mach number contours of the baseflow $\mathbf{w_b}$.

6.1.1 Transonic buffet over an airfoil

In transonic conditions, a strong compression shock forms on wings, followed by a boundary layer separation upstream of the trailing edge. For sufficiently high angle of attack of the wing, the interaction between the shock and the turbulent boundary layer leads to the creation of large scale instabilities. The shock oscillates inducing structural vibrations and load fluctuations, a phenomenon named buffeting. The determination and understanding of the buffet occurrence is of critical importance for designers as it limits the performance of a wing profile in terms of maximum lift. The postponing of buffet onset is a key target in the profile design process and constitutes the aim of most flow control techniques, such as vortex generators on wings or suction slots in air intakes (see Seegmiller et al. [117], Caruana et al. [118]). Numerical simulations based on the unsteady RANS equations or zonal detached eddy simulations have been extensively used

to predict buffet onset with some degree of success (Deck [43], Barakos and Drikakis [119], Chung et al. [120]). Although CFD simulations well capture the flow physics, the agreement with experimental results remains however qualitative (Jacquin et al. [1]).

Recently, Crouch et al. [63, 64] linked the buffet onset over a NACA0012 profile to the appearance of a globally unstable mode, performing a linear stability analysis of the RANS equations closed with the Spalart-Allmaras turbulence model. These results encouraged us to revisit the buffet onset problem with our fully discrete formalism. Rather than analysing the NACA0012 profile, we chose to use an OAT15A profile which was designed at the ONERA and experimentally characterized by Jacquin et al. [1]. The wing profile, depicted Fig.6.1(a), is characterized by a cord length $c = 0.23$m and a relative thickness of 12.3%.

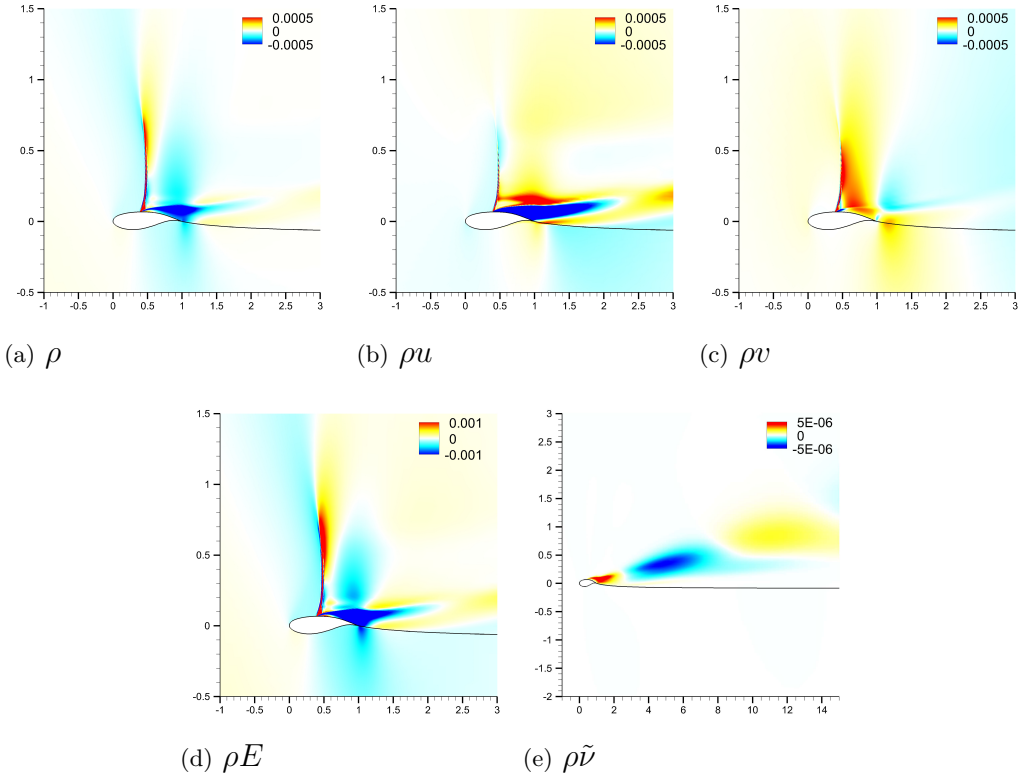

(a) ρ (b) ρu (c) ρv

(d) ρE (e) $\rho\tilde{\nu}$

FIGURE 6.2: Spatial structure of the direct buffet mode $\hat{\mathbf{w}}$, the real part is plotted.

We impose an adiabatic wall condition on the profile and the angle of attack α of the wing is fixed by changing the incoming fluid direction. The computational domain is taken sufficiently large (computational borders are imposed at $40c$ of the wing) so that the flow returns to its initial state on the external boundaries were a non reflexion with upstream flow conditions are imposed. An example of mesh discretization used is plotted in Fig.6.1(a), the mesh being generated with an ONERA software.

We mimic the study by Jacquin et al. [1] using a stagnation temperature $T_\infty = 300$K, a stagnation pressure $P_\infty = 10^5$Pa and a Mach number $M = 0.73$, leading to a Reynolds number based of the cord length of $R_e = 3 \times 10^6$. All quantities are made dimensionless using the free stream variables ρ_∞,U_∞,T_∞ and the profile cord c. The parametric study of this configuration was performed by Fulvio Sartor, who varied the angle of attack α and the mesh discretization to study their impact on the buffet onset. He found that unsteady simulations (uRANS) closed with the Spalart-Allmaras turbulence model reproduced the buffet onset for a critical angle of attack. Using our discrete method, he observed the appearance of a globally unstable mode of the baseflow for critical angles of attack close to the one computed using uRANS simulations.

Among the available datas, we chose to use the baseflow computed with the mesh depicted in Fig. 6.1(a) for a critical angle of attack $\alpha = 4.5$, and performed a complete stability analysis of this configuration in the following. Contours of the Mach number for the computed baseflow are depicted in Fig.6.1(b). We observe the formation of a shock on the suction side of the profile, with the formation of a recirculation bubble downstream of the shock.

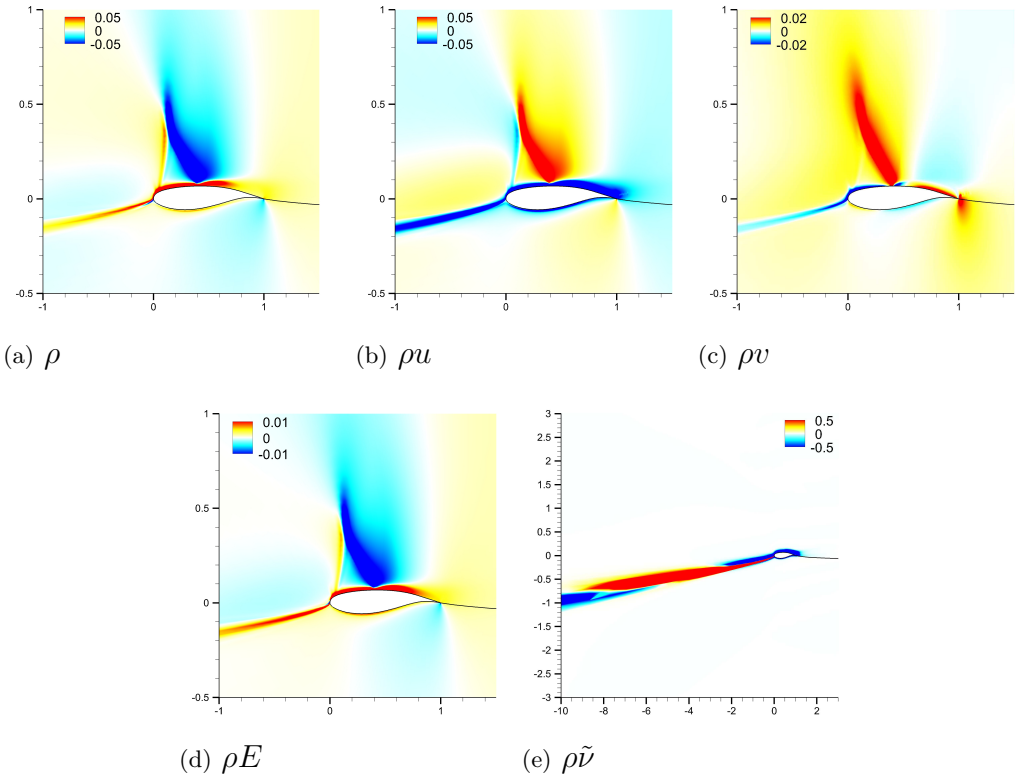

(a) ρ (b) ρu (c) ρv

(d) ρE (e) $\rho\tilde{\nu}$

FIGURE 6.3: Spatial structure of the adjoint buffet mode $\tilde{\mathbf{w}}|_{\mathbf{Q}}$, the real part is plotted.

The Jacobian matrix $\mathbf{J}$ is then computed as in Section 3.2.2, and the eigenvalue problem in Eq. 2.5 solved. The baseflow is found to be unstable with the existence of one unstable

mode of growth rate $\sigma = 4.5 \times 10^{-2}$ and pulsation $\omega = 0.46$. The real part of the spatial structure of the mode is depicted in Fig.6.2. The mode structure is mainly located in the shock and in the recirculation bubble. Typical structures of Kelvin-Helmoltz instabilities are observed for the different components that propagate downstream of the profile. These structures seem to raise from the recirculation bubble. The turbulent fluctuations do not seem to impact the shock, while for all other components, we observe an opposite sign between the shock and the recirculation bubble. This suggest that shock oscillations and bubble expansions or breathing are in phase opposition.

The corresponding adjoint mode is straightforwardly obtained solving Eq. 2.10. The real part of the spatial structure of the adjoint mode is depicted in Fig.6.3. The adjoint mode is mostly located near and upstream of the shock and propagates upstream.

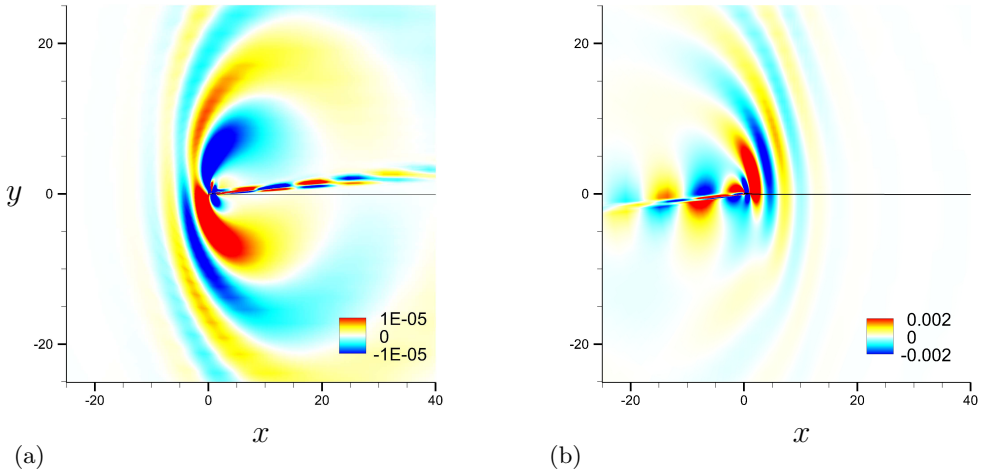

FIGURE 6.4: Saturated levels of the ρ component of the direct mode $\hat{\mathbf{w}}$ (a) and the adjoint mode $\tilde{\mathbf{w}}|_{\mathbf{Q}}$ (b). The real part is plotted.

Model	ρ	ρu	ρv	ρE	$\rho\tilde{\nu}$
Spalart-Allmaras	10^{-4}	10^{-4}	10^{-5}	10^{-3}	10^{-8}

TABLE 6.1: Linearization parameter ϵ_{m_2} used for the computation of the matrix $\mathbf{H}'$.

As we use compressible equations, we expect to observe some acoustic effects in the flow. We depicted in Fig.6.4(a) the saturated levels of the density component ρ of the direct mode as well as those of the adjoint mode Fig.6.4(b). We observe the propagation of acoustic waves downstream of the profile for the direct mode and upstream for the adjoint. In particular, we recover the non normality of the Jacobian due to the oppositive sign of the advection term between the direct and adjoint equations.

We then compute the matrix $\mathbf{H}'$ as proposed in Section 3.2.3. The linearization parameter ϵ_1 was set to 10^{-3}, while the values used for ϵ_2 are summarized in Table 6.1. The sensitivity gradient to baseflow perturbation $\boldsymbol{\nabla}_{\mathbf{w_b}}\lambda$ is straightforwardly obtained

using Eq. (2.19). We depicted in Fig.6.5 the real part of the different components of the gradient.

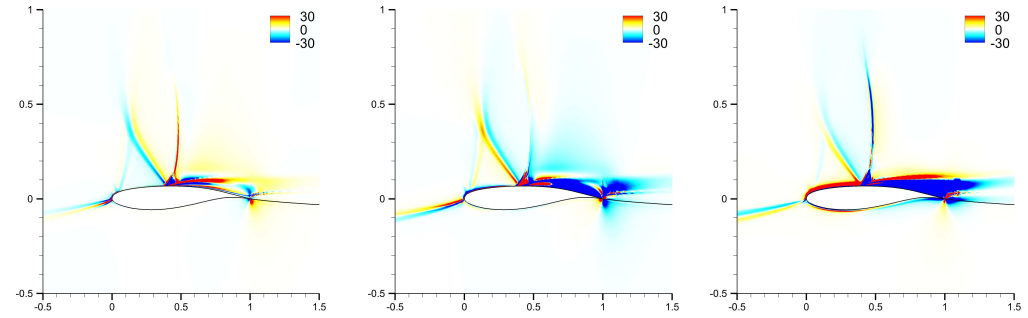

(a) ρ (b) ρu (c) ρv

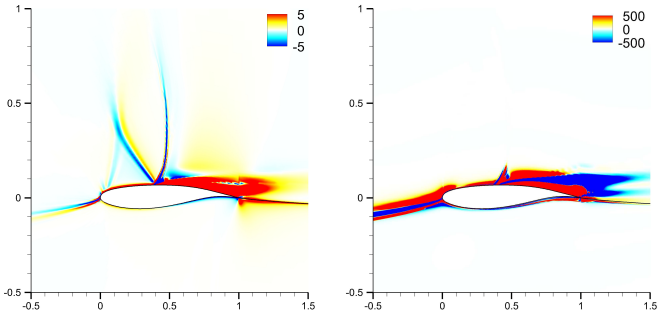

(d) ρE (e) $\rho\tilde{\nu}$

FIGURE 6.5: Sensitivity of the growth rate $\boldsymbol{\nabla}_{\mathbf{w_b}}\sigma|_{\mathbf{Q}}$ to baseflow perturbations.

A first remark is that some discontinuities are observed near the trailing edge. These discontinuities are not linked to the linearization of the turbulent equations. Note that in the spirit of Section 5.4, the constant $M = 1.0$ was used in the linearization process and f_w was frozen. Furthermore, the limiter on the cross diffusion term was suppressed as it lead to discontinuities in the gradient in this case. We believe that the origin of these discontinuities relies in the poor mesh discretization in this area. This suggests that the mesh should be further refined in this zone for a complete characterization. The baseflow is sensitive near the shock and the boundary layer, as well as upstream of the shock and the wing.

Finally, we compute the sensitivity gradient to a steady force $\boldsymbol{\nabla}_{\mathbf{f}}\sigma|_{\mathbf{Q}}$ using Eq. 2.21. The real part of the gradient fields are plotted in Fig.6.6. As for the cavity case in Chapter 5, the discontinuities are smoothed by the inverse of the adjoint Jacobian $\mathbf{J}^{-1*}$. We observe in Fig.6.6(b) that a streamwise force in the boundary layer or in the recirculation bubble will have a stabilizing effect on the unstable mode. This can be interpreted as an energization effect of the boundary layer that becomes less prone to separation.

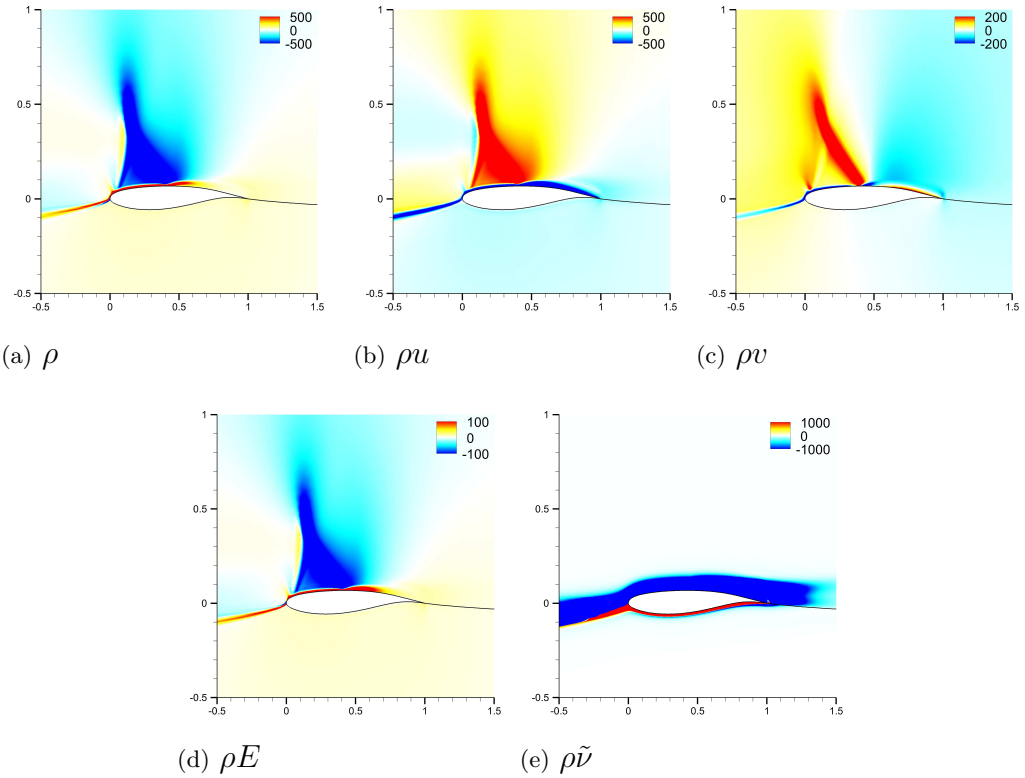

(a) ρ (b) ρu (c) ρv

(d) ρE (e) $\rho\tilde{\nu}$

FIGURE 6.6: Sensitivity of the growth rate $\boldsymbol{\nabla}_{\mathbf{f}}\sigma|_{\mathbf{Q}}$ to a steady force.

To conclude, the buffet onset seems to be linked to the appearance of a globally unstable mode. The mode is mostly located near and inside the shock and the recirculation bubble. A control map was derived which indicates that a streamwise forcing near the wing profile may lead to a stabilization of the flow. These results remain preliminary as a further analysis of the mesh discretization needs to be performed, but lead to interesting features of the flow.

6.1.2 Strong shock over a curved profile

This study realised by Fulvio Sartor at the DAFE focuses on a strong normal shock impinging on a curved profile as depicted in Fig.6.7. The shock shape is modified by the interaction with the boundary layer and adopts a lambda pattern. The boundary layer detaches near the shock foot and forms a recirculation bubble downstream of the shock. The flow unsteadiness is characterized by two distinct frequencies: a low frequency linked to a slow motion of the shock, and a high frequency that can be observed in the mixing layer downstream of the separation line.

This configuration was experimentally studied at the DAFE by Sartor et al. [121] and the aim of this study is to further characterize this dynamics using linear stability analysis.

From a linear stability point of view, this flow is stable: no unstable modes are observed, and the flow dynamics may be analysed as a noise amplifier. We will briefly introduce in the following some interesting results obtained by Fulvio Sartor using the methodology and computational procedures presented in Section 2.3 and 3.1.1. A deeper analysis of these results can be found in Sartor et al. [122].

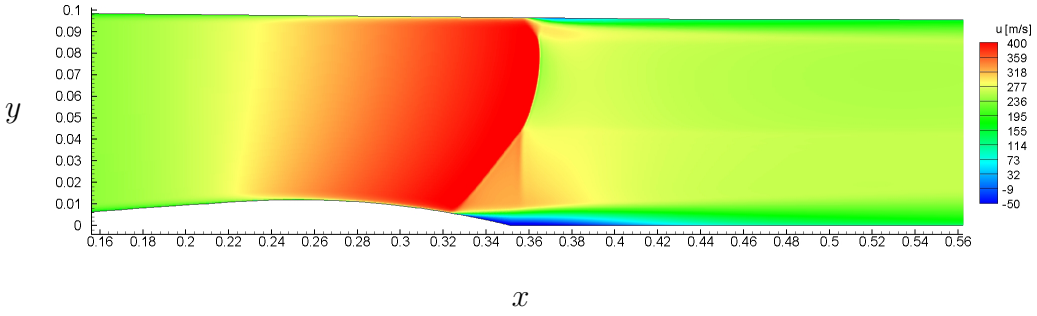

FIGURE 6.7: Isocontours of the streamwise velocity component of the baseflow.

The incoming flow is subsonic and turbulent with a Reynolds number of $R_e = 1.4 \times 10^6$. A wall adiabatic condition is imposed on the upper and lower part of the domain while an injection condition is fixed at the inlet. The pressure at the outlet is fixed so that the shock position corresponds to the experimental case. Isocontours of the streamwise velocity of the baseflow can be observed in Fig.6.7 were we recover the lambda pattern of the shock. The Spalart-Allmaras turbulence model is used to model the baseflow turbulence, the convective flux is discretized using the AUSM+ scheme, and the turbulence modeled is linearized for the Jacobian computation.

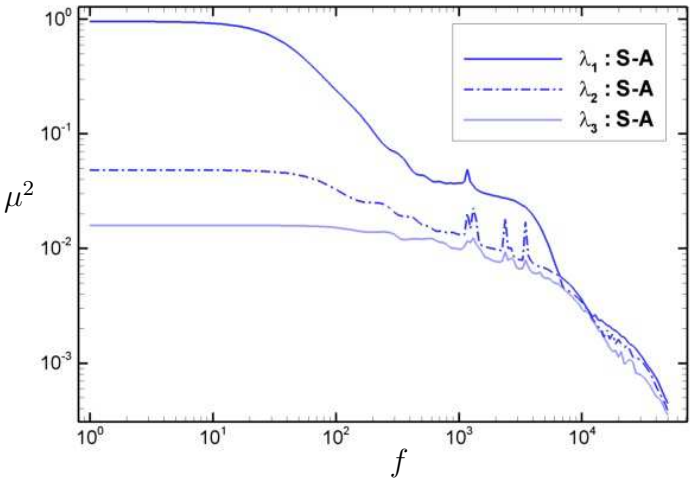

FIGURE 6.8: Optimal gain curve as a function of the forcing frequency f (Hz). The Spalart-Allmaras turbulence model was used for the baseflow computation.

As stated in Section 2.3, the dynamics of noise amplifiers is analysed by considering the flow response $\hat{\mathbf{x}}$ to harmonic forcing. The methodology proposed in Section 2.3.5 is thus

followed. The Jacobian matrix $\mathbf{J}$ is first computed according to the procedure detailed in Section 3.2.2 with a linearization parameter $\epsilon = 5.0 \times 10^{-6}$ (results were observed to be converged with ϵ). The pseudo scalar product $\mathbf{Q_e}$ introduced in Section 2.3.3 is used for the maximization of the kinetic energy, and the forcing terms are normalized with the scalar product $\mathbf{Q}$ introduced in Chapter 4. The forcing restriction $\hat{\mathbf{f}}_\mathbf{s}$ introduced in Section 2.3.4 is also applied as only momentum components forcing is allowed. The prolongation operator $\mathbf{P}$ is thus straightforwardly derived by adding 0 to the prolonged vector $\hat{\mathbf{f}} = \mathbf{P}\hat{\mathbf{f}}_\mathbf{s}$. The resolvent $\mathscr{R}_\omega$ is finally computed for different frequencies ω and the optimal gain μ^2 is then obtained solving the eigenvalue problem in Eq. (2.77). The resolution of the eigenvalue problem gives access to the set of optimal forcing $\hat{\mathbf{f}}_\mathbf{s}$, and the set of optimal response $\hat{\mathbf{x}}$ is then determined solving Eq. (2.76).

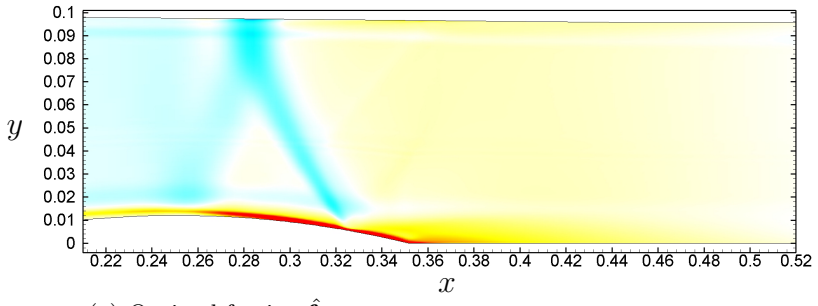

(a) Optimal forcing $\hat{\mathbf{f}}_\mathbf{s}$.

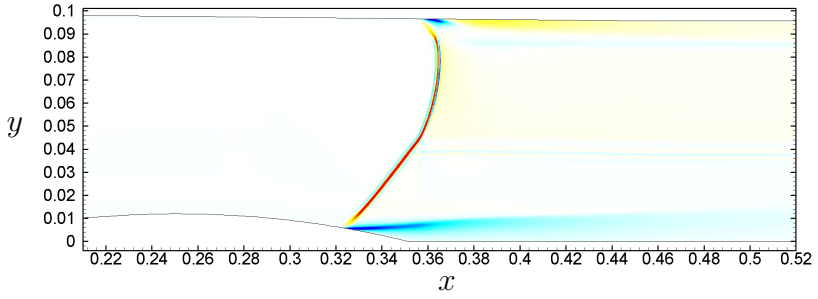

(b) Optimal response $\hat{\mathbf{x}}$.

FIGURE 6.9: Streamwise component of the optimal forcing and response for a forcing frequency of $f = 50$Hz.

The three most energetic singular values of the global resolvent are depicted in Fig.6.8. The gain function is not constant, and is more energetic for low frequencies up to 50 Hz. It then decreases rapidly to another plateau for $f = 1 - 4$ kHz. As the configuration is known to be characterized by a low and a high frequency (Sartor et al. [122]), two types of flow forcing and response are analysed.

For low frequency forcing, $f = 50$Hz was chosen to study both optimal forcing and response. As can be observed in Fig.6.9(a), the optimal forcing is mostly located in the boundary layer on the divergent part of the bump and its strongest values are located within the shock foot. The optimal response in Fig.6.9(b) extends on the shock wave,

with a spatial structure similar to low-frequency Fourier mode observed experimentally by Sartor et al. [122]. Low-frequency response is associated to a breathing of the recirculating bubble whose contractions are related to downstream motion of the reflected shock as indicated by the opposite sign in the shock and the mixing layer in Fig.6.9(b). Similarly, the expansions of the bubble are induced by upstream motion of the reflected shock. This observation is consistent with the model proposed by Piponniau et al. [123].

In the same spirit, a high-frequency $f = 3000$Hz is then considered. The optimal forcing in Fig.6.10(a) is still located before the shock and near the beginning of the mixing layer. Moreover, the maximum value is once again attained at the shock foot, where the pressure gradient causes the separation of the boundary layer. The induced response structures start from the separation point around $x = 0.33$mm as shown in Fig.6.10(b). They are characterized by a small wavelength compared to the size of the recirculation bubble. This feature suggests that the high-frequency unsteadiness is associated to the so called flapping motion of the shear layer (see Kiya and Sasaki [124]).

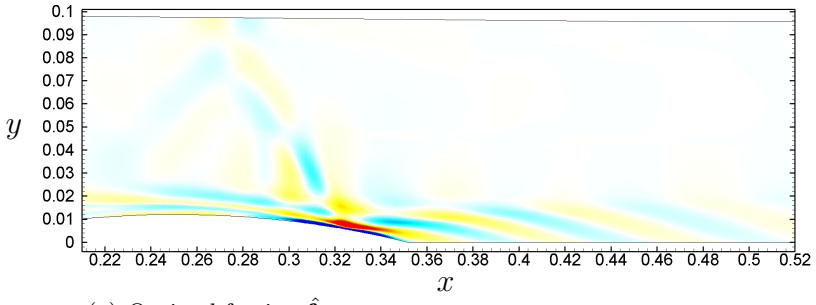

(a) Optimal forcing $\hat{\mathbf{f}}_\mathbf{s}$.

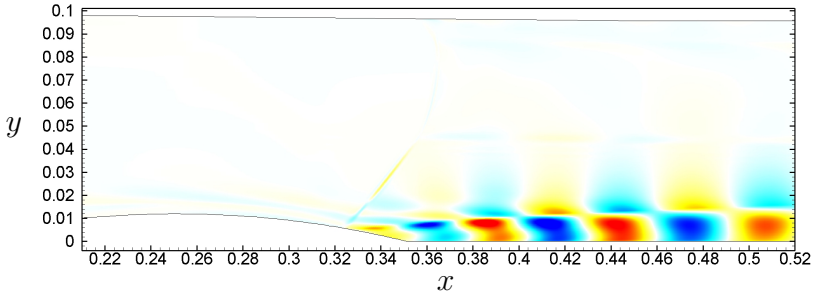

(b) Optimal response $\hat{\mathbf{x}}$.

FIGURE 6.10: Streamwise component of the optimal forcing and response to a forcing frequency of $f = 3000$Hz.

To conclude, the fully discrete method used to perform a linear stability analysis of the flow dynamics leads to interesting features in agreement with experimental results. The low-pass filter behavior of the shock is recovered as well as the high frequency flapping of the recirculation bubble.

6.2 Screech in jets

Under certain conditions, imperfectly expanded jets produce a discrete tone referred to as screech. The study of supersonic jet screech began in the early 1950s with the seminal work of Powell [125–127], who discovered this phenomenon solely from schlieren visualization of rectangular chocked jets. Almost 50 years after Powell's discovery, screech still plays a critical role in the design of advanced aircraft because it can cause sonic fatigue failure. Indeed, as stated by Raman [4], such failures have been observed before on the British Aircraft Corporation's $VC-10$ and on the $F-15$ and $B1-B$ of the United States Air Force.

Under expanded jets correspond to flows in which the static pressure is higher inside the jet than outside. Shocks and expansion fans naturally appear at the nozzle lip region to compensate the pressure mismatch. When the oblique shocks or expansion fans impinge on the jet boundary they are reflected back into the jet leading to the formation of quasi-periodic shock-cells structures (see Tam [128]). Perturbations created at the nozzle lip propagate downstream and are reflected by the shocks, leading to an acoustic feedback mechanism between the nozzle lip and the shocks responsible for screech.

The screech frequency f is thus expected to be related to the travel time of the perturbation. A simple relation can be found in Powell's work [125–127] for jets with an ambient flow at rest. Imposing a co-flow u_1 alters the screech frequency, since it has an impact on the time a perturbation needs to travel upstream. This point has been studied by Bryce and Pinker [129] who proposed an adaptation accounting for the co-flow, leading to the following formula for screech frequency:

$$f = \frac{0.7\,(u_j - u_1) + u_1}{l_s\left(1 + \dfrac{0.7\,(u_j - u_1) + u_1}{c_1 - u_1}\right)}, \tag{6.1}$$

where l_s is the shock-cell spacing, u_j the fully expanded jet velocity and c_1 the speed of sound in the co-flow.

Linear stability analysis has been successfully used to characterize jet flows dynamics (Bagheri et al. [130], Meliga and Chomaz [131], Nichols and Lele [132]). For under-expanded jets, Tam [128] gave a prediction of the extension of the shock-cell structures l_s in good agreement with experimental datas using a vortex-street shock cell model combined with local stability analysis. These results suggest that global stability analysis may be a useful tool to characterize such dynamics. In this spirit, the present study was conducted by Samir Benedine at the DAFE who considered a two dimensional cold supersonic under-expanded free jet. The jet is laminar and formed by the junction of a

co-flow and a flow exiting a nozzle of height $h = 3$mm and width $b = 15$mm ($b/h = 5$) at $x = 0$ as sketched in Fig.6.11(a).

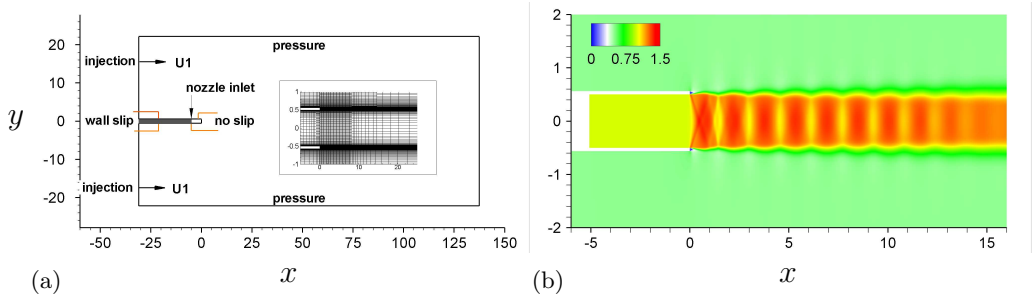

FIGURE 6.11: (a): Sketch of the jet configuration with boundary conditions. In the inward is depicted the discretization near the nozzle exit (one discrete point out of two). (b): Mach number contours of the baseflow $\mathbf{w_b}$ near the nozzle exit.

The imposed boundary conditions are also sketched in Fig.6.11(a) together with an example of the mesh structure near the jet nozzle in the inward of the figure. An injection condition is imposed at the entrance of the nozzle with a Mach number set to $M = 1$ leading to a Mach number at the nozzle exit $M_d = 1$. An injection condition is also used for the ambient flow, whom characteristics are chosen to impose the ratio between the pressure at the nozzle exit p_e and the ambient pressure p_1 to 1.4, leading to a Mach number in the co-flow equal to $M_1 = 0.5$. Ambient pressure conditions are imposed on the upper and lower part of the domain, as well as at the outlet where the flow is subsonic. No particular boundary conditions are required at the outlet where the flow is subsonic as the characteristic relations are respected on the boundaries. In the planes $y = +-h$, a wall slip condition is imposed for $x < -b$ (ambient flow), while an adiabatic no-slip condition is imposed for $-b \leq x \leq 0$ (for both nozzle and ambient flow). The stagnation temperature is set to $T = 288$K, the Prandt number to $P_r = 1$, and the Reynolds number based of the ambient velocity u_1, density ρ_1, nozzle height h, and Sutherland's law for the viscosity is equal to $R_e = 5325$. All quantities are made dimensionless using the nozzle height h, the ambient velocity u_1, density ρ_1 and viscosity μ_1 computed with Sutherland's law.

The Mach number contours or the baseflow are depicted in Fig.6.11(b) where we recover the shock-cell structures. The shock-cell length is found to be equal to $l_s = 1.44$ in good agreement with the formula by Tam [128]. The Mach number at the nozzle exit being equal to $M_d = 1$, the fully expanded jet Mach number M_j is defined by (see Berland et al. [133]):

$$M_j = \left\{ \frac{2}{\gamma - 1} \left[\left(1 + \frac{\gamma - 1}{2} M_d^2 \right) \left(\frac{p_e}{p_1} \right)^{(\gamma-1)/\gamma} - 1 \right] \right\}^{1/2}, \tag{6.2}$$

and is equal to 1.27, leading a fully expanded jet velocity u_j of 2.15 (taken at $y = 0$ at the x station where $M = M_j$).

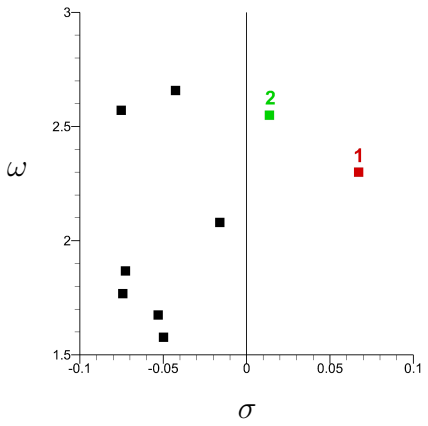

FIGURE 6.12: Spectrum of the baseflow $\mathbf{w_b}$.

The Jacobian matrix $\mathbf{J}$ is then extracted as presented in Section 3.2.2 and the eigenvalue problem in Eq. (2.5) is solved. An example of computed spectrum for this configuration is plotted in Fig.6.12. Two globally unstable modes are found, mode 1 is characterized by a growth rate $\sigma_1 = 0.067$ and a pulsation $\omega_1 = 2.3$, while mode 2 is characterized by $\sigma_2 = 0.0136$ and $\omega_2 = 2.54$. Both modes present similar spatial structures, as an example we depicted the streawise and crosswise component of mode 1 in Figs.6.13(a) and 6.13(b) respectively. For both modes, the streamwise component is anti-symmetric while the crosswise is symmetric. Such features are similar to sinuous and varicose modes as observed by Berland et al. [133].

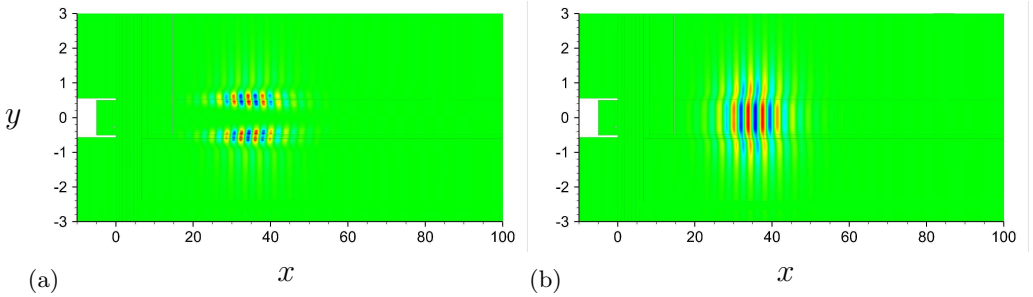

FIGURE 6.13: Spatial structure of the streamwise ρu (a) and crosswise ρv (b) components of the unstable mode 1. The real part is plotted.

The frequency prediction using Eq. (6.1) leads to a dimensionless screech frequency around $f = 2.7$, close but higher than both unstable mode frequencies $f_1 = 2.29$ and in $f_1 = 2.54$. These preliminary results enhance the valuable information carried out by stability analysis to characterize the dynamics of under-expanded jets.

6.3 Concluding remarks

Our fully discrete method was further applied to analyse several configurations. The dynamics of shock-boundary layer interactions was first investigated in the case of the transonic buffet over a wing profile. The flow unsteadiness was found to be reproduced by unsteady simulations and was linked to the existence of an unstable mode of the RANS equations. Both frequency and growth rate of the modes match reasonably well those obtained when integrating in time the unsteady RANS equations. The sensitivity gradients were then computed and the impact of a baseflow variations and a steady force were briefly discussed. A streamwise velocity forcing was found to have a stabilizing effect in the boundary layer and inside the recirculation bubble near the wing. We then presented some results obtained by Fulvio Sartor using our discrete method on the dynamics of a strong shock impinging of a curved wall. The noise amplifier dynamics of the flow was analysed and the low pass filter behavior of the shock was recovered. Properties of optimal forcing at high and low frequency were presented which reproduce the natural flow features. Finally, preliminary results obtained by Samir Benedine on sound generation in under-expanded jets were presented. The screech phenomenon seems to be linked to the existence of unstable modes of the RANS equations. These tests cases enhance the valuable information carried out by linear stability analysis and further validate our fully discrete methods. The proposed tools and developed formalism can thus be further applied in the future to characterize new configurations.

Chapter 7

Towards turbulence model free sensitivity analysis

We revisit in this Chapter the dynamics of the wake behind a D-shaped cylinder. The flow is turbulent and unsteady, characterized by Strouhal number of $S_t = 0.22$. This configuration was experimentally studied by Parezanović and Cadot [67], who showed that the use of a small steady cylinder can significantly alter the unsteadiness frequency of the natural flow. More recently, Meliga et al. [66] analysed this configuration by performing a stability analysis of the meanflow computed using the RANS equations closed with the Spalart-Allmaras model. They found that a slightly unstable mode existed, associated with a Strouhal number close to the one of the natural flow. Moreover, they showed using sensitivity analysis that the control effect of the cylinder was to modify the unstable mode frequency, in good agreement with the results of Parezanović and Cadot [67].

We propose to reconsider this turbulent case using our fully discrete formalism. The main idea behind this work is to question the definition of a relevant eddy viscosity for linear stability analysis of a turbulent meanflow, without the use of a turbulence model but rather thanks to available datas from a Direct Numerical Simulations (DNS) or experimental measurements. Note that this question is also relevant in the case of linear perturbations of meanflows computed from RANS simulations. Indeed, integrating in time the RANS equations yields the fluctuation of the coherent large scale structures of the turbulent flow, which may be used in order to redefine the eddy viscosity for linear stability analysis.

The configuration is presented in Section 7.1, while Section 7.2 is devoted to the analysis of the flow dynamics. The unstable modes are computed in Section 7.3, and the sensitivity gradients depicted in Section 7.4. Finally, beforehand control maps using a steady

cylinder as a means to control the flow are detailed in Section 7.5. This work was performed in collaboration with Farid Benyoucef and Hervé Bezard from the Aerodynamics and Energetics Modeling Department (DMAE) at ONERA.

7.1 Configuration

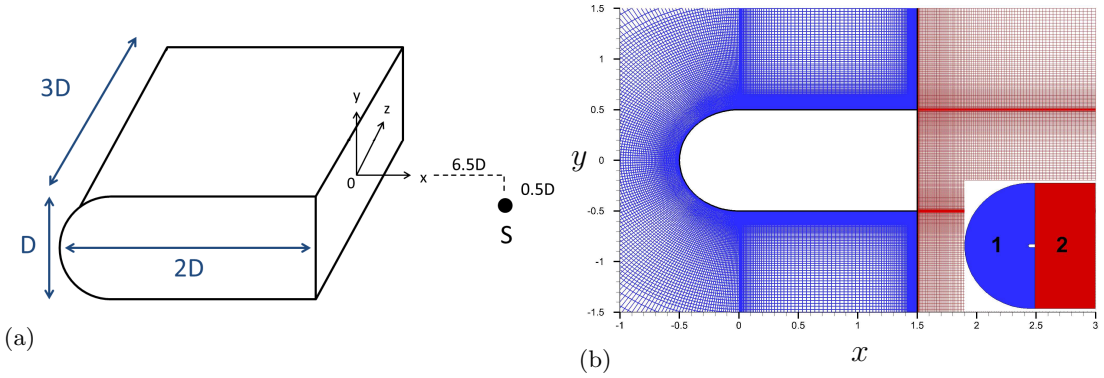

FIGURE 7.1: (a): Sketch of the configuration. (b): Mesh discretization near the cylinder. In the inlet are distinguished the two computational blocs.

We consider a D-shaped cylinder of height $D = 25$mm, length $L = 2D$ and width $W = 3D$ as sketched in Fig.7.1(a). We impose the incoming flow characteristics by setting the mach number $M = 0.2$, the stagnation pressure $p_\infty = 11667$Pa and the stagnation temperature $T_\infty = 292.5$K. The Reynolds number based of the cylinder height, the free stream density ρ_∞, velocity U_∞ and viscosity μ_∞ (computed with Sutherland's law) is equal to $R_e = 13000$. The turbulence level is set to 10^{-4} and the viscosity ratio $\mu_{t_\infty}/\mu_\infty$ is set to 0.1. All quantities are made dimensionless using the cylinder height D and the free stream variables ρ_∞, U_∞ and T_∞. This configuration mimics the studies by Parezanović and Cadot [67] and Meliga et al. [66]. Similarly to [67], we place a sensor S from which we measure the velocity and pressure fluctuations for the three dimensional unsteady simulations (see Fig.7.1(a)).

	Discretization points	Number of cells
Bloc 1	$357 \times 85 \times 40$	$30345 \times 40 = 1.2 \times 10^6$
Bloc 2	$150 \times 273 \times 40$	$40950 \times 40 = 1.6 \times 10^6$

TABLE 7.1: Bloc discretization properties.

The two dimensional mesh discretization in the x, y plane is shown in Fig.7.1(b) and consists in two blocs, with an external boundary located at 20D from the cylinder. A symmetric discretization is used with respect to the plane $y = 0$, with a tangential law for the evolution of the discretization step and imposing the cells adjacent to the downstream edge of the cylinder to be square of size $\Delta x = 5 \times 10^{-4}$. The configuration

is extended in the z direction for three dimensional simulations with a spatial extent of $W = 3D$ and is uniformly discretized with $\Delta z = 7.7 \times 10^{-2}$. Both blocs characteristics are summarized is Table 7.1 leading to a total number of cells of $N_m^{3D} = 2.8 \times 10^6$ for unsteady simulations and $N_m^{2D} = 70000$ for two dimensional stability analysis. Non-reflecting conditions with upstream properties are imposed on the outer part of the domain, with a periodic condition in the z direction, while a no-slip adiabatic condition is imposed on the cylinder surface.

Rather then performing a complete DNS, we propose to use three dimensional unsteady RANS simulations in order to obtain a relevant turbulent meanflow. The turbulence impact is modeled using the SAS model proposed by Menter and Egorov [134] which includes an additional source term compared to the original $k - \omega$ model of Wilcox. The effect of this source term is to reduce the eddy viscosity ν_t in areas where local unsteadiness develop, allowing the structures to stay alive and grow. Hence, this model differs from the classical turbulence models in the sense that it allows the resolution of a larger band of wavelength in the Kolmogorov spectrum.

Benyoucef et al. [135] have shown that the SAS turbulence model efficiently reproduced the turbulence features of the three dimensional wake behind a circular cylinder, while Didorally et al. [136] observed similar results for the three dimensional wake behind a heated square cylinder. From the similarity of these studies with our configuration, we performed the following analysis in collaboration with Hervé Bezard and Farid Benyoucef at ONERA (DMAE) who furnished the simulation maps (modeling, numerical schemes) used in [135], which we applied to compute the flow-field around our D-shaped cylinder. Similarly to Didorally et al. [136], a slight modification is applied in the definition of the additional source term in the $k - \omega$ model as proposed by Benyoucef (SAS-αL model, [135, 137]) which was shown to improve its efficiency. The Zeng limiter is used to prevent large values of ω. The Roe scheme extended to second order (MUSCL) is used for the discretization of the convective fluxes, with the Superbee limiter for the mean-field variables.

7.2 Flow dynamics

7.2.1 Unsteady simulations

The natural flow unsteadiness is characterized by a Strouhal number close to $S_t = 0.22$. The time integration is performed using an implicit backward Euler scheme, with a global time step $\Delta t = 10^{-4}/S_t$ which ensures that the time discretization will capture

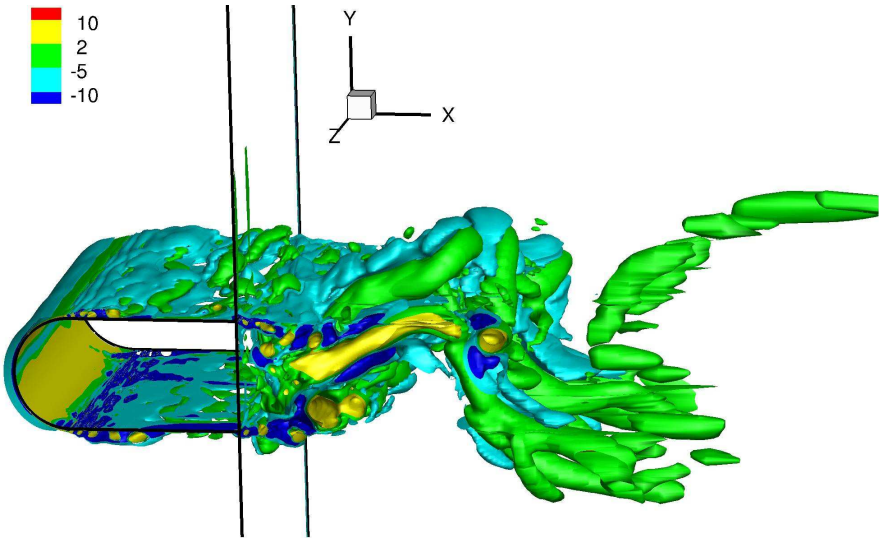

FIGURE 7.2: Q-criterion contours of the flow field at an arbitrary time.

the flow unsteadiness and yields a CFL condition of 1. We depicted in Fig.7.2 the Q-criterion contours of a snapshot of the flow field once the oscillatory regime is attained. We observe that the flow detaches quickly on the cylinder, and recover structures typical of a Von-Kármán alley in the wake of the cylinder. We extracted the velocity fluctuations at the sensor S and computed the flow spectrum using a Fast-Fourrier transform. The obtained spectrum is plotted in Fig.7.3(a) where we recover a dominant Strouhal number of $S_t = 0.23$ in close agreement with the expected one $S_t = 0.22$.

7.2.2 Meanflow computation

The meanflow $\mathbf{w_m}$ is then computed by averaging both in time and in the z direction in space $\mathbf{w_m} = \overline{\mathbf{w}}$. Note that the computed meanflow was found to be slightly dissymmetric, which probably comes from the fact that the average has been achieved on a small number of periods. We thus enforced the symmetry by keeping only the symmetric part of the meanflow.

In a first approximation, the mean eddy viscosity $\overline{\mu_t}$ is defined from the mean turbulent variables with:

$$\overline{\mu_t} = \frac{\overline{\rho}\overline{\rho k}}{\overline{\rho\omega}}. \tag{7.1}$$

Contours of the obtained eddy viscosity field μ_t are plotted in Fig.7.3(b) together with the velocity streamlines of the meanflow. We observe a recirculation bubble at the rear of the cylinder of length $\bar{l_r} = 0.89$ in relative agreement with the experimental result $\bar{l_r} = 0.82$ of Parezanović and Cadot [67] (note that due to the two dimensional nature

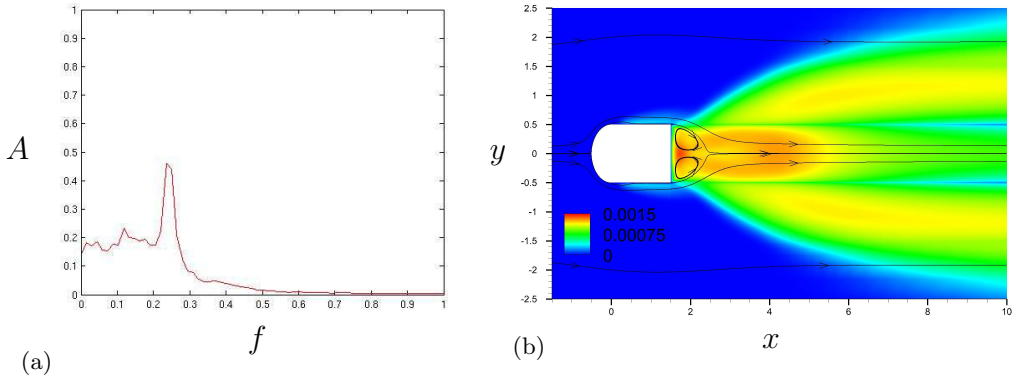

FIGURE 7.3: (a): Flow spectrum obtained with the signal extracted at the sensor S. (b): ρk contours and streamlines of the two dimensional meanflow $\mathbf{w_m}$.

of their configuration, the recirculation length computed in Meliga et al. [66] was 30% lower than the experimental value).

7.2.3 Discussion on the choice of a relevant eddy viscosity

Reynolds and Hussain [48] have shown that the linear stability analysis of a mean turbulent profile in a channel flow is generally improved when using an eddy viscosity. They justified the use of a frozen eddy viscosity as a fixed spatial field, for flows in which the perturbation waves do not impact the characteristic time of turbulent fluctuations. Analysing the dynamics of a turbulent flow around a NACA0012 profile, Crouch et al. [63] found that the eddy viscosity should be allowed to fluctuate when linearizing the RANS equations in order to observe the existence of a globally unstable. Oppositely, Barkley [138] observed that in the Reynolds number range $R_e = 46 - 180$, the flow dynamics of the wake behind a two dimensional cylinder could be described using laminar perturbations around the meanflow. These studies suggest that the impact of the viscosity field for flow modeled through the Boussinesq assumption may have a great impact onto the linear evolution of perturbations.

In a first approximation, we proposed to use the value given by our averaged turbulent variable to define this eddy viscosity ν_t. Note that this definition is not necessarily relevant, since the impact of the large scale coherent structures of the turbulence, available from our unsteady simulations, are not included in this definition. Furthermore, in DNS or experiments, one does not have direct access to this eddy viscosity field ν_t. The question of an intrinsic definition solely based on the computed or measured datas thus naturally arises.

Numerous models can be used with different levels of complexity. As an example, we can mention the $K - \epsilon$ model which relates the eddy viscosity to the turbulent kinetic

energy K and to the dissipation rate of turbulence ϵ with:

$$\nu_t = C_\mu \frac{K^2}{\epsilon}. \tag{7.2}$$

Note that here, as we integrated in time the RANS equations, we have access to the fluctuations of the large scale coherent structures of turbulence. These terms are not included in the turbulence model which was used, as it only models the small scales of turbulence. These fluctuations may thus be used to complement the definition of the turbulent energy K as well as the dissipation rate ϵ associated with the RANS model.

The point of this short study was to investigate the impact of this eddy viscosity modeling and show that its definition remains a difficult problem. We will thus perform in the following laminar ($\nu_t = 0$) and frozen eddy viscosity perturbations of the turbulent meanflow, and compare the results obtained with both approaches.

7.3 Direct and adjoint unstable modes

Viscosity model	σ	$f = \omega/2\pi$
μ	0.28	0.259
$\mu + \mu_t$	0.23	0.256

TABLE 7.2: Unstable eigenvalues obtained with a laminar and a frozen eddy viscosity model.

The linear stability analysis is performed similarly to the previous Chapters using in our formalism $\mathbf{w_b} = \mathbf{w_m}$. The Jacobian matrix $\mathbf{J}$ is first extracted and its spectrum is analysed. We observed the existence of an unstable mode for both laminar and frozen viscosity linearization, the corresponding eigenvalues are summarized in Table 7.2. Similarly to Meliga et al. [66], the unstable mode is slightly unstable with a frequency relatively close to the frequency computed from unsteady simulations (0.23). The spatial structure of the direct mode $\hat{\mathbf{w}}$ computed using the frozen eddy viscosity is depicted in Fig.7.4, while the corresponding adjoint mode structure $\tilde{\mathbf{w}}|_{\mathbf{Q}}$ is shown Fig.7.5.

We recover typical structures of Kelvin-Helmholtz instabilities with an opposite traveling direction between the direct and adjoint modes. Both direct and adjoint mode structures are similar to those computed by Meliga et al. [66]. The modes computed using a laminar model have similar structures.

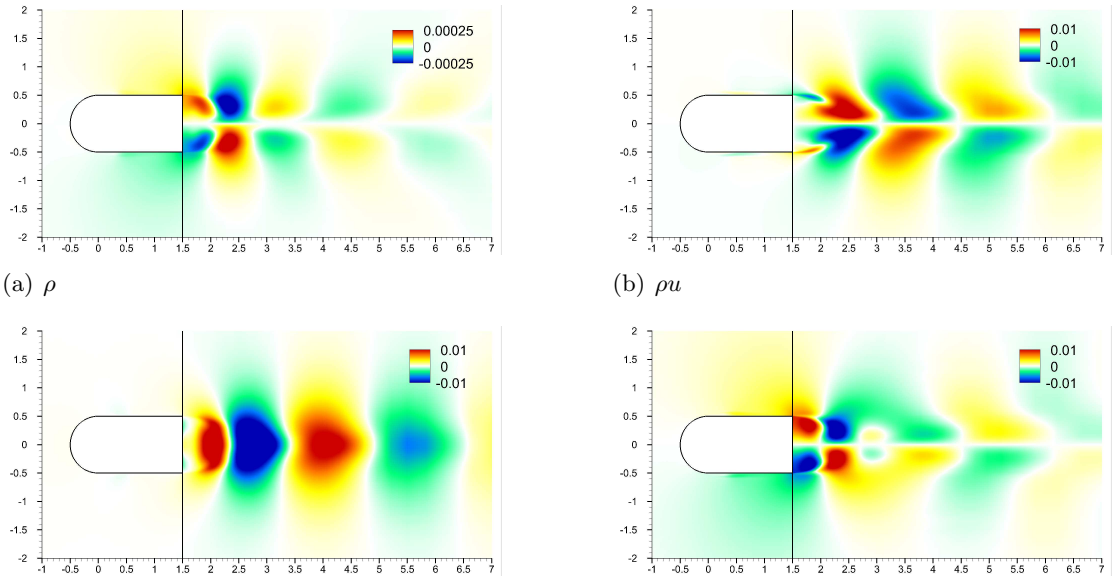

(a) ρ (b) ρu

(c) ρv (d) ρE

FIGURE 7.4: Spatial structure of the unstable mode $\hat{\mathbf{w}}$ computed using a frozen eddy viscosity. The real part is plotted.

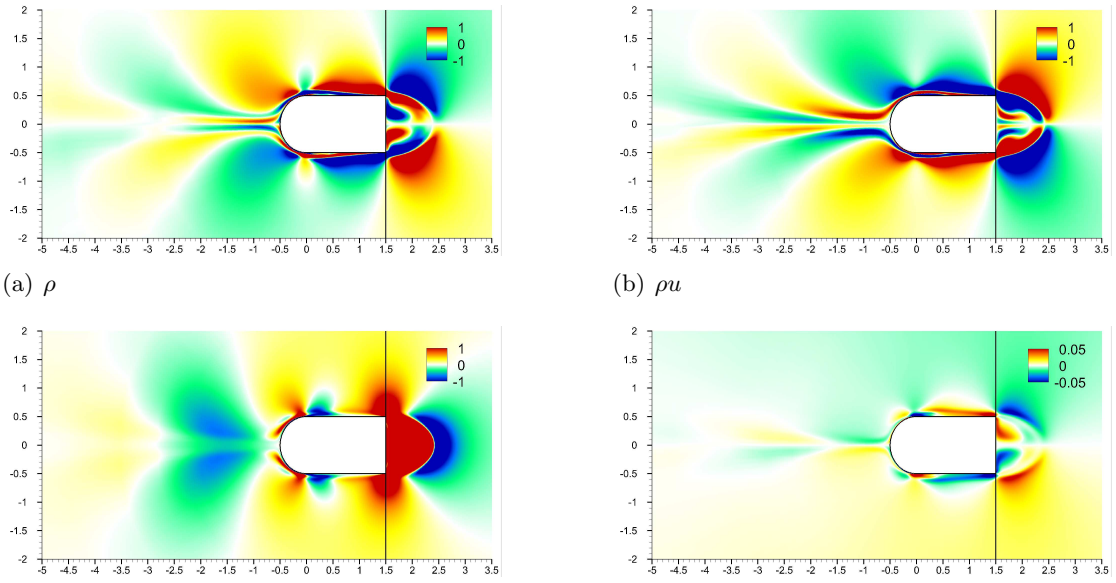

(a) ρ (b) ρu

(c) ρv (d) ρE

FIGURE 7.5: Spatial structure of the unstable adjoint mode $\tilde{\mathbf{w}}|_{\mathbf{Q}}$ computed using a frozen eddy viscosity. The real part is plotted.

7.4 Sensitivity gradients

The matrix $\mathbf{H}'$ is then extracted and the sensitivity gradient to meanflow perturbations $\boldsymbol{\nabla}_{\mathbf{w_m}}\lambda|_{\mathbf{Q}}$ is computed. Note that as stated by Sipp and Lebedev [68], for flows close to bifurcation, the linear analysis of the meanflow gives relevant information regarding the natural flow frequency selection, but lead to marginally stable modes with amplification

rates which are not physically relevant. We will thus focus in the following in the sensitivity analysis of the eigenvalue frequency ω.

We plotted in Fig.7.6 the spatial structure of the frequency sensitivity $\boldsymbol{\nabla}_{\mathbf{w_m}}\omega|_{\mathbf{Q}}$. The flow is mostly sensitive near the cylinder surface and inside the recirculation bubble.

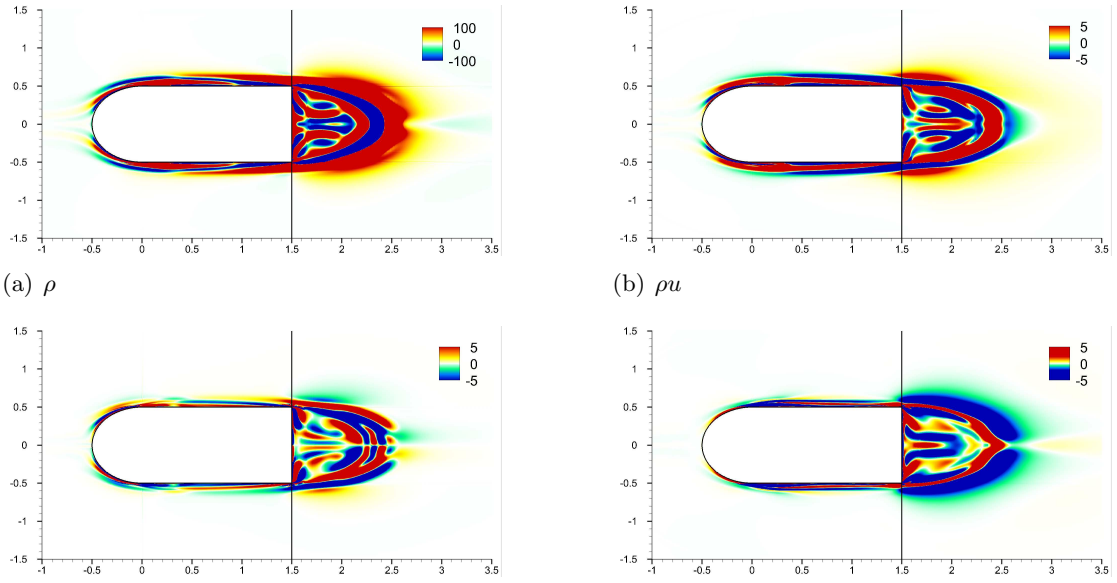

(a) ρ (b) ρu

(c) ρv (d) ρE

FIGURE 7.6: Spatial structure of the frequency sensitivity to meanflow perturbations $\boldsymbol{\nabla}_{\mathbf{w_m}}\omega|_{\mathbf{Q}}$ using a frozen eddy viscosity model.

As the meanflow $\mathbf{w_m}$ is a solution of the steady RANS equations $\mathcal{R}(\mathbf{w_m}) = 0$, the impact of a small amplitude steady force $\boldsymbol{\delta f}$ can be linked to a small meanflow variation $\boldsymbol{\delta w_m}$ through $\boldsymbol{\delta f} = -\mathbf{J}^{-1}\boldsymbol{\delta w_m}$ similarly to Section 2.2.2. Hence, we can still define the sensitivity gradient of the unstable eigenvalue to a steady force using $\boldsymbol{\nabla}_{\mathbf{f}}\lambda = -\mathbf{J}^{-1*}\boldsymbol{\nabla}_{\mathbf{w_m}}\lambda$.

The frequency sensitivity to a steady force $\boldsymbol{\nabla}_{\mathbf{f}}\omega|_{\mathbf{Q}}$ is then derived and depicted in Fig.7.7. We observe that a streamwise steady force has a destabilizing effect near the cylinder surface ($x < 1.5$ in the Figure), while a similar tendency can be observed in most part of the recirculating area.

Note that so far, the sensitivity gradients to meanflow perturbations $\boldsymbol{\nabla}_{\mathbf{w_m}}\lambda$ are correctly defined using both laminar and frozen eddy viscosity models. However, when linking a steady force perturbation to a meanflow variation through the relation $\boldsymbol{\delta f} = -\mathbf{J}^{-1}\boldsymbol{\delta w_m}$, we may expect that some turbulence effects may be involved in the induced meanflow variation as the meanflow is turbulent. As a consequence, as a more realistic approximation than the "full laminar method", we can define a mixed sensitivity gradient to a

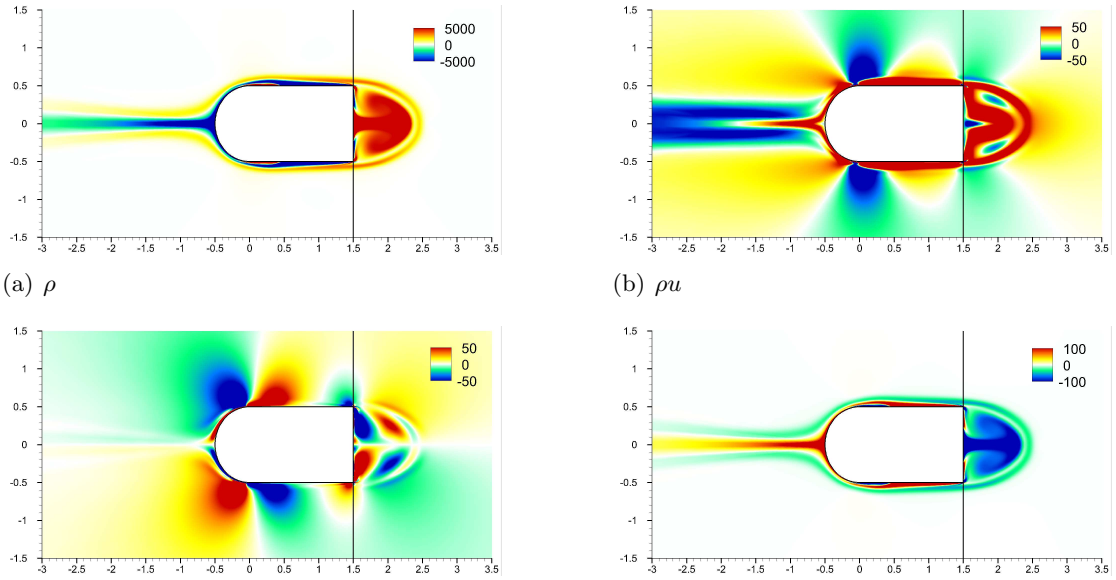

(a) ρ (b) ρu

(c) ρv (d) ρE

FIGURE 7.7: Spatial structure of the frequency sensitivity to a steady force $\boldsymbol{\nabla}_{\mathbf{f}}\omega|_{\mathbf{Q}}$ using a frozen eddy viscosity model.

steady force $\boldsymbol{\nabla}_{\mathbf{f}}\lambda^{\text{mixed}} = -\mathbf{J}^{-1*}_{\text{frozen}}\boldsymbol{\nabla}_{\mathbf{w_m}}\lambda^{\text{laminar}}$, where the gradient $\boldsymbol{\nabla}_{\mathbf{w_m}}\lambda^{\text{laminar}}$ is computed using laminar perturbations while the Jacobian $\mathbf{J}^{-1*}_{\text{frozen}}$ is obtained with our frozen eddy viscosity method. This mixed analysis allows us to forsee the impact of a steady force which incorporates turbulence effect onto the evolution of laminar perturbations.

7.5 Steady control of the flow frequency

Finally, similarly to Meliga et al. [66], we consider the impact of a control cylinder of diameter $d = 0.04$m onto the flow frequency. The local force $\mathbf{f_{xy}}$ exerted by the cylinder is modeled to the first order with:

$$\mathbf{f_{xy}} = -\frac{1}{2}dC_d\mathbf{U_{xy}}\left\|\mathbf{U_{xy}}\right\|/\Omega_{xy}, \tag{7.3}$$

where the drag coefficient was set to $C_d = 1$ and Ω_{xy} corresponds to the surface of the considered cell. The control map $\delta\omega_{xy} = \langle\boldsymbol{\nabla}_{\mathbf{f}}\omega,\mathbf{f_{xy}}\rangle$ which indicates the variation of the unstable frequency due to the presence of the control cylinder is depicted in Fig.7.8 for both laminar and frozen eddy viscosity model together with the results computed by Meliga et al. [66] and the results obtained using the aforementioned mixed model.

Several remarks can be made. First, we recover similar features between both analysis and the control map derived in [66]. Note that as both our computational procedure and our eddy viscosity model are different than those used in [66], we did not expect to

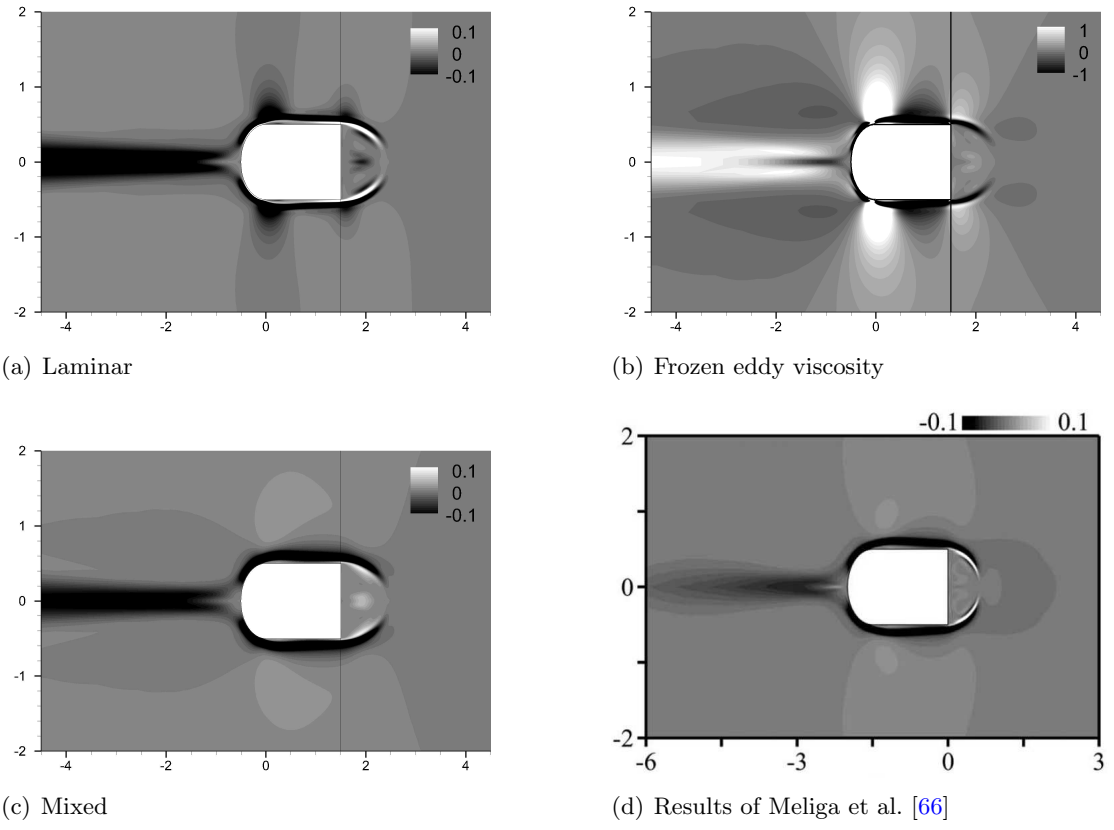

(a) Laminar

(b) Frozen eddy viscosity

(c) Mixed

(d) Results of Meliga et al. [66]

FIGURE 7.8: Frequency variation $\delta\omega_{xy}$ of the unstable mode due to the presence of a small control cylinder located at (x, y).

fully recover these previous results. The cylinder seems to lower the frequency of the mode when located near the surface of the D-shaped cylinder, while it does not impact it when located within the recirculation bubble. A striking result is that to the first order, the effect of the control cylinder can be approximated using laminar perturbations. The mixed model, which includes turbulence effects in the steady force, seems to lead to slightly improved results compared to the simple laminar approximation. This is a very interesting result as for an industrial application, the impact of a steady device can be approximated beforehand using laminar linear perturbations, without the inherent complexity of the definition of a turbulent eddy viscosity.

7.6 Concluding remarks

We revisited in this Chapter the dynamics of the turbulent wake behind a two dimensional cylinder. The linear stability analysis was performed onto a two dimensional meanflow computed from three dimensional unsteady simulations. The difficulty of the definition of a relevant eddy viscosity from available unsteady datas, in order to perform a linear stability analysis was emphasized. Using time and spatially averaged quantities,

the dynamics of the flow was analysed. The flow frequency selection seems to be link to the existence of an unstable mode. A sensitivity analysis was performed and the impact of a steady control device onto the unstable mode frequency was derived. Our results are in relative agreement with previous studies and suggest the validity of this study. The control effect of the cylinder was found to be well reproduced using laminar perturbations superimposed onto the turbulent meanflow, enhancing strong potential for industrial applications.

Chapter 8

Conclusion and perspectives

8.1 Conclusion

This theoretical and numerical study aimed at developing a new tool to perform linear stability analysis of a turbulent compressible flow modeled using RANS equations. To this end, a fully discrete formalism was developed in Chapter 2. The linear stability problem was derived by linearizing the discretized equations and the Jacobian matrix **J** was defined within this framework. The baseflow stability is then assessed with the resolution of an eigenvalue problem. Two types of dynamics can be observed: oscillators correspond to unstable flows for which one or several unstable modes will naturally develop and contaminate the whole flow field; noise amplifiers correspond to stable flows which may strongly amplify external perturbations. Both flows dynamics analyses were extended to the discrete framework. The sensitivity gradient to baseflow perturbations, which links modifications of the baseflow to eigenvalue variations for oscillators and to gain modifications for noise amplifiers was defined. In particular, the sensitivity gradient was shown to be linked to the Hessian of the RANS equations. Finally, the sensitivity gradient to a steady force was introduced for both oscillators and noise amplifiers, which gives access to interesting zones of the flow where a steady control device may lead to a stabilization of the flow.

Numerical aspects of the proposed formalism were detailed and analysed in Chapter 3. One of the critical steps of the method consists in the resolution of an eigenvalue problem which requires a matrix inversion algorithm. An explicit storage of matrices strategy was adopted, which allows fast and accurate computation of the matrices eigenvalues. Furthermore, the combination of discrete framework and explicit matrix storage allows immediate access to adjoint matrices required for the computation of the sensitivity gradients. The method remains however costly in terms of computational memory. Several

other strategies with iterative algorithm, and on-the-fly strategy were hence described to tackle three dimensional configurations. An efficient procedure was proposed to compute the Jacobian and the Hessian of the RANS equations using repeated evaluations of the residual operator. More specifically, the discrete equations are linearized using finite differences. The procedure exploits the sparsity of the considered matrices and allows the computation of all their coefficients in a few residual evaluations. The method efficiency relies on the definition of a particular set of perturbation vectors linked to the stencil discretization. The linearization parameters choice was also analysed, and a possible adaptation of shape optimization codes to perform linear stability analysis and compute the sensitivity gradients was proposed. We applied our fully discrete formalism to a finite volume code, and chose two widely used turbulence models to close the RANS equations: the $k-\omega$ model of Wilcox and the Spalart-Allmaras model.

A first validation step was carried out in Chapter 4 where we reproduced former results obtained on laminar flows in a continuous framework. The dynamics of the wake behind a two dimensional cylinder was first investigated similarly to Marquet et al. [32]. The critical Reynolds number was recovered, and the unstable mode and its adjoint were found to have similar features to those previously computed. The sensitivity gradient to a steady force was then computed and found identical to the one presented in [32]. As a second test case, the noise amplifier dynamics of an evolving boundary layer was analysed. Similarly to Brandt et al. [38], the amplifier properties of the flow were characterized through the gain function, and the sensitivity gradients to baseflow perturbations were computed. Our results are in excellent agreement with [38], suggesting that our fully discrete method is a valuable tool to perform such analysis.

The method was then tested on a turbulent compressible flow over a deep cavity in Chapter 5. This case enabled us to demonstrate the valuable information that both stability and sensitivity analysis of turbulent flows provide. Furthermore, it also allowed us to extensively analyse the validity and numerical properties of our fully discrete approach. The flow dynamics was modeled using the RANS equations closed with a turbulence model. The natural flow unsteadiness is recovered when integrating in time the unsteady RANS equations in agreement with experimental results. The baseflow was then computed and found to be unstable with the existence of several unstable modes. The fundamental frequency of the flow as well as several harmonics were shown to be linked to aero-acoustic modes associated with a feedback mechanism. The agreement between the linear stability analysis and the unsteady simulations suggest that the flow unsteadiness is linked to the existence of these unstable modes. Typical structures of Kelvin-Helmholtz instabilities are recovered when considering the spatial structure of the modes. The acoustic features of the flow were also captured as we observed acoustic resonance modes excited by Kelvin-Helmholtz instabilities. In the view of open loop

control, the sensitivity gradient of the unstable eigenvalue to baseflow perturbations $\boldsymbol{\nabla}_{\mathbf{w_b}}\lambda$ was computed. The flow is found to be mostly sensitive near the mixing layer and upstream of the cavity. Finally, the sensitivity gradient to a steady force $\boldsymbol{\nabla}_{\mathbf{f}}\lambda$ was determined. It indicates interesting areas of the flow where a steady force could lead to the stabilization of the unstable eigenvalue. A previsional control map using a steady cylinder as a mean to control the flow was derived for the fundamental mode. The cylinder was found to have a stabilizing effect on the mode near and upstream of the leading edge of the cavity, in agreement with experimental results. Numerous numerical tests were performed to analyse the robustness and validity of our fully discrete method. Mesh discretization was found to poorly affect the unstable modes frequency but did influence their growth rate. The impact of the linearization parameter onto the Jacobian computation was tested. The spectrum was observed to converge to the second order with the linearization parameters proving accuracy of the Jacobian computation. The genericity of the method with the system of equations was also investigated. As expected, the numerical scheme poorly affect the results. On the contrary, the choice of turbulence model had a slight impact on the growth rates of the unstable eigenvalues but not on their frequency. Still, similar features were obtained using both $k-\omega$ of Wilcox and Spalart-Allmaras turbulence model. The sensitivity gradients were validated using a discrete evaluation of the eigenvalue. The gradient were found to correctly predict the eigenvalue variation with an error lower then 3%. Finally, a particular analysis of the Spalart-Allmaras model was performed and a modification was proposed to improve the linearization of the model. The modifications were shown to poorly modify our results.

We presented in Chapter 6 results of parallel studies that were conducted using the formalism and tools that we developed. The dynamics of shock-wave/boundary layer interactions was first investigated in the case of the transonic buffet over a wing profile. The flow unsteadiness was found to be reproduced by unsteady simulations and was linked to the existence of an unstable mode of the RANS equations. The sensitivity gradients were then computed and the impact of a baseflow variations and a steady force were briefly discussed. Two other studies that were performed independently from this Ph.D were then presented. Results obtained on the dynamics of a strong shock impinging of a curved profile were first detailed. The noise amplifier dynamics of the flow was characterized and the low pass filter behavior of the shock was recovered. Properties of optimal forcing at high and low frequency were presented which reproduce the natural flow features. Finally, preliminary results obtained on sound generation in under-expanded jets were summarized. The screech phenomenon seems to be linked to the existence of unstable modes of the RANS equations.

Finally, we revisited in Chapter 7 the dynamics of the turbulent wake behind a two dimensional D-shaped cylinder. The linear stability analysis was performed onto a two

dimensional meanflow computed from three dimensional unsteady simulations. The difficulty of the definition of a relevant eddy viscosity from available unsteady datas was discussed. The flow frequency selection seems to be link to the existence of an unstable mode. A sensitivity analysis was performed and the impact of a steady control device onto the unstable mode frequency was derived. Our results are in relative agreement with previous studies. The control effect of the cylinder was found to be well reproduced using laminar perturbations superimposed onto the turbulent meanflow, enhancing strong potential for industrial applications.

The coherence of the numerical tests, as well as the physical information obtained on the several cases presented suggest the relevancy and the correctness of the proposed method. Linear stability and sensitivity analysis performed on RANS equations thus appear as a robust tool to analyse turbulent flows dynamics.

8.2 Perspectives

The proposed formalism and tools appeared to be adequate to characterize compressible turbulent flow dynamics. In a first time, the natural evolution of this work would consist in analysing new configurations and identify Hopf bifurcations or transient growth properties for flows at very high Reynolds number. Furthermore, the information carried out by sensitivity analysis could be also further compared to experimental studies. In a recent study, Grandemange et al. [139] considered the wake behind a three dimensional axisymetric body. They explored the control impact of steady devices onto the unsteadiness of the wake and showed that three dimensional steady control means could significantly alter the natural flow frequency. A complete linear stability analysis of this case with the computation of the sensitivity gradients may lead to interesting information regarding the mechanism responsible for frequency change of the flow.

Further developments can also be performed in terms of formalism and methods, based on the knowledge of the Hessian $\mathbf{H}$. The computational method used to compute the Hessian may be used to perform a weakly non linear stability analysis of a turbulent flow. Indeed, turbulent flows occur at high Reynolds number thus generally far from the critical Reynolds number. In such conditions, secondary instabilities may occur which are not predicted by linear stability analysis. A weakly non-linear analysis may thus be required to better understand turbulent flows unsteadiness for such cases. As detailed in Sipp and Lebedev [68], three steps are required to perform a weakly non-linear analysis. The first two step respectively consist in the computation of a baseflow and the resolution of an eigenvalue problem, similarly to a classical linear stability analysis. The third step corresponds to the resolution of a linear inhomogeneous equation where the forcing term

is given by the average of the Hessian applied to the unstable mode. As our formalism gives access to the Hessian, such an extension of the current method to perform weakly non linear analysis would thus be an other natural evolution of the current work.

An other natural next step would consist in the computation of three dimensional turbulent unstable modes. A full TriGlobal stability analysis is theoretically possible (three inhomogeneous spatial directions) with our method, although the necessary mesh dimensions for relevant analysis will require very high computational capabilities. A less intense approach would be to perform a pseudo BiGlobal stability analysis of a two dimensional baseflow, where the baseflow fluctuations in the linearization process are assumed periodic with a wavenumber β in the third direction. Such an analysis is possible here by extending our 2D baseflow in a 3D domain and imposing a periodical condition on the borders of our domain. The fluctuation wave number β would be imposed by the extension in the third direction of the computational frontiers. The residual evaluation can then be carried out and the Jacobian and unstable modes computed for this wave number. Of course, this procedure would require one jacobian computation and one eigenvalue resolution per wavelength β thus inducing important computational costs in terms of memory and time. However, such a procedure remains the fastest track to compute three dimensional turbulent unstable modes with our formalism.

However, such an analysis will lead to important matrices sizes requiring too large amount of memory for direct inversion methods. A first step to lower such a memory cost would be to use iterative algorithms for matrices inversions. Still, the matrices size may become problematic and the explicit storage strategy may become irrelevant. The implementation of an on the fly strategy as proposed by De Pando et al. [69] thus appear as a critical step with our fully discrete method to perform three dimensional stability analysis. The optimal set of vectors that we introduced may be used to optimize such a procedure.

Finally, in the view of industrial applications, the extension of linear stability analysis to turbulent flows obtained from Direct Numerical Simulations or experimental datas could be further analysed. The impact of the closure model, as well as the question of the relevant quantities of the flow to define the eddy viscosity remain interesting points to investigate. In this spirirt, the analysis we performed on the D-shaped cylinder suggests that for some flow configurations, a simple laminar sensitivity analysis may yield in a first approximation significant results regarding frequency control of unsteady flows. Such features may be exploited to design generic methods for industrial applications where experimental turbulent meanflow are available.

Appendix A

Appendix A

A.1 Scalar products definitions

A.1.1 Matrix Q

Let us consider two continuous complex functions $\mathbf{f}$,$\mathbf{g}$: $\Omega \in \mathbb{R}^{\mathrm{N}} \rightarrow \mathbb{C}^{\mathrm{N}}$. The domain Ω which corresponds to our mesh is discretized such that $\Omega = \bigcup_{i=1,N} \Omega_i$, and we designate by $\mathbf{F} \in \mathbb{C}^{\mathrm{N}}$ and $\mathbf{G} \in \mathbb{C}^{\mathrm{N}}$ the complex vectors corresponding to the discrete form of the functions $\mathbf{f}$ and $\mathbf{g}$ on $\bigcup_{i=1,N} \Omega_i$.

The discrete inner product $\langle , \rangle |_Q$ in Eq. (2.22) is defined as the discretization of the continuous inner product inducing the $\mathcal{L}^2$ norm. That is:

$$\int_{\Omega} \mathbf{f}^* \mathbf{g} d\Omega = \sum_{i=1,N} F_i^* G_i \Omega_i = \mathbf{F}^* \mathbf{Q} \mathbf{G} = \langle \mathbf{F}, \mathbf{G} \rangle |_Q. \tag{A.1}$$

As a consequence, $\mathbf{Q}$ is a real diagonal matrix whose terms Q_i correspond to the volume Ω_i of the discretized cell i.

A.1.2 Matrix $\mathbf{Q_e}$

We use in Chapter 2 the pseudo inner-product based on the energy matrix $\mathbf{Q_e}$ and defined such that for any response field $\hat{\mathbf{x}}$:

$$\langle \hat{\mathbf{x}}, \hat{\mathbf{x}} \rangle |_{Q_e} = \hat{\mathbf{x}}^* \mathbf{Q_e} \hat{\mathbf{x}} = E, \tag{A.2}$$

where E is the kinetic energy of the response $\hat{\mathbf{x}}$. Let us consider the two dimensional laminar response at a given cell location of our mesh $\hat{\mathbf{x}} = \left(\rho', (\rho u)', (\rho u)', (\rho E)'\right)^T$. As

the response corresponds to small perturbations of the baseflow conservative variables, we will denote its variable with $'$ to differentiate them from the baseflow values. We aim at computing the kinetic energy $E = \left(u'^2 + u'^2\right)\Omega$ of the response at the considered cell of volume Ω. We have at the first order:

$$(\rho\mathbf{u})' = \rho'\mathbf{u} + \rho\mathbf{u}', \tag{A.3}$$

$$(\rho\mathbf{v})' = \rho'\mathbf{v} + \rho\mathbf{v}'. \tag{A.4}$$

In particular, we are looking for for the coefficients a, b, c, d such that:

$$\begin{aligned} u'^2 &= \left(\rho', \rho'u + \rho u'\right) \begin{pmatrix} a, b \\ c, d \end{pmatrix} \begin{pmatrix} \rho' \\ \rho'u + \rho u' \end{pmatrix}, && \text{(A.5)} \\ &= a\rho'^2 + b\rho'^2 u + b\rho\rho' u' && \text{(A.6)} \\ &+ c\rho'^2 u + d\rho'^2 u^2 + d\rho\rho' uu' && \text{(A.7)} \\ &+ c\rho\rho' u' + d\rho\rho' uu' + d\rho^2 u'^2, && \text{(A.8)} \end{aligned}$$

which by identification leads to:

$$a = \tfrac{u^2}{\rho^2}, \quad b = -\tfrac{u}{\rho^2}, \quad c = -\tfrac{u}{\rho^2}, \quad d = \tfrac{1}{\rho^2}. \tag{A.9}$$

Therefore the energy matrix Q_e is given by:

$$u'^2 + v'^2 = \hat{\mathbf{x}}^* \begin{pmatrix} \frac{(u^2+v^2)\Omega}{\rho^2} & , & -\frac{u\Omega}{\rho^2} & , & -\frac{v\Omega}{\rho^2} & , & 0 \\ -\frac{u\Omega}{\rho^2} & , & \frac{\Omega}{\rho^2} & , & 0 & , & 0 \\ -\frac{v\Omega}{\rho^2} & , & 0 & , & \frac{\Omega}{\rho^2} & , & 0 \\ 0 & , & 0 & , & 0 & , & 0 \\ 0 & , & 0 & , & 0 & , & 0 \end{pmatrix} \hat{\mathbf{x}}. \tag{A.10}$$

The matrix Q_e is real, symmetric,and by definition semidefinite positive (enabling Cholesky decomposition). The extension of Q_e to turbulent response $\hat{\mathbf{x}}$ is straitforwardly obtained by adding 0 to the matrix.

Bibliography

[1] L Jacquin, P Molton, S Deck, B Maury, and D Soulevant. Experimental study of shock oscillation over a transonic supercritical profile. *AIAA journal*, 47(9): 1985–1994, 2009.

[2] E Electric. Pressure plotting of bulkheads fore and aft of bomb bay with bomb doors open. *Technical Report WT Rep. AX9, English Electric*, 1946.

[3] Mehdi R Khorrami, Mert E Berkman, and Meelan Choudhari. Unsteady flow computations of a slat with a blunt trailing edge. *AIAA journal*, 38(11):2050–2058, 2000.

[4] G Raman. Supersonic jet screech: Half-century from powell to the present. *Journal of Sound and Vibration*, 225(3):543–571, 1999.

[5] Carlo Cossu, Luca Brandt, Shervin Bagheri, and Dan S Henningson. Secondary threshold amplitudes for sinuous streak breakdown. *Physics of fluids*, 23:074103, 2011.

[6] P. Huerre and P. A. Monkewitz. Local and global instabilities in spatially developing flows. *Annual Review of Fluid Mechanics*, 22:473–537, 1990.

[7] P Huerre and M Rossi. Hydrodynamic instabilities in open flows. *Collection Alea Saclay, Monographs and texts i Statistical Physics*, pages 81–294, 1998.

[8] Benoît Pier. On the frequency selection of finite-amplitude vortex shedding in the cylinder wake. *Journal of Fluid Mechanics*, 458(1):407–417, 2002.

[9] S.J. Lawson and G.N Barakos. Review of numerical simulations for high-speed, turbulent cavity flows. *Progress in Aerospace Sciences*, 47:186–216, 2011.

[10] P Huerre and P Monkewitz. Absolute and convective instabilities in free shear layers. *Journal of Fluid Mechanics*, 159:151–68, 1985.

[11] Frédéric Alizard and Jean-Christophe Robinet. Spatially convective global modes in a boundary layer. *Physics of fluids*, 19(11):114105, 2007.

[12] Xavier Garnaud, Lutz Lesshafft, PJ Schmid, and Patrick Huerre. The preferred mode of incompressible jets: linear frequency response analysis. *Journal of Fluid Mechanics*, 716:189–202, 2013.

[13] HM Blackburn, Dwight Barkley, and Spencer J Sherwin. Convective instability and transient growth in flow over a backward-facing step. *Journal of Fluid Mechanics*, 603:271–304, 2008.

[14] Dwight Barkley, M Gabriela M Gomes, and Ronald D Henderson. Three-dimensional instability in flow over a backward-facing step. *Journal of Fluid Mechanics*, 473:167–190, 2002.

[15] C. Godrèche and P. Manneville. *Hydrodynamics and nonlinear instabilities*, volume 3. Cambridge Univ Pr, 1998.

[16] Vassilios Theofilis. Global linear instability. *Annual Review of Fluid Mechanics*, 43:319–352, 2011.

[17] D. Sipp, O. Marquet, O. Meliga, and A. Barbagallo. Dynamics and control of global instabilities in open flows: a linearized approach. *Applied Mechanics Reviews*, 63: 030801, 2010.

[18] J.-M. Chomaz. Global instabilities in spatially developing flows: Non-normality and nonlinearity. *Annual Review of Fluid Mechanics*, 37:357, 2005.

[19] L. Trefethen, A. Trefethen, S. Reddy, and T. Driscoll. Hydrodynamic stability without eigenvalues. *Science*, 261(5121):578–584, 1993.

[20] Brian F Farrell and Petros J Ioannou. Optimal excitation of three-dimensional perturbations in viscous constant shear flow. *Physics of Fluids A: Fluid Dynamics*, 5:1390, 1993.

[21] P. J. Schmid and D. S Henningson. *Stability and transition in shear flows*, volume 142. Springer, 2001.

[22] Olivier Marquet, Denis Sipp, Jean-Marc Chomaz, and Laurent Jacquin. Amplifier and resonator dynamics of a low-reynolds-number recirculation bubble in a global framework. *Journal of Fluid Mechanics*, 605:429, 2008.

[23] Carlo Cossu, Gregory Pujals, and Sebastien Depardon. Optimal transient growth and very large-scale structures in turbulent boundary layers. *Journal of Fluid Mechanics*, 619:79, 2009.

[24] Uwe Ehrenstein and Francois Gallaire. On two-dimensional temporal modes in spatially evolving open flows: the flat-plate boundary layer. *Journal of Fluid Mechanics*, 536:209–218, 2005.

[25] M. Gad-el Hak, A. Pollard, and J.-P. Bonnet. *Flow Control: Fundamentals and Practices*. Berlin: Springer-Verlag, 1998.

[26] SS. Collis, RD. Joslin, A. Seifert, and V. Theofilis. Issues in active flow control: theory, control, simulation, and experiment. *Progress in Aerospace Sciences*, 40 (4-5):237–289, 2004.

[27] F. Giannetti and P. Luchini. Structural sensitivity of the first instability of the cylinder wake. *Journal of Fluid Mechanics*, 581:167–197, 2007.

[28] J. Kim and T. R. Bewley. A linear systems approach to flow control. *Annual Review of Fluid Mechanics*, 39:383–417, 2007.

[29] Denis Sipp. Open-loop control of cavity oscillations with harmonic forcings. *Journal of Fluid Mechanics*, 708:439, 2012.

[30] D. C. Hill. A theoretical approach for analyzing the restabilization of wakes. *AIAA 1992-0067*, 1992.

[31] F Giannetti and P Luchini. Receptivity of the circular cylinders first instability. In *Proc. 5th Eur. Fluid Mech. Conf., Toulouse*, 2003.

[32] O. Marquet, D. Sipp, and L. Jacquin. Sensitivity analysis and passive control of cylinder flow. *Journal of Fluid Mechanics*, 615:221–252, 2008.

[33] P. J. Strykowski and K. R. Sreenivasan. On the formation and suppression of vortex shedding at low Reynolds-numbers. *Journal of Fluid Mechanics*, 218:71–107, 1990.

[34] Jano Pralits, Luca Brandt, and Flavio Giannetti. Instability and sensitivity of the flow around a rotating circular cylinder. *Journal of Fluid Mechanics*, 650:513, 2010.

[35] Frédéric Alizard, Jean-Christophe Robinet, and Ulrich Rist. Sensitivity analysis of a streamwise corner flow. *Physics of Fluids*, 22:014103, 2010.

[36] Andrea Fani, Simone Camarri, and Maria Vittoria Salvetti. Stability analysis and control of the flow in a symmetric channel with a sudden expansion. *Physics of Fluids*, 24:084102, 2012.

[37] Outi Tammisola. Oscillatory sensitivity patterns for global modes in wakes. *Journal of Fluid Mechanics*, 701:251–277, 2012.

[38] Luca Brandt, Denis Sipp, Jan O Pralits, and Olivier Marquet. Effect of base-flow variation in noise amplifiers: the flat-plate boundary layer. *Journal of Fluid Mechanics*, 687:503, 2011.

[39] Brian F Farrell. Optimal excitation of perturbations in viscous shear flow. *Physics of Fluids*, 31:2093, 1988.

[40] MT Landahl. A note on an algebraic instability of inviscid parallel shear flows. *Journal of Fluid Mechanics*, 98(02):243–251, 1980.

[41] W. Rodi. Comparison of les and rans calculations of the flow around bluff bodies. *Journal of Wind Engineering and Industrial Aerodynamics*, 69:55–75, 1997.

[42] G. Iaccarino, A. Ooi, PA Durbin, and M. Behnia. Reynolds averaged simulation of unsteady separated flow. *International Journal Heat Fluid Flow*, 24(2):147–156, 2003.

[43] S. Deck. Numerical simulation of transonic buffet over a supercritical airfoil. *AIAA Journal*, 43(7):1556–1566, 2005.

[44] Albert A Townsend. *The structure of turbulent shear flow*. Cambridge university press, 1956.

[45] MJ Lighthill. Dynamics of a dissociating gas. part i. equilibrium flow. *Journal of Fluid Mechanics*, 2(1):1–32, 1957.

[46] J. Lumley. The applicability of turbulence research to the solution of the internal flow problems. *Fluid Mechanics of Internal Flow*, page 152, 1967.

[47] RD Cess. A survey of the literature on heat transfer in turbulent tube flow. *Res. Rep*, pages 8–0529, 1958.

[48] WC Reynolds and AKMF Hussain. The mechanics of an organized wave in turbulent shear flow. part 3. theoretical models and comparisons with experiments. *Journal of Fluid Mechanics*, 54(02):263–288, 1972.

[49] WP Jones and BE Launder. The calculation of low-reynolds-number phenomena with a two-equation model of turbulence. *International Journal of Heat and Mass Transfer*, 16(6):1119–1130, 1973.

[50] Kuei-Yuan Chien. Predictions of channel and boundary-layer flows with a low-reynolds-number turbulence model. *AIAA journal*, 20(1):33–38, 1982.

[51] D. Wilcox. Reassessment of the Scale-Determining Equation for Advanced Turbulence Models. *AIAA 1988-1299*, 26(11):12991310, 1988.

[52] Brianr Smith. The k-kl turbulence model and wall layer model for compressible flows. In *AIAA, Fluid Dynamics, Plasma Dynamics and Lasers Conference, 21 st, Seattle, WA*, page 1990, 1990.

[53] P.R. Spalart and S.R. Allmaras. A One-Equation Turbulence Model for Aerodynamic Flows. *AIAA 92-439*, 1992.

[54] Viktor V Babenko, Ho-Hwan Chun, and Inwon Lee. *Boundary layer flow over elastic surfaces: compliant surfaces and combined methods for marine vessel drag reduction*. Butterworth-Heinemann, 2012.

[55] Marc Buffat, Lionel Le Penven, Anne Cadiou, and Julien Montagnier. Dns of bypass transition in entrance channel flow induced by boundary layer interaction. *European Journal of Mechanics-B/Fluids*, 2013.

[56] Kathryn M Butler and Brian F Farrell. Optimal perturbations and streak spacing in wall-bounded turbulent shear flow. *Physics of Fluids A: Fluid Dynamics*, 5:774, 1993.

[57] WC Reynolds and WG Tiederman. Stability of turbulent channel flow, with application to malkuss theory. *Journal of Fluid Mechanics*, 27(part 2):253–272, 1967.

[58] C. Juan and J. Jiménez. Linear energy amplification in turbulent channels. *Journal of Fluid Mechanics*, 559:205–213, 2006.

[59] Gregory Pujals, Manuel García-Villalba, Carlo Cossu, and Sebastien Depardon. A note on optimal transient growth in turbulent channel flows. *Physics of Fluids*, 21:015109, 2009.

[60] Y. Hwang and C. Cossu. Amplification of coherent streaks in the turbulent couette flow: an input–output analysis at low reynolds number. *Journal of Fluid Mechanics*, 643:333, 2010.

[61] Yongyun Hwang and Carlo Cossu. Linear non-normal energy amplification of harmonic and stochastic forcing in the turbulent channel flow. *Journal of Fluid Mechanics*, 664:51–73, 2010.

[62] Vassili Kitsios, Laurent Cordier, J-P Bonnet, Andrew Ooi, and Julio Soria. Development of a nonlinear eddy-viscosity closure for the triple-decomposition stability analysis of a turbulent channel. *Journal of Fluid Mechanics*, 664:74–107, 2010.

[63] J. D. Crouch, A. Garbaruk, and D. Magidov. Predicting the onset of flow unsteadiness based on global instability. *Journal of Computational Physics*, 224(2): 924–940, 2007.

[64] J. D. Crouch, A. Garbaruk, D. Magidov, and A. Travin. Origin of transonic buffet on aerofoils. *Journal of Fluid Mechanics*, 628:357369, 2009.

[65] P. R. Spalart and S. R. Allmaras. A One-Equation turbulence model for aerodynamic flows. *Recherche arospatiale*, 1:5–21, 1994.

[66] P. Meliga, G. Pujals, and E. Serre. Sensitivity of 2-d turbulent flow pas a d-shaped cylinder using global stability. *Physics of Fluids*, 24, 2012.

[67] V. Parezanović and O. Cadot. Experimental sensitivity analysis of the global properties of a two-dimensional turbulent wake. *Journal of Fluid Mechanics*, 1(1): 1–35, 2012.

[68] D. Sipp and A. Lebedev. Global stability of base and mean flows: a general approach and its applications to cylinder and open cavity flows. *Journal of Fluid Mechanics*, 593:333–358, 2007.

[69] M.F. De Pando, D. Sipp, and P.J. Schmid. Efficient evaluation of the direct and adjoint linearized dynamics from compressible flow solvers. *Journal of Computational Physics*, 2012.

[70] M. B. Giles and N. A. Pierce. Analytic adjoint solutions for the quasi-one-dimensional euler equations. *Journal of Fluid Mechanics*, 426(2001):327–345, 2001.

[71] J-Ch Robinet. Bifurcations in shock-wave/laminar-boundary-layer interaction: global instability approach. *Journal of Fluid Mechanics*, 579(1):85–112, 2007.

[72] J.E.V. Peter and R.P. Dwight. Numerical sensitivity analysis for aerodynamic optimization: A survey of approaches. *Computers and Fluids*, 39(3):373–391, 2010.

[73] M. B. Giles and N. A Pierce. An introduction to the adjoint approach to design. *Flow, turbulence and combustion*, 65(3-4):393–415, 2000.

[74] Siva Nadarajah and Antony Jameson. Studies of the continuous and discrete adjoint approaches to viscous automatic aerodynamic shape optimization. *AIAA paper*, 2530:2001, 2001.

[75] J. Peter and F. Drullion. Large stencil viscous flux linearization for the simulation of 3D compressible turbulent flows with backward-Euler schemes. *Computational Fluids*, 36:1005–1027, 2007.

[76] T.J. Poinsot and SK Lelef. Boundary conditions for direct simulations of compressible viscous flows. *Journal of Computational Physics*, 101(1):104–129, 1992.

[77] Antony Jameson, Wolfgang Schmidt, Eli Turkel, et al. Numerical solutions of the euler equations by finite volume methods using runge-kutta time-stepping schemes. *AIAA paper*, 1259:1981, 1981.

[78] Alain Lerat and Christophe Corre. A residual-based compact scheme for the compressible navier–stokes equations. *Journal of Computational Physics*, 170(2):642–675, 2001.

[79] P.L. Roe. Approximate riemann solvers, parameter vectors, and difference schemes. *Journal of Computational Physics*, 43(2):357–372, 1981.

[80] Bram Van Leer. *Flux-vector splitting for the Euler equation*. Springer, 1997.

[81] G.D. van Albada, B. van Leer, and Roberts W.W. A Comparative Study of Computational Methods in Cosmic Gas Dynamics. *Astron. Astrophys.*, 108:76–84, 1982.

[82] V Theofilis and T Colonius. Three-dimensional instabilities of compressible flow over open cavities: direct solution of the biglobal eigenvalue problem. *AIAA Paper*, 2544:2004, 2004.

[83] N. Forestier, L. Jacquin, and P. Geffroy. The mixing layer over a deep cavity at high-subsonic speed. *Journal of Fluid Mechanics*, 475:101–145, 2003.

[84] Lionel Larchevêque, Pierre Sagaut, and Odile Labbé. Large-eddy simulation of a subsonic cavity flow including asymmetric three-dimensional effects. *Journal of Fluid Mechanics*, 577(1):105–126, 2007.

[85] Vassilios Theofilis. Advances in global linear instability analysis of nonparallel and three-dimensional flows. *Progress in aerospace sciences*, 39(4):249–315, 2003.

[86] A. Bottaro, P. Corbett, and P. Luchini. The effect of base flow variation on flow stability. *Journal of Fluid Mechanics*, 476:293–302, 2003.

[87] G Dergham, D Sipp, and J-C Robinet. Accurate low dimensional models for deterministic fluid systems driven by uncertain forcing. *Physics of Fluids*, 23: 094101, 2011.

[88] G Dergham, D Sipp, and J-Ch Robinet. Stochastic dynamics and model reduction of amplifier flows: the backward facing step flow. *Journal of Fluid Mechanics*, 719: 406–430, 2013.

[89] C.J. Mack and P.J. Schmid. A preconditioned krylov technique for global hydrodynamic stability analysis of large-scale compressible flows. *Journal of Computational Physics*, 229(3):541–560, 2010.

[90] R.B. Lehoucq, D.C. Sorensen, and C. Yang. *ARPACK users' guide: solution of large-scale eigenvalue problems with implicitly restarted Arnoldi methods*, volume 6. Siam, 1998.

[91] C. K. Mamun and L. S. Tuckerman. Asymmetry and hopf bifurcation in spherical couette flow. *Physics of Fluids*, 7:80, 1995.

[92] Shervin Bagheri, Espen Åkervik, Luca Brandt, and Dan S Henningson. Matrix-free methods for the stability and control of boundary layers. *AIAA journal*, 47 (5):1057–1068, 2009.

[93] D.A. Knoll and D.E. Keyes. Jacobian-free newton–krylov methods: a survey of approaches and applications. *Journal of Computational Physics*, 193(2):357–397, 2004.

[94] Heng-Bin An, Ju Wen, and Tao Feng. On finite difference approximation of a matrix-vector product in the jacobian-free newton–krylov method. *Journal of Computational and Applied Mathematics*, 236(6):1399–1409, 2011.

[95] J. Sobieszczanski-Sobieski. The case for aerodynamic sensitivity analysis. *Technical Report CP 2457, NASA*, 1987.

[96] GV. Candler and RW. MacCormack. Hypersonic flow past 3-D configuration. *AIAA Paper 87-0480*, 1987.

[97] L Cambier, S Heib, and S Plot. The onera elsa cfd software: input from research and feedback from industry. In *28th International Congress of the Aeronautical Sciences, ICAS*, volume 2, 2012.

[98] Laurent Cambier, Sébastien Heib, and Sylvie Plot. The onera elsa cfd software: input from research and feedback from industry. *Mechanics and Industry*, 14: 159–174, 1 2013. ISSN 2257-7750. doi: 10.1051/meca/2013056. URL http://www.mechanics-industry.org/article_S2257777713000560.

[99] L. Martinelli. Calculations of viscous flows with a multigrid method. 1987.

[100] B. Van Leer. Towards the ultimate conservative difference scheme. v. a second-order sequel to godunov's method. *Journal of Computational Physics*, 32(1):101–136, 1979.

[101] Ivan Mary, Pierre Sagaut, and Michel Deville. An algorithm for unsteady viscous flows at all speeds. *International Journal of Numerical Methods for Fluids*, 34(5): 371–401, 2000.

[102] A. Harten and H. Hyman. Self adjusting grid methods for one-dimensional hyperbolic conservation laws. *J. Comp. Phys.*, 50:235–69, 1983.

[103] X. Zheng, C. Lia, CH. Sung, and TT. Huand. Multigrid computation of incompressible flows using two-equation tubulence models: PartI - Numerical method. *J. Fluids Eng.*, 119:839–9, 1997.

[104] J Peter. Discrete adjoint method in elsa (part i): method/theory. In *Proceedings of the ONERA-DLR Aerospace Symposium (ODAS), Toulouse*, 2006.

[105] I. S. El Din, G. Carrier, and S. Mouton. Discrete adjoint method in elsa (part 2): Application to aerodynamic design optimisation. In *Proceedings of the 7th ONERA-DLR Aerospace Symposium (ODAS), Toulouse*, 2006.

[106] Jacques Peter, Maxime Nguyen-Dinh, and Pierre Trontin. Goal oriented mesh adaptation using total derivative of aerodynamic functions with respect to mesh coordinates. with applications to euler flows. *Computational Fluids*, 2012.

[107] Florent Renac. Improvement of the recursive projection method for linear iterative scheme stabilization based on an approximate eigenvalue problem. *Journal of Computational Physics*, 230(14):5739–5752, 2011.

[108] Espen Åkervik, Uwe Ehrenstein, François Gallaire, and Dan S Henningson. Global two-dimensional stability measures of the flat plate boundary-layer flow. *European Journal of Mechanics-B/Fluids*, 27(5):501–513, 2008.

[109] H. Illy, P. Geffroy, and L. Jacquin. Observations on the passive control of flow oscillations over a cavity in a transonic regime by means of a spanwise cylinder. *AIAA 2008-3774*, 2008.

[110] S. Yamouni. Contrôle en boucle ouverte des instationnarités de cavité en régime transsonique. *Thse de l'Ecole Polytechnique*, 2013.

[111] J.E. Rossiter. Wind-Tunnel Experiments on the Flow over Rectangular Cavities at Subsonic and Transonic Speeds. *Royal Aircraft Establishment ARC R&M*, (3438), 1966.

[112] S. Deck, P.É. Weiss, M. Pamiès, and E. Garnier. Zonal detached eddy simulation of a spatially developing flat plate turbulent boundary layer. *Comp. Fluids*, 48(1): 1–15, 2011.

[113] Sami Yamouni, Denis Sipp, and Laurent Jacquin. Interaction between feedback aeroacoustic and acoustic resonance mechanisms in a cavity flow: a global stability analysis. *Journal of Fluid Mechanics*, 717:134–165, 2013.

[114] L.F. East. Aerodynamically induced resonnance in rectangular cavities. *J. Sound Vib.*, 3(3):277–287, 1966.

[115] David S Dolling. Fifty years of shock-wave/boundary-layer interaction research: what next? *AIAA journal*, 39(8):1517–1531, 2001.

[116] Emile Touber and Neil D Sandham. Large-eddy simulation of low-frequency unsteadiness in a turbulent shock-induced separation bubble. *Theoretical and Computational Fluid Dynamics*, 23(2):79–107, 2009.

[117] H Seegmiller, L Levy JR, and J Marvin. Steady and unsteady transonic flow. *AIAA Journal*, 16(12):1262–1270, 1978.

[118] D Caruana, A Mignosi, C Robitaillie, and M Correge. Separated flow and buffeting control. *Flow, turbulence and combustion*, 71(1-4):221–245, 2003.

[119] G Barakos and D Drikakis. Numerical simulation of transonic buffet flows using various turbulence closures. *International Journal of Heat and Fluid Flow*, 21(5): 620–626, 2000.

[120] Injae Chung, Duckjoo Lee, and Taekyu Reu. Prediction of transonic buffet onset for an airfoil with shock induced separation bubble using steady navier-stokes solver. *AIAA Journal*, 2934, 2002.

[121] Fulvio Sartor, Gilles Losfeld, and Reynald Bur. Piv study on a shock-induced separation in a transonic flow. *Experiments in fluids*, 53(3):815–827, 2012.

[122] F Sartor, C Mettot, D Sipp, and R Bur. Dynamics of a shock-induced separation in a transonic flow: a linearized approach. 43^{th} *Fluid dynamics conference, AIAA San Diego*, 2013.

[123] S Piponniau, JP Dussauge, JF Debiève, and P Dupont. A simple model for low-frequency unsteadiness in shock-induced separation. *Journal of Fluid Mechanics*, 629:87, 2009.

[124] Masaru Kiya and Kyuro Sasaki. Structure of a turbulent separation bubble. *Journal of Fluid Mechanics*, 137(83):113, 1983.

[125] Alan Powell. On the noise emanating from a two-dimensional jet above the critical pressure. *Aeronautical Quarterly*, 4(Part II), 1953.

[126] Alan Powell. The noise of choked jets. *The Journal of the Acoustical Society of America*, 25:385, 1953.

[127] Alan Powell. The reduction of choked jet noise. *Proceedings of the Physical Society. Section B*, 67(4):313, 1954.

[128] CKW Tam. The shock-cell structures and screech tone frequencies of rectangular and non-axisymmetric supersonic jets. *Journal of Sound and Vibration*, 121(1): 135–147, 1988.

[129] WD Bryce and RA Pinker. The noise from unheated supersonic jets in simulated flight. *AIAA Paper*, (77-1327), 1977.

[130] Shervin Bagheri, Philipp Schlatter, Peter J Schmid, and Dan S Henningson. Global stability of a jet in crossflow. *Journal of Fluid Mechanics*, 624(9):33–44, 2009.

[131] Philippe Meliga and Jean-Marc Chomaz. Global modes in a confined impinging jet: application to heat transfer and control. *Theoretical and Computational Fluid Dynamics*, 25(1-4):179–193, 2011.

[132] Joseph W Nichols and Sanjiva K Lele. Global modes and transient response of a cold supersonic jet. *Journal of Fluid Mechanics*, 669:225–241, 2011.

[133] Julien Berland, Christophe Bogey, and Christophe Bailly. Numerical study of screech generation in a planar supersonic jet. *Physics of fluids*, 19(7):075105–075105, 2007.

[134] FR Menter and Y Egorov. The scale-adaptive simulation method for unsteady turbulent flow predictions. part 1: theory and model description. *Flow, Turbulence and Combustion*, 85(1):113–138, 2010.

[135] Farid Benyoucef, Hervé Bézard, Bertrand Aupoix, and Bertrand Michel. Sas-sst model assessment and improvement. In *Conference on Modelling Fluid Flow (CMFF12)*, 2012.

[136] S Didorally, H Bezard, and E Laroche. Numerical simulation of the unsteady flow past a heated square cylinder. *ICHMT DIGITAL LIBRARY ONLINE*, 2012.

[137] F. Benyoucef. Amélioration de la prévision des écoulements turbulent par une approche urans avancée. *Thèse de l'Institut Supérieur de l'Aéronautique et de l'Espace*, 2012.

[138] D Barkley. Linear analysis of the cylinder wake mean flow. *EPL (Europhysics Letters)*, 75(5):750, 2006.

[139] M Grandemange, M Gohlke, V Parezanović, and O Cadot. On experimental sensitivity analysis of the turbulent wake from an axisymmetric blunt trailing edge. *Physics of Fluids*, 24:035106, 2012.